Analytical approach to crack tip plasticity of dental CoCrMo alloy

Lovrenić-Jugović, Martina; Slokar Benić, Ljerka; Jandrlić, Ivan

Source / Izvornik: **Machines. Technologies. Materials 2022. Proceedings, Volume III, Machines. Materials., 2022, 226 - 228**

Conference paper / Rad u zborniku

Publication status / Verzija rada: **Published version / Objavljena verzija rada (izdavačev PDF)**

Permanent link / Trajna poveznica: https://urn.nsk.hr/urn:nbn:hr:115:615272

XIX INTERNATIONAL SCIENTIFIC CONGRESS

SUMMER SESSION

07 - 10.09.2022, VARNA, BULGARIA

MACHINES TECHNOLOGIES MATERIALS 2022

PROCEEDINGS

VOLUME III
MACHINES
MATERIALS

ISSN 2535-0021 (Print)
ISSN 2535-003X (Online)

ORGANIZER
SCIENTIFIC-TECHNICAL UNION OF MECHANICAL ENGINEERING
BULGARIA

XIX INTERNATIONAL SCIENTIFIC CONGRESS

MACHINES. TECHNOLOGIES. MATERIALS

07-10.09.2022, VARNA, BULGARIA

PROCEEDINGS

YEAR V, ISSUE 3 (23), VARNA, BULGARIA 2022

VOLUME III

MACHINES. MATERIALS.

ISSN 2535-0021 (PRINT)
ISSN 2535-003X (ONLINE)

PUBLISHER:

SCIENTIFIC TECHNICAL UNION OF MECHANICAL ENGINEERING INDUSTRY-4.0

108, Rakovski Str., 1000 Sofia, Bulgaria
tel. (+359 2) 987 72 90,
tel./fax (+359 2) 986 22 40**,**
office@mtmcongress.com
www.mtmcongress.com

INTERNATIONAL EDITORIAL BOARD

C O N T E N T S

MACHINES.

MATERIALS.

Dependance on the required power of the electric motor on the CNC Spinner EL-510 lathe according to the depth of cut for turning and facing with CNMG 120408-PM 4325 tool insert

Violeta Krcheva[1], Marija Chekerovska[1]
[1]Faculty of Mechanical Engineering
'Goce Delcev' University - Stip, Republic of North Macedonia
violeta.krceva@ugd.edu.mk, marija.cekerovska@ugd.edu.mk

Abstract: *A lathe is a machine that removes metal from a workpiece to the required shape and size. A lathe operates on the principle of a rotating workpiece and a fixed cutting tool. The cutting tool is fed into the workpiece, which rotates about its own axis, causing the workpiece to be formed into the desired shape. The operation by which the excess material is removed from the workpiece to produce a cone or cylindrical shape is called turning, and the operation used to cut a flat surface perpendicular to the workpiece's rotational axis is called facing. Speed, feed, and depth of cut are important factors that have to be determined according to the power of the CNC Spinner EL-510 lathe using a PCLNR 2525M 12 shank tool and a CNMG 120408-PM 4325 tool insert.*
Keywords*: MACHINING, METAL CUTTING, CUTTING CONDITIONS, SPEED, FEED*

1. Introduction

The material removal processes are a family of shaping operations in which the removal of material from a starting workpiece results in a transformed product machined to the desired final geometry. The most important branch of that family is machining. Machining, as a manufacturing process, is most frequently applied to shape metals into convenient products, which consists of forcing a sharp cutting tool to cut away a layer of material on the workpiece blank to achieve the desired part shape and size. Actually, machining is a generic term, applied to all material removal, while metal cutting refers to processes in which the excess material is removed by a harder tool, through a process of extensive plastic deformation or controlled fracture [1].

The predominant cutting action in metal cutting involves separation of the work material to form a chip. When the cutting tool is fed along the finished contour, a new surface is generated. It is usually performed after other manufacturing processes that create the general shape of the starting workpiece, and metal cutting provides the final geometry of the resulting work surface. Metal cutting is important in the process of manufacturing (commercially and technologically) as a consequence of applying a variety of work materials for different part shapes (with regular and irregular geometry features), achieving dimensions to very close tolerances with appropriate smooth surface finishes.

In fact, metal cutting is not just an individual specific process - it is a group of certain processes. The common feature is the aim of generating the shape of the workpiece using a sharp cutting tool of harder material to form a final workpiece with precise dimensions or to improve the tolerances and quality of the surface finish of an already produced workpiece. To realize the metal cutting operations, relative motion is required between the workpiece and the cutting tool. The relative motion is performed (in most operations) by a primary and a secondary motion. The primary motion (called the cutting speed) is attained with the spinning of the workpiece, and the secondary motion (called the feed) is obtained by the linear movement of the cutting tool (Fig. 1(a)).

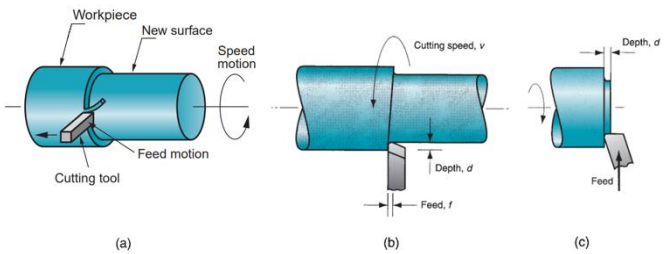

Fig. 1 *(a) Creating a shape in metal cutting by turning, (b) Turning cutting conditions, and (c) Facing cutting conditions*

Conclusively, the primary motion is accomplished at a certain cutting speed (*v*). In addition, the tool must be moved laterally across the work. This is a much slower motion, called the feed (*f*). The remaining dimension of the cut is the penetration of the cutting tool below the original work surface, called the depth of cut (*d*). Collectively, speed, feed, and depth of cut are called the cutting conditions [2].

Here are discussed cutting conditions for turning and facing (as one of the most common types of metal cutting) in more detail.

In turning, the workpiece revolves around its central axis. The cutting tool moves along the axis of rotation at a constant speed, removing excess material to form a cylinder, cone, or surface with a more complex profile. The rotating workpiece performs the speed motion, and the cutting tool achieves the feed motion by moving at a slow pace in a direction that is parallel to the workpiece's axis of rotation. In facing, the perpendicular movement of the cutting tool to the axis of rotation of the workpiece removes excess material from the workpiece's end and/or shoulder to create a new smooth surface. The cutting conditions for turning and facing are illustrated in Figure 1(b) and Figure 1(c), respectively. A typical unit used for cutting speed is [m/min], for feed is [mm/rev] and for depth of cut is [mm].

The cutting conditions in turning and facing generally incorporate the speed motion combined with a feeding motion and depth of cut to create the correct shape of the workpiece by the geometry of the cutting tool and its penetration into the work surface. The cutting tool has just one or even more sharp cutting edges. It is made of a material harder than the workpiece material. The purpose of the cutting edges is to separate a chip from the current workpiece in order to generate a new surface.

The surface of the tool over which the chip flows is known as the rake face. The cutting edge is formed by the intersection of the rake face with the clearance face or flank of the tool. The rake angle is measured from a line parallel to the axis of rotation of the workpiece. A positive rake angle is one where the rake face dips below the line, but the greater robustness of tools with a smaller rake angle leads in many cases to the use of a zero or negative rake angle. The tool terminates in an end clearance face, which is also inclined at such an angle as to avoid rubbing against the freshly cut surface. The nose of the tool is at the intersection of all three faces and may be sharp, but more frequently there is a nose radius between the two clearance faces [3].

Performing the operation with a positioned cutting tool relative to the workpiece requires a compatible machine tool. A machine tool, as a term, is applied to any power-driven machine that realizes a machining operation. It also indicates metal forming and metal

cutting processes. The requirement of the machine tool is to provide power for the operation at the determined speed, feed, and depth of cut related to the rotating workpiece and the movement of the cutting tool. The traditional machine tools used to implement the process of turning and facing are lathes. Instead of controlling the tool machine and the operation by a human operator who changes the cutting tool and sets the cutting conditions, a modern form of control (as a form of automation) is computer numerical control (CNC), in which the operation is controlled by a program of instructions. Despite the particular operation and the level of control, appropriate power is required to accomplish the activities in order to perform the exact operation.

2. Research

The purpose of this research is to determine how the required power of the electric motor on the CNC Spinner EL-510 lathe (with a maximum power of the main motor of 13,4[kW] and a mechanical efficiency of 80%) affect turning and facing operations when the work material, cutting tool, and cutting conditions are identical. The specified work material is C1430 (corresponding to the JUS C.B9.021 Standard for Heat - treatable Steels) with a hardness of 172 HB. The applied cutting tool is a combination of a CNMG 120408-PM 4325 indexable insert mechanically clamped into a PCLNR 2525M 12 shank tool (see Fig. 2). The cutting tool has the following elements of geometry: an approach (or cutting edge) angle of 95º, an entering (or lead) angle of -5º, an orthogonal rake angle of -6º, a clearance angle of 0º, and a corner radius of 0,8[mm].

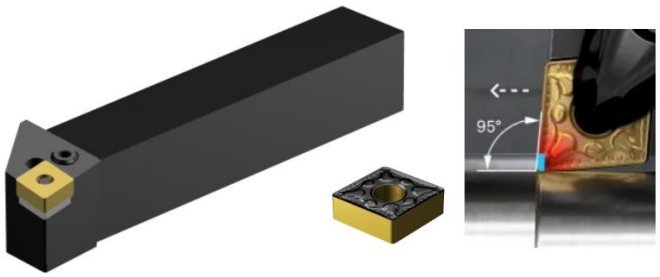

Fig. 2 *The Cutting Tool*

The corresponding grade number of surface roughness to the geometric tool factors is N10, and the appropriate value for the average roughness is 3,2 [μm]. The chosen cutting feed to achieve the defined surface quality is 0,83 [mm/rev]. The depth of cut is from 0,5 [mm] to 3 [mm] and it changes every 0,5 [mm] in order to calculate the essential motor power for turning and facing operations. The proper cutting speed is 180 [m/min] up to 1 [mm] depth of cut, and as the depth of cut increases from 1÷3 [mm], the cutting speed decreases to 140 [m/min].

The power required to operate the machine tool is greater than the power delivered to the cutting process because of mechanical losses in the motor and drive train in the machine [4].

The total product of the depth of cut, cutting speed, feed and the specific power coefficient for a particular operation gives the power required to perform the turning operation, while half the product gives the power required to perform the facing operation.

For turning:

(1) $$P_R = d \cdot v \cdot f \cdot p$$

where P_R is the power required to perform the turning operation, d - depth of cut, v - cutting speed, f – feed, p - specific power coefficient for a particular operation.

For facing:

(2) $$P_R = \frac{d \cdot v \cdot f \cdot p}{2}$$

where P_R is the power required to perform the facing operation, d - depth of cut, v - cutting speed, f – feed, p - specific power coefficient for a particular operation.

As a result of mechanical losses in the motor and drive train in the machine, the total required power is greater than the required power to perform the operation, and these types of losses can be estimated with the mechanical efficiency of the lathe:

(3) $$P = \frac{P_R}{E}$$

where P is the total required power, P_R - power required to perform the operation, E - mechanical efficiency of the lathe.

3. Results and discussion

Considering the specified work material, cutting tool, cutting conditions, and mechanical efficiency of the lathe, Table 1 lists (and Fig. 3 shows) the required power to perform turning and facing operations.

Table 1: *Required power for turning and facing operations*

d [mm]	0,5	1	1,5	2	2,5	3
f[mm/rev]	0,83	0,83	0,83	0,83	0,83	0,83
v[m/min]	180	180	140	140	140	140
P_R [kW] – Turning	4,78	9,56	11,16	14,87	18,59	22,31
P[kW] – Turning	**5,98**	**11,95**	**13,95**	**18,59**	**23,24**	**27,89**
P_R [kW] – Facing	2,39	4,78	5,58	7,44	9,3	11,16
P[kW] – Facing	**2,99**	**5,98**	**6,98**	**9,3**	**11,63**	**13,95**

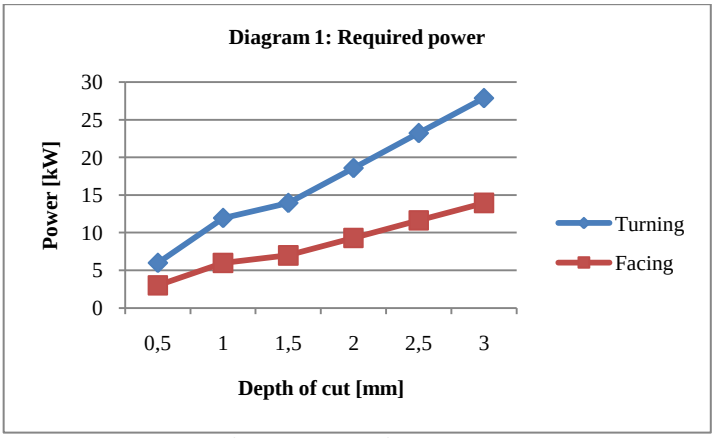

Fig. 3 *Required power for turning and facing operations on the CNC Spinner EL-510 lathe*

Turning and facing, as different types of metal cutting processes, require various values of motor power to perform the removal of a unit volume of metal during the process. Using this measure, turning and facing can be compared in terms of power requirements for identical work material, cutting tool and cutting conditions. The required power to accomplish a particular turning and facing operation (considering the results presented in Table 1 and Diagram 1) depends on the value of the depth of cut.

With the intention of increasing depth of cut, increasing motor power is required in performing these operations. The essential motor power is different in the two cases.

Considering that turning is a process of material removal with a cutting tool parallel to the rotation axis of the workpiece and facing is a process of material removal with a cutting tool perpendicular to the rotation axis of the workpiece, with turning the diameter of material is removed and with facing the length of material is removed.

The turning operation reduces the diameter of the workpiece from its original diameter to a final diameter, also known as the depth of cut. Actually, the depth of cut is the radius of the workpiece around which excess material is removed.

The total removed material during the process of turning is the sum of the two radiuses, i.e., it is a process of removing material from both sides of the workpiece, which results in a duplicated value of the depth of cut. On the other hand, in a facing operation, the cutting tool moves from the outer diameter of the workpiece towards the center (or inner diameter), removing a single value of the depth of cut.

Therefore, the power required to perform the turning process is two times higher than the power required to perform the facing process.

4. Conclusion

For the specified CNC Spinner EL-510 lathe's motor power of 13,4 [kW], it is recommended to perform turning up to a maximum of 1 [mm] and facing up to a maximum of 2,5 [mm] depth of cut. It is important to emphasize that to complete turning and facing operations in the same circumstances for higher values of the depth of cut, it is crucial to apply a higher power rating electric motor.

5. References

[1] Schey, J. A. *Introduction to Manufacturing Processes*, 2nd ed., McGraw Hill, Singapore, 1987, pp.442

[2] Groover, M. P. *Fundamentals of Modern Manufacturing: Materials, Processes, and Systems*, 4th ed., John Wiley & Sons, United States of America, 2010, pp.487

[3] Trent, E., and Wright, P., *Metal Cutting*, 4th ed., Butterworth–Heinemann, United States of America, 2000, pp. 11

[4] Groover, M. P. *Fundamentals of Modern Manufacturing: Materials, Processes, and Systems*, 4th ed., John Wiley & Sons, United States of America, 2010, pp.498

[5] Kaushish, J. P. *Manufacturing Processes*, 2nd ed., PHI Learning, New Delhi, 2010

[6] Ostwald, P. F., and Munoz, J. *Manufacturing Processes and Systems*, 9th ed., Wiley India, New Delhi, 1997

[7] Cvetkov, S. *Metal cutting and plastic deformation*, Goce Delcev University, Stip, 2014 [In Macedonian]

[8] Cvetkov, S. *Practicum for metal cutting and plastic deformation*, Goce Delcev University, Stip, 2015 [In Macedonian]

Application of polymer composites in moving joints machines of the fat and oil industry

Oleksii Derkach, Dmytro Makarenko, Yevhen Muranov, Antonina Yashnova., Polina Derkach
Dnipro State Agrarian and Economic University, Dnipro, Ukraine
e-mail: flymakd@gmail.com, derkach_dsau@i.ua

Abstract: *The expediency of using parts made of polymer composites in moving joints of machines in the oil and fat industry is shown. The use of experimental moving joints provided an increase in the resource from 500 hours to 1080 hours minimum. Diagnostics of experimental moving joints revealed that some of them have signs of transfer of the composite material to the steel shaft. This is explained by the following factors: the presence of the transfer effect and operation at high temperatures of 140 °C. The operating modes of the equipment are maintained. Most of the experimental parts made of polymer-composite material are in a running-in state, as wear has not been recorded in them.*

KEYWORDS*: POLYMER-COMPOSITE MATERIALS, MOVABLE COUPLINGS, DURABILITY, OIL AND FAT INDUSTRY, SCREW CONVEYORS*

1. Introduction

Ensuring food safety is one of the primary tasks for any country. The branch of processing of agricultural products occupies the main place in solving the specified problem. For this purpose, at processing enterprises, use a variety of equipment and equipment that requires special conditions of use, which is related to work with food products. Therefore, first of all, nessesery pay attention to compliance with the safety requirements of the obtained products, and only then to their cost price. Conveyors of processing enterprises, depending on the characteristics of the transported material and the conditions of the technological process, can be divided into: inertial, suspended, scraper, plate, belt, screw, roller, etc. [1]. Each of them has its advantages and disadvantages, but in the oil and fat processing industry screw or screw conveyors have become the most common.

2. Statement of the problem

Screw conveyors have become widely used in the production and processing of oil and fat products. Their main advantage is the simplicity of construction and low cost [1]. Most scientific research is aimed at increasing the productivity of conveyors or the wear resistance of their working bodies [2-4]. Production processes in oil and fat industry shops involve the movement of technological materials over considerable distances. Therefore, structurally, the conveyors are made with a large number of bearing supports. Theese bearing require careful maintenance in the form of periodic maintenance, diagnostics or replacement. This leads to periodic stops of transportation lines for planned and preventive repairs. Such a system of operation of conveyors reduces the volume of products produced by enterprises for a certain period.

The main elements of moving joints that require systematic and frequent maintenance or replacement are bearing supports. In the production of sunflower oil, screw conveyors are used, which, according to the technological process, must transport sunflower pulp at temperatures of 90...95 ºC and higher; the rotation frequency of the conveyor shaft is 77 min^{-1}; the distance between bearing supports is 3 m; the productivity of conveyors is not less than 5 t/h. This additionally imposes certain restrictions on the use of materials for bearing assembly supports.

There are known solutions for the use of supports made of wood in the indicated moving joints. The advantage of such supports is their low cost, and the disadvantages include low durability. In order to slightly increase the service life of the supports, it is necessary to additionally heat-treat has been wooden bearings in lubricants. However, this does not ensure compliance with reliability requirements, and some of the wooden bearings fail even before the regular maintenance according to the regulations, which leads to an unplanned stoppage of production. One of the ways to solve this problem is the use of structural materials capable of operating in friction mode without lubrication at temperatures above 95 ºC. At the same time, products of wear or friction of such materials must be absent or be safe for use in the food industry. The positive experience of using polymer composite materials (PCM) in the construction of agricultural machines [5-7], industrial production equipment [8] and the food industry [9] is known.

3. Materials and equipment

The tribological properties of PCM during friction without lubrication were determined on a friction machine of disc type (Fig. 1) according to the method [10].

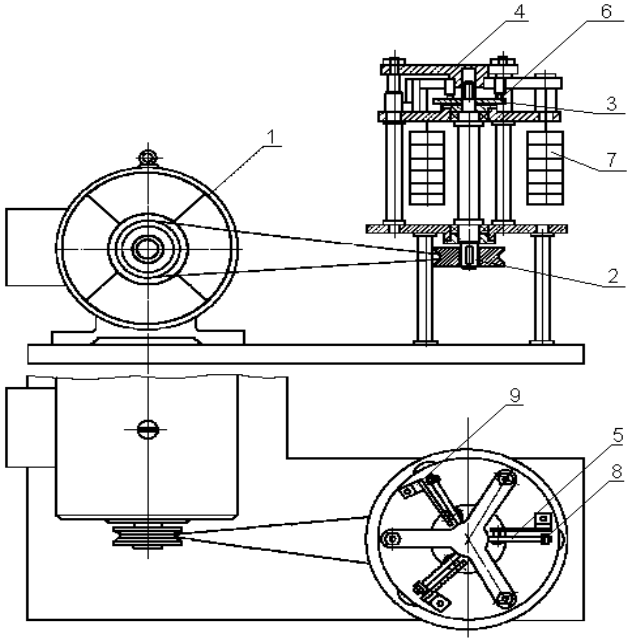

Figure 1 *– Friction disc machine.*
1 – electric motor; 2 – pulley; 3 – steel disk; 4 – cross; 5 – lever; 6 – carbon plastic

Modes of operation: sliding speed of the sample on the metal surface - 1.0 ... 2.5 m/s; pressure on the sample - 1.0 MPa; surface roughness of the metal disc – Ra = 0.63 μm; the friction path is 10,000 m. The test was carried out under two additional conditions: with removal of the transfer film from the surface of the metal disk and without removal of the transfer film. As can be seen from fig. 2, the temperature in the contact zone is lower than the friction condition in the presence of the transfer film. This is explained by the lower coefficient of friction on the film [5]. Thus, the operation of PCM parts based on polyamide reinforced with carbon fibers should not require additional care for the technical condition of the shafts.

For the production of sliding bearings of screw conveyor supports, PCM of our own production based on polyamide 6.6 reinforced with carbon fiber was chosen. This material is workable at PV factor up to 2 MPa·m/s in friction mode without lubrication and at temperatures in the friction zone up to 120 ºC. The material was obtained on an experimental extruder equipped with two dispensers (Fig. 3).

The extruder is made with two dispensers - for polymer material and carbon fibers; with the help of a worm with a diameter of 45 mm, the dosed mass is mixed and transported through four heating zones. Then, through the die, the composite is pressed into a bath with water, in which cooling is carried out, and then the

already cooled strands are crushed into granules on a granulator. Residues of moisture from the obtained PCM were removed by drying in a thermal cabinet at a temperature of 120ºC for at least 3 hours. The dried granules were processed into finished parts by the method of pressure casting in a press mold on a hydraulic casting machine (Fig. 4).

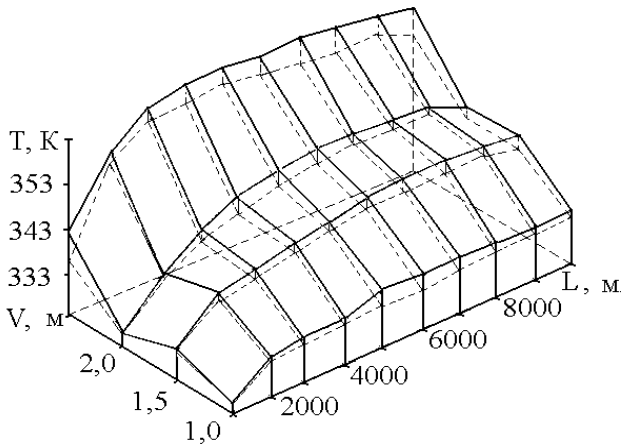

Figure 2 *– The influence of sliding speed and friction path on the temperature of PCM in the contact zone along the film (- - -) and without film (□)*

Figure 3 *– Experimental extruder*

Figure 4 *– PL-32 injection molding machine*

The technology of processing granules into products was carried out under the following conditions: the pressure of injecting the material into the mold was 11 MPa, the temperature of the melt was 255...260 ºC, the temperature of the mold was 75...80 ºC, the duration of exposure under pressure after filling the mold was no less than 30 seconds.

4. Results of production tests

Experimental sliding bearings had the form of semi-annular elements obtained by cutting a part (blank) of an annular shape (Fig. 5). The specified elements are installed as sliding bearings in the supports of the screw conveyor, which was used to transport the pulp of sunflower seeds for subsequent removal of oil from it.

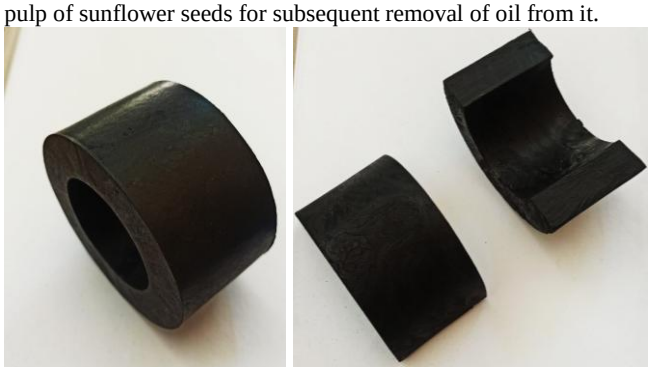

Figure 5 *– Experimental elements of the bearing supports of the screw conveyor: a – part (workpiece) of a cylindrical shape made of PCM; b – experimental sliding half-bearings*

Experimental elements of bearing support of the screw conveyor worked for 1080 hours without maintenance or failures. After their defecting, a partial transfer of PCM to the conveyor shaft of those supports located in the pulp supply area after heating was recorded. This may indicate a violation of the technological process of heating the transportation product (pulp) according to the temperature criterion. It was established that the temperature in the contact zone of the bearings was up to 135...140 ºC. After dismantling the supports with experimental sliding bearings, our was found that it had wear of up to 0.1 mm, which indicates that they were in a running-in condition. The resource of such minimum elements is increased by 2.5...3 times, compared to elements made of wood. The technological mode is maintained. The proposed technical solution is protected by a Ukrainian utility model patent [11].

It was established that additional heat treatment of PCM parts, in a lubricant environment, does not significantly affect the amount of wear and strength characteristics, compared to untreated parts. Therefore, the specified technological operation was not carried out for other batches of parts made of PCM.

5. Conclusions

The workability of PCM, based on polyamide 6.6 reinforced with carbon fiber, as a structural material for the elements of the bearing supports of the screw conveyor of the oil and fat industry has been proven.

The developed materials have significant corrosion resistance and do not damage steel welded parts, even under friction conditions without lubrication. The use of experimental parts makes it possible to realize the construction of bearing supports that do not require maintenance during the entire period of their operation.

The production of such bearings does not require significant expenditure of resources, and their use allows to increase the service life of bearing units by 2.5...3 times compared to the use of standard elements made of steel or wood.

6. References

1.Datsyshyn, O., Tkachuk, A., Hvozdiev, O. Tekhnolohichne obladnannia zernopererobnykh ta oliinykh vyrobnytstv: navch. posibnyk. Vinnytsia : Nova Knyha, 2009, 488pp.

2.Hrudovyi, R. Novi typy hvyntovykh mekhanizmiv z pokrashchenymy ekspluatatsiinymy kharakterystykamy. Visnyk Khmelnytskoho natsionalnoho universytetu, V.1. (197), 2013, 24–27.

3.Hevko, R., Rohatynskyi, R., Rozum, R., Klendii, M. Pidvyshchennia tekhnolohichnoho rivnia protsesiv zavantazhennia ta perevantazhennia materialiv u hvyntovykh konveierakh: monohrafiia, Ternopil: Osadtsa Yu.V., 2018, 180 pp.

4.Orobinskyi, V., Heruk, S., Hrudovyi, R. Shliakhy pidvyshchennia znosostiikosti shnekovykh robochykh orhaniv. Visnyk Lvivskoho natsionalnoho ahrarnoho universytetu: ahroinzhenerni doslidzhennia, Lviv: Lvivskyi natsionalnyi ahrarnyi universytet, №. 14, 2010, 282–291.

5.Derkach, O. Obhruntuvannia parametriv obertovykh elementiv robochykh orhaniv zernozbyralnykh kombainiv: Dys. kand. tekhn. Nauk, Ternopil, 2006, 182p.

6.Makarenko, D. Pidvyshchennia dovhovichnosti paralelohramnoho mekhanizmu posivnykh kompleksiv zminoiu konstruktsii rukhomykh ziednan, Dys. kand. tekhn. nauk, Kropyvnytskyi, 2018, 185pp.

7.Derkach, O., Buria, O. Pidvyshchennia tekhnichnoho rivnia elektro-, avtomobilnoho transportu ta silskohospodarskoi tekhniky za rakhunok vykorystannia novykh materialiv. Dnipropetrovsk, DSAU, 2011. 71pp.

8.Kabat, O. Naukovo-tekhnichni osnovy tekhnolohii vyhotovlennia termostiikykh polimernykh kompozytsiinykh materialiv trybotekhnichnoho pryznachennia. Dnipro, 2021, 350pp.

9.Vykorystannia teflonu v kharchovii promyslovosti. https://novaflon.com/ispolzovanie-teflona-v-promishlenosti-ua

10. Burja, A., Molchanov, B., Trenie i iznos poliamida-6 i ugleplastika na ego osnove. Trenie i iznos, V.13, №5., 1992, 90-94.

11. Opornyi pidshypnyk kovzannia. Ukrainian utility model patent № 151145, F16C17/00, 08.06.2022, Biul. 23/2022. 3pp.

Dual fuel four stroke lean burn engine supercharging system operational features

Delyan Hristov[1]
Nikola Vaptsarov Naval Academy Varna, Bulgaria[1]
d.hristov@nvna.eu[1], d.hristov@naval-acad.bg[1]

***Abstract**: In the present publication are considered the features of the dual fuel four stroke lean burn engines supercharging system operational features. The supercharging system control means are analysed and performance data is collected from an engine in operation on an offshore vessel. The data obtained from the engine in operation is analysed, processed and figures of related parameters are obtained. The latter are analysed in relation to the importance of the supercharging technical condition. Conclusions and recommendations are stated as a final outcome.*
***Keywords**: DUAL FUEL LEAN BURN FOUR STROKE MARINE ENGINE, SUPERCHARGING SYSTEM CONTROL, WASTE GATE, MARINE TURBOCHARGER SPEED CONTROL*

1. Introduction

With the present energy transition forced changes in the marine industry there are new dual fuel engines introduced in the ship power plants, which have different behavior on gas mode operation, compared with the conventional diesel engines. As a matter of fact, these engines operate on Diesel cycle while operating on liquid fuel and change to Otto cycle while on gas.

There are specifics in the operation of the subsystems of the Lean burn Otto cycle engines such as the gas supply and the supercharging system. The operation of the supercharging system on gas mode is critical for the ability of the engine to run safe and in case of system deteriorated condition it could be even impossible to run on gas.

The information related to the specifics of the supercharging systems on the dual fuel four stroke engines are well known to the engine manufacturers but mainly remain in their envelope. The general knowledge for the supercharging systems of the dual fuel engines on gas mode should be populated and better disseminated.

In this publication the aim is to be presented the features of the supercharging system control components and the logic of the control system dealing with the air-fuel ratio on gas mode of operation. The tasks linked to the aim stated are to be collected data for the charge air system operation on dual fuel engine Wärtsilä 34DF and the data to be analyzed in respect to the features of the charge air pressure control.

2. The dual fuel four stroke engine type Wärtsilä 34DF

The object in the publication is a four-stroke dual fuel engine Wärtsilä 34DF operating in the medium speed range has the characteristics as shown in Table 1 [1].

***Table 1:** Engine 34DF characteristics*

Wärtsilä 34DF	
Cylinder bore	340 mm
Speed	650 - 720 RPM
Power output	5760 kW
Turbocharger maximum RPM	32500

The engine is part of the ship power plant of an offshore supply vessel and operates in the range of 650 – 720 RPM depending on the mode of operation. There are two turbochargers Napier NT 1-10 co-operating with the engine with specific control system components – bypass valve and waste gate system, dealing with the pressure control in two different modes – nominal and low load operation.

A sectional view of the V-type engine is shown on a figure 1 [2]. It is trunk engine, twin bank with scavenge manifold positioned between the two engine blocks.

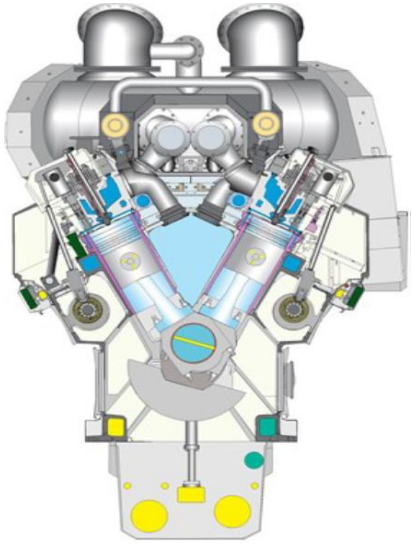

***Fig. 1** Sectional view of V34DF [2]*

2.1 Engine turbocharging control system

The function of the bypass valve is to increase the pressure of the air charge, supporting the operation of the turbocharger turbine at low engine load. It is positioned before the air cooler of the engine in order to recirculate part of the air flow. By a command from the engine control system to open it, it diverts part of the still uncooled portion of air directly to the inlet of the turbine side of the turbocharger, thereby helping to increase the turbine speed, followed by an increase of the charge air pressure in the receiver. This distinctive feature of the engine improves its performance at low loads by reducing the thermal load and avoids unwanted additional smoke creation.

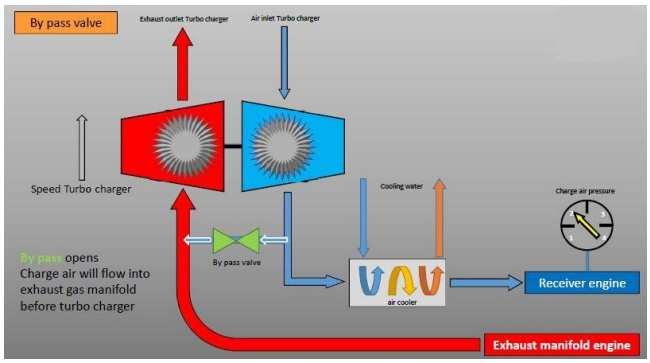

***Fig. 2 Charge air bypass valve** [2]*

The waste gate valve is installed in the exhaust gas flow path before the turbine side of the turbocharger. One of its functions is a safe activation in a high engine load mode [2]. Its function is to be opened for bypassing part of the flow of exhaust gases off the turbine upon reaching the critical values in terms of revolutions per

minute for the turbocharger shaft and charge air pressure in the receiver

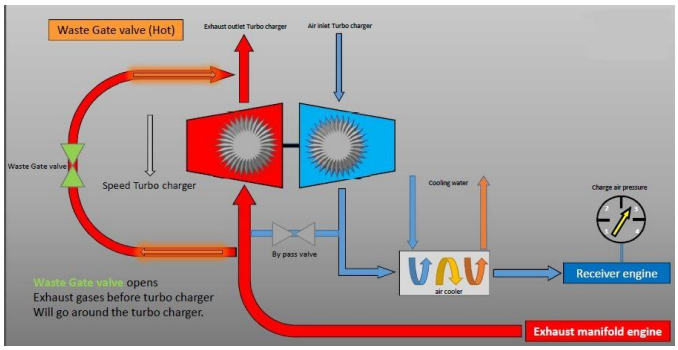

Fig. 3 *Waste gate valve [2]*

In addition, the main distinguishing feature of the waste gate is the control of the charge air pressure and thus the stability of the fuel ignition. By precisely adjusting its opening, the flow of exhaust gases entering the turbine side of the turbocharger unit is bypassed, by routing them directly to the funnel. In this way, regulation/reduction of the revolutions developed by the turbocharger is achieved, in a large range of the rotation speed and wide range of the engine power. This function determines the waste gate valve as a regulator of the maximum values of λ within the limits of a lean fuel-air mixture, preventing it from exceeding its upper limit, which would lead to problems in the combustion process, increasing the NOx formation and tending to engine knocking.

The waste gate valve control is carried out by the engine control system which monitors the value of the air pressure in the receiver and if the pressure of the charge air is higher than the set value it sends a command to gradually open the waste gate valve, until the correct pressure value set in the engine map is reached. In the event that the pressure drops below this value, the engine control system commands to gradually close the waste gate valve until the correct value of the charge air pressure is reached again. The control logic is implemented in the engine control system and no external regulators are needed [2].

3. Performance results of the turbocharging system

For the purpose of the task execution in this publication, there are collected the results of the performance of the supercharging system in variable modes from 25% to 100% load modes of the engine with liquid and gas fuel in use in actual operation of the engine, by using the engine monitoring system for data acquisition of the parameters. The condition of the engine could be evaluated as optimal as the data was attained on a mode of sea trials of the ship power plant. Due to the different control approach on both modes, there can be seen the significant differences in the supercharging system behavior. There are differences in the turbocharger performance due to the control action of the charge air bypass valve and the waste gate valve operation by the engine control system.

In table 2 are presented the results of the turbocharger RPM in the variety of the loads of the engine. It could be noticed that the revolutions of the turbocharger are higher on low load mode at gas fuel mode and tend to decrease at higher loads compared to the liquid fuel mode.

Table 2. *Turbocharger RPM*

Turbocharger RPM					
Load %	25	50	75	90	100
LNG	12315	20290	24340	25855	27045
MDO	8370	21560	25844	27845	29140

In the table 3 are presented the values of the charge air pressure in the scavenge air manifold in the both modes – liquid and gas fuel operation as the gas fuel supply pressure on gas mode of the engine.

Table 3. *Charge air and gas pressure*

Charge Air Pressure and fuel gas supply pressure (bar)					
LNG	0.4	1.39	2.46	2.93	3.35
MDO	0.15	1.61	2.88	3.64	4.12
GVU	**1.4**	**2.53**	**3.76**	**3.94**	**4.27**

The control positions of the waste gate valve and the charge air bypass valve for the liquid and gas fuel mode are shown on table 4 and table 5. It noticeable that the waste gate is utilized mostly on gas fuel mode and the charge air bypass valve is used on both modes mostly to facilitate the smokeless operation in low load operation.

Table 4 *Waste gate and charge air bypass valves control positions - gas*

Gas fuel mode operation					
Load %	25	50	75	90	100
Waste gate [%]	12	5	6	6	14
CA by-pass [%]	69	33	10	4	0

Table 5 *Waste gate and charge air bypass valves control positions - liquid*

Liquid fuel mode					
Load %	25	50	75	90	100
Waste gate [%]	0	0	0	0	8
CA by-pass [%]	31	37	20	8	0

3.1 Performance results analysis

A comparison of the RPM's of the turbocharger in both modes – liquid and gas fuel mode are shown on figure 4.

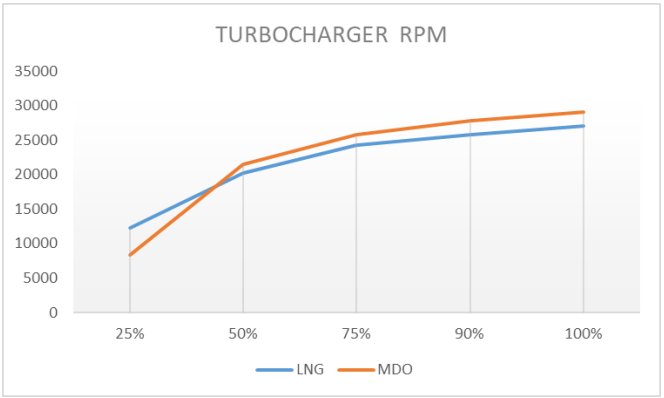

Fig. 4 *Turbocharger RPM comparison on gas and liquid fuel mode*

As it can be seen, there is a difference in the revolutions in low load of operation and the turbocharger is supported by the charge air bypass with intention to increase the turbine RPM. On the high load range, although the charge air bypass is still opened the waste gate allows part of the gases to go directly to the funnel thus controlling the turbocharger performance with relation to the charge air pressure control for the lean burn concept combustion execution.

On the figure 5 it can be seen the pressure developed by the turbocharger in both modes, compared to the fuel gas pressure supplied in the gas mode.

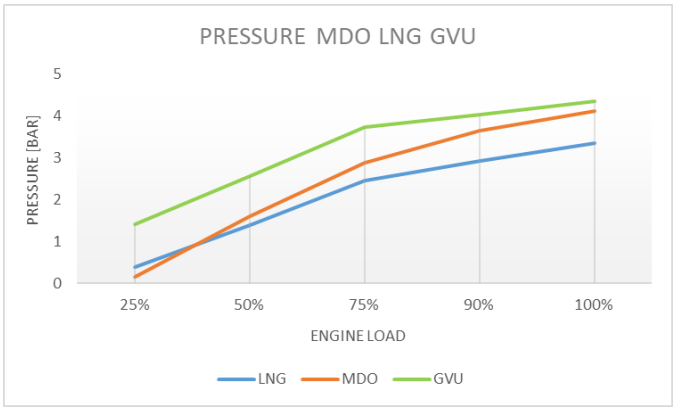

Fig. 5 *Charge air and gas pressure development*

The comparison of both lines with the orange and blue color on figure 5 shows the influence of the charge air control system on the performance of the system. The orange line representing the pressure development in liquid mode shows the simplified operation of the Diesel cycle engine compared to the gas fueled Otto engine with lean burn concept. Although there is surplus air in the combustion chamber of the engine it is not critical is it precisely metered to the fuel amount, so to obtain proper fuel-air ratio. Due to the non-homogeneous combustion of the Diesel cycle engines, there would be always rich fuel-air ratio areas in the combustion chamber which cannot be controlled due to the manner of fuel injection. It is the most significant difference with the presented subject engine in the publication. On gas mode the engine operates on homogeneous combustion which requires precise adjustment of the fuel-air ratio.

On figure 5 it could be seen another special feature of the gas fueled engine, the difference in the pressure of the charge air and gas fuel shown with blue and green color lines. There is strong dependence of the pressure difference between both fluids in the entire engine load range. The gas fuel pressure is kept higher with approximately one bar above the charge air pressure. In this relation the charge air pressure is controlled by the waste gate of the exhaust gases around the turbocharger turbine and the gas valve unit of the gas fuel system controls the supply pressure of the gas. Due to the specific mixing approach of the gas fuel and the air on gas mode it is necessary to have positive difference in the gas pressure compared to the air pressure in order to achieve proper routing of the flow of the mixture to the direction of the combustion chamber. The gas fuel is fed to the inlet charge air branch of the air manifold next to the inlet valve of the specific cylinder unit and to be sure that the gas will approach the combustion chamber the dosing gas valve has specific position and additionally the pressure must be kept with the difference described to not change the direction of the gas fuel aside from the combustion chamber to the scavenge manifold. If for any reason this pressure difference cannot be maintained there is direct safe issue with the gas operation of the engine.

On a figure 6 it is shown the opening value of the charge air bypass valve on gas mode of the engine. In an alignment with the intended use of the charge air bypass system the bypass valve is opened mostly in the low range load modes for the purpose of the smokeless combustion of the engine supported by the reverted flow of the hot charge air directly to the turbine side of the turbocharger. The bypass valve is fully closed at high load modes and supports the turbine in the mid and low range mode. It could be concluded that the by pass valve ability to support the turbine operation is similar to the control margin of the turbocharging system. If there is no sufficient air amount to be supplied to the turbine it would lead to smoke operation of the engine, especially in the low load ranges where the turbocharger operates with poor efficiency by default.

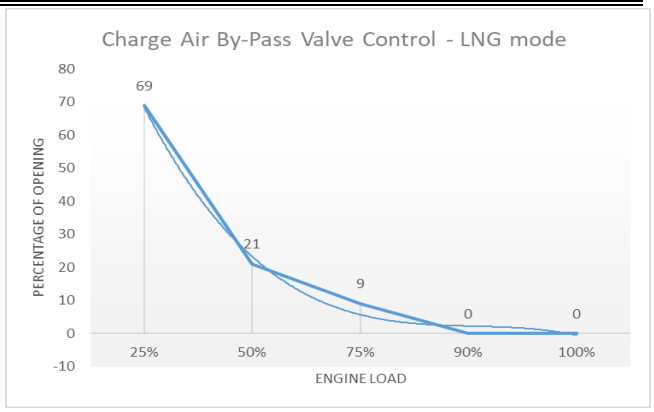

Fig. 6 *Charge air bypass valve operation*

On figure 7 it shown the waste gate valve operation in both modes – liquid and gas fuel mode.

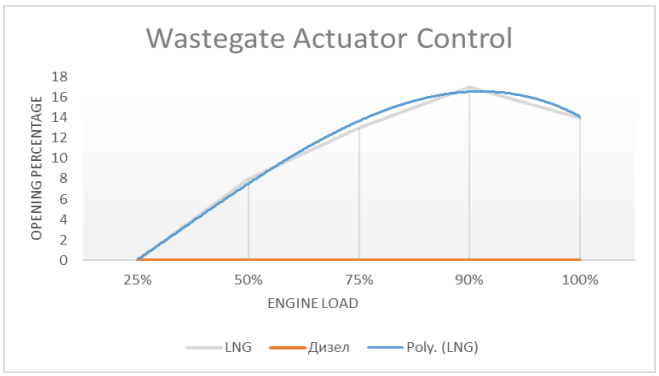

Fig. 7 *Waste gate valve operation on liquid and gas fuel mode*

The waste gate valve is used exclusively in gas fuel mode by the engine control system. As it was underlined its function is to keep the proper charge air pressure related to the engine load and the gas consumption, so to keep constant fuel-air ratio during gas mode operation. On liquid fuel mode the waste gate valve is closed, and the full capacity of the turbocharger is used to supply the engine with air. There is a possibility to use the waste gate as a safety device to redirect part of the gases on full load on liquid fuel mode in case of specific matching approach of the engine and the turbocharger by choosing smaller turbocharger for better performance in lower range of operation.

The core function of the waste gate is to act as pressure controlling device on gas mode, but it has strong dependence of the turbocharging system technical condition. The turbocharger must be able to keep its operation with control margin determined by the excessive efficiency for the waste gate opening. If there is no margin for opening the waste gate while the engine is operating on gas mode it could be impossible to keep the intended charge air pressure and respectively the fuel-air ratio in the specific mode, so the gas operation would become impossible.

The optimal condition figure of the waste gate valve position could be utilized as a reference condition for the turbocharging system deterioration. If there is excess fouling or there is marginal wear of the turbocharger components and the scavenge air system components it could be impossible to achieve the desired control of the turbocharger performance by opening the waste gate valve. The turbocharger must be kept in optimal condition for the smooth operation of the scavenge air control system. There must be considered variable factors which could influence the turbocharging system operation in different way than the considered in this publication. The margin for control is a must after all considerations.

4. Conclusions

In the publication are stated the special features of the turbocharging system of a dual fuel lean burn four stroke engine. The functions of the waste gate and the bypass valves are described in their critical minimum.

It could be considered that the dual fuel engines operate in two fundamentally different modes. On liquid fuel they are pure diesel engines and on gas fuel they are different engines. While operating on liquid fuel and not only there can be considered significant process of fouling of the turbocharger components. These components need to be in optimal condition for normal operation on gas mode. If there is a contradiction in this direction it must be expected that there will be deviation in the gas operation of the engine. It must be considered the proper maintenance of the engines and their subsystems as a critical requirement for the safe gas operation.

The experience with the diesel engines supercharging system could lead to poor results in the case of gas used as fuel [3]. The diesel engine could run in most of the cases even with turbocharging system in poor condition with some smoke and heat tensioning, but the gas fuelled engine cannot run in that way, just because of the engine control concept. The operation of relatively new engines is non problematic, but with the running hours stored there will be deviations of the technical condition which must be handled with the required attention from the engine operators.

5. Acknowledgements

The tasks in the publication to show the specifics of the turbocharging control system of the lean burn dual fuel engine is accomplished. There are shown the differences of the turbocharging system of the Diesel and the Lean burn concept engine with the potential weak points to be considered during the operation of such engines. The data analysis in the publication could be considered as a reference for the expected performance of the newly introduced dual fuel engines.

The data acquired from real ship power plant is the most realistic figure which could be seen in the real practice of the marine engineers working on natural gas fuelled ships.

The outcome of the publication could be beneficial to the marine engineers to better understand, clarify and explain the differences in the operation of the dual fuel and the Diesel four stroke engines in relation with the charge air system.

6. References

1. Anonimous, Wartsila land & sea academy, *Wartsila 34DF engine operation manual*, 2010
2. Anonimous, Wärtsilä, Engine Operation and Maintenance Manual (O&MM) - W9L34DF, 2016
3. Popov, D., Study of the effects on engine fuel consumption generated by turbocharger performance, Trans Motauto World 7.3 (2022): 132-135.

The Effect of Vanadium, Niobium and Boron on Microstructure, Mechanical and Corrosion Properties of High-Chromium White Cast Irons

Kemal Delijić[1,*], Mirjana Filipović[2]
University of Montenegro, Faculty of Metallurgy and Technology, (MNE)[1]
University of Belgrade, Faculty of Technology and Metallurgy, (SRB)[2]
kemal@ac.me

Abstract: *The influence of the vanadium, niobium and boron addition on properties of high-chromium white cast iron alloys for grinding balls is investigated in this paper. These alloying elements were individually added to the high-chromium white cast iron alloys with monitoring of changes in microstructure, corrosion rate, and mechanical properties in the as-cast conditions. The microstructure in all tested alloys consists of primary austenite dendrites and eutectic colonies, which consist of M_7C_3 carbides and austenite. The addition of V, Nb or B affects, to a greater or lesser extent, the size, morphology and volume fraction of both primary austenite dendrites and eutectic colonies. Samples of iron alloyed with vanadium and boron have a much finer structure than unmodified (base) alloy and niobium alloyed iron sample. Vanadium affects the decrease in the volume fraction of the primary austenitic phase, and the increase in the volume fraction of eutectic colonies, and thus the eutectic carbide phase in hypoeutectic alloys of high-chromium iron. The tested alloys have a comparable values of average hardness in the cross section of cast balls, as well as compressive yield strength, noting that the addition of vanadium increases the hardness, while boron addition increases the compressive yield stress. The single addition of all of three tested alloying elements shifts the corrosion potentials (and Tafel curves) of modified high-chromium white irons toward less negative values. The most favorable values of mechanical and corrosion properties were measured for the iron modified with 0.021 % of boron.*
Keywords*: HIGH-CHROMIUM WHITE CAST IRON, GRINDING BALLS, VANADIUM, NIOBIUM, BORON, CORROSION*

1. Introduction

High-chromium white irons represent the third generation of wear-resistant white irons, developed after unalloyed white cast and nickel-alloyed type of irons, with a favorable ratio of abrasion wear and toughness, which makes them very attractive for use in the most demanding conditions of grinding and crushing of various materials [1,2]. This class of alloys have a wide range of applications in mining, metallurgy, cellulose and paper production, construction industry or wherever is a need for grinding huge quantities of material by crushing or milling. The properties of these irons are influenced by the type, hardness, morphology, distribution, volume fraction and orientation of eutectic carbides, as well as the matrix microstructure, which supports the carbide phase-[3].

One of the possibilities of improving the performance of high-chromium white cast irons is alloying with carbide-forming elements, such as vanadium [4, 5, 6], niobium [4, 6, 7, 8], and boron [10, 11, 12]. These alloying elements bind carbon in the form of carbides different from cementite, with higher hardness and a much more favorable morphology, and reduce the carbon content in the matrix enabling the simultaneous improvement of both impact toughness and resistance to abrasion wear [4, 13, 14]. Refining the eutectic carbide structure by creating finer, more globular carbides, is also a possible strategy to improve the toughness of white iron alloys, as well as the wear resistance [15, 16]. The influence of certain alloying elements, which are the subject of the analysis in the paper, can be briefly described as follows. Increasing in carbon and chromium content in white cast iron causes the change of eutectic carbide from M_3C to M_7C_3 [17]. Niobium has a limited solubility in M_7C_3 carbides. The formation of NbC before M_7C_3 carbide [7] causes a decrease in the carbon content of the melt. Since carbon mainly determines the volume fraction of the carbide phase in the structure of high chromium iron, the amount of M_7C_3 carbide will decrease with increasing of niobium content in the alloy. Concentration of vanadium and boron in M_7C_3 carbides increases with the increase of their content in the alloy. Increase in vanadium content in high-chromium iron, affects the changes in volume fraction of eutectic M_7C_3 carbides [5, 6, 18], although the data in the literature are not consistent: according to [6] increasing of vanadium content decreases the amount of eutectic M_7C_3 carbides, but according to others [5, 18], it increases. Boron changes the morphology, size and volume fraction of M_7C_3 carbide [11, 20]. By adding up to 0,15% boron to high-chromium iron, the structure becomes much finer and the volume fraction of the eutectic, or M_7C_3 carbide, increases.

The corrosion behavior of these materials does not depend only on the content of Cr and C individually, but primarily on the ratio of their content Cr/C, as well as on the ratio of Cr content in carbides, and in the matrix (Cr_{M7C3}/Cr_{matrix}) [21]. The addition of other alloying elements, such as Si, Mo, Ni, Cu, V, Ti, etc., also affects the corrosion behavior. The microstructure of white cast iron consists of a ductile γ-Fe phase and various carbides (M_7C_3, $M_{23}C_6$), which provide an extremely high level of hardness. Wear resistance depends on the volume fraction of carbide in the structure, while the Cr content in the Fe-base affects corrosion behavior and corrosion resistance [21]. When the matrix contains a sufficient amount of chromium (Cr > 12%), a very thin layer of passivating oxide nano-film (Cr_2O_3) is formed on the surface, which protects these alloys from corrosion [23]. Increasing the carbon content provides a higher proportion of carbides in the structure, but at the same time worsens the corrosion characteristics of white cast iron [21]. If the Cr/C value decreases, the amount of Cr bound in the carbides is significant, the chromium-depleted zone around the carbide particles expands, due to which the sensitivity to corrosion increases [22]. The improvement of corrosion resistance of this type of alloys can be also achieved when the particles of the secondary phases in the structure are approximately spherical, and when their content/volume fraction in the structure, is optimal [23]. In this way, the formation of a micro galvanic cell becomes difficult, or pitting corrosion is prevented.

The aim of this paper is to present some results and considerations related to the influence of the single addition of vanadium, niobium and boron on microstructure, corrosion and mechanical properties of high-chromium white cast iron alloys for grinding balls.

2. Experimental procedure

The chemical composition of tested alloys is listed in Table 1. The melting of high chromium white irons, individually alloyed with vanadium, niobium and boron, was performed in induction furnace. Grinding balls with 60mm of diameter were cast in water cooled permanent molds. The casting temperature was 1470 ^oC - 1490 ^oC and the mold temperature was 130 ^oC -140 ^oC. The balls were kept in the mold for 3 minutes, the mold was subsequently opened, cast balls were taken out and further cooled in ambient air. The samples were tested in the as-cast conditions. The microstructure of the samples was investigated by conventional optical microscopy and scanning electron microscopy. Corrosion behavior was evaluated by linear and potentidynamic polarization electrochemical methods in fresh water, using the potentiostat/galvanostat Princeton Applied Research PAR 273 with the software SoftCorr 352 II (standard saturated calomel electrode; auxiliary graphite electrodes.). Properties of fresh water: pH=7,78; Fe <0,003mg/l; chlorides 6,54 mg/l; nitrates (NO_3^-) <1,00 mg/l;

sulphates (SO_4^-) 3,12 mg/l; potassium (K^+) 0,562 mg/l; magnesium (Mg^{++}) 3,1 mg/l; sodium (Na^+) 0,798 mg/l; calcium (Ca^{++}) 55,86 mg/l; Fe < 0,003 mg/l.

Table 1. Chemical composition of tested alloys

Element, wt%	Base alloy[1]	HCCI balls alloyed with vanadium	HCCI balls alloyed with niobium	HCCI balls alloyed with boron
C	2,91	2,91	2,86	2,64
Si	0,83	0,92	0,95	1,28
Mn	0,79	0,81	0,71	0,80
P	0,029	0,030	0034	0047
S	0,016	0,017	0,016	0,013
Cr	17,83	17,95	16,42	14,28
Mo	1,15	1,14	1,13	1,08
Cu	0,84	0,87	0,95	0,92
Ni	0,11	0,10	0,12	0,10
B	<0,002	<0,002	<0,002	**0,021**
V	0,041	**1,23**	0,074	0,072
Ti	0,021	0,045	0,068	0,109
Nb		0,011	**2,43**	0,056
W	<0,001	<0,001	<0,001	<0,001
[1] high chromium cast white iron, chemical composition ASTM A532-IIE				

Mechanical properties were analyzed by: measuring of Rockwell hardness and calculating the average values for the cross-section of the grinding balls; determining the compressive yield stress on cylindrical samples of 7mm of diameter and 14mm of height, using the FPZ-100 universal tensile/compressive testing machine.

In order to compare the properties of novel cast balls, casting and testing of high chromium white iron "base alloy" balls (chemical composition defined by ASTM A532-IIE) were performed under the same conditions.

4. Results

Microstructures of tested as-cast balls, at the surface and in central zones on the cross-sections, are presented in Fig. 1. The microstructure of the base high chromium white iron balls is also shown with the aim of more clearly observing the changes caused by alloying with different carbide-forming elements, Fig. 1.a. The structure consists of primary austenite dendrites and eutectic colonies, which consist of M_7C_3 carbides and austenite in all tested alloys. The alloying elements, vanadium, niobium and boron affect to a greater or lesser extent the size, morphology and volume fraction of both primary austenite dendrites and eutectic colonies. Niobium affects the smallest influence on the size of the micro-constituents present in the structure, noting that it affects the morphology of the primary austenite dendrites, and thus the morphology of the eutectic colonies, Fig.1.c. Significantly finer structure is noticeable in vanadium alloyed irons if compared to the base alloy and the alloy with niobium. There is a difference in the size of the micro-constituents in the structure from the surface to the center of the balls, but it is much less pronounced in the alloys with vanadium compared to the base alloy, Fig.2. Niobium affects the volume fraction of phases present in the structure, changes the morphology of both primary dendrites and eutectic colonies (Fig. 1.c). The shape of the eutectic colonies is determined mainly by the volume fraction and morphology of the dendrites of the primary austenite. The size of the particles increases from the surface to the central zone of balls, with the largest changes in their size in the region from the surface to a distance of 5 mm from the surface, Fig. 3. The volume fraction of dendrites of primary austenite is higher, while the amount of eutectic, and thus of M_7C_3 carbide, is lower in Nb-alloyed iron if compared to the base alloy. The presence of NbC carbide particles, of different morphologies and sizes, in the microstructure of niobium-alloyed iron can also be indicated (Fig. 3 and Fig. 4). NbC particles are mostly located in the surface zone of austenite dendrites, or precisely at the border of dendrites and eutectic M_7C_3 carbides, and very rarely in the central zone of dendrites. In certain regions, accumulations of large NbC carbide particles can be observed.

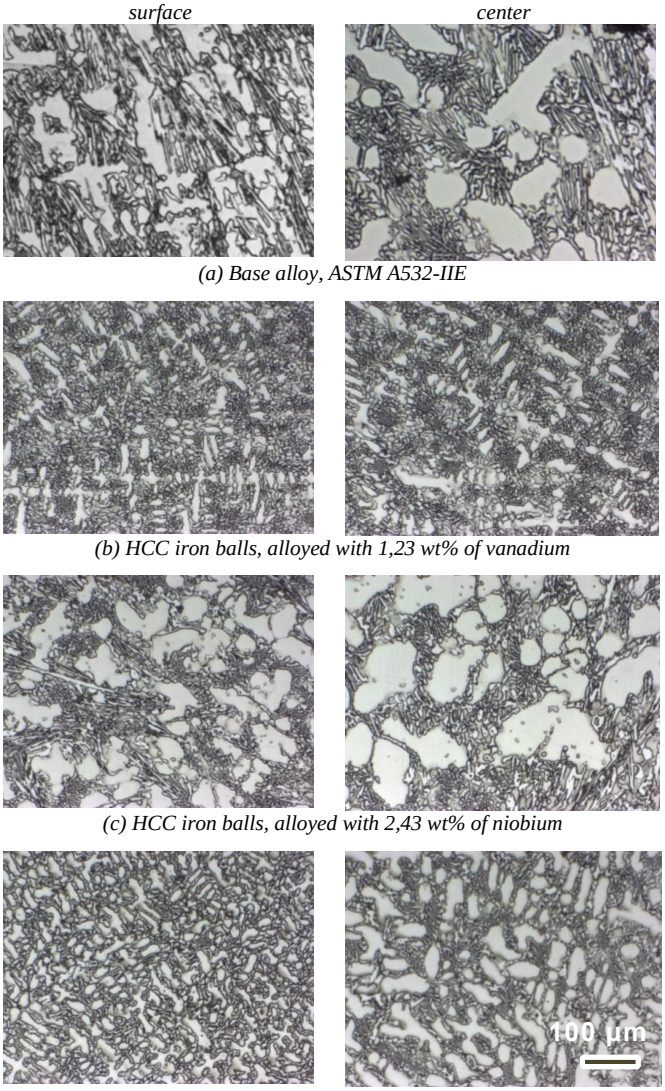

(a) Base alloy, ASTM A532-IIE

(b) HCC iron balls, alloyed with 1,23 wt% of vanadium

(c) HCC iron balls, alloyed with 2,43 wt% of niobium

(d) HCC iron balls, alloyed with 0,021 wt% of boron

Fig. 1. *Optical micrographs of as-cast grinding balls structure (in the surface and in the center of balls): base alloy and high chromium alloys modified by individual addition of vanadium, niobium and boron*

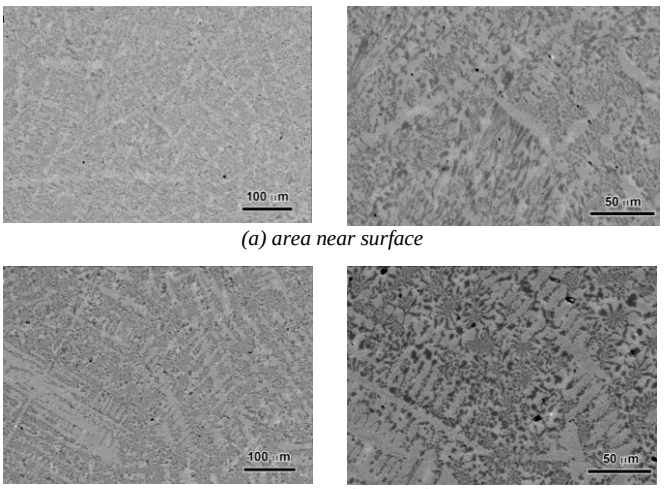

(a) area near surface

(b) area 15 mm from surface

Fig. 2 *SEM micrographs of as-cast grinding balls structure, containing 1,23 wt% of vanadium: (a) near surface and (b)central region5 i 15mm*

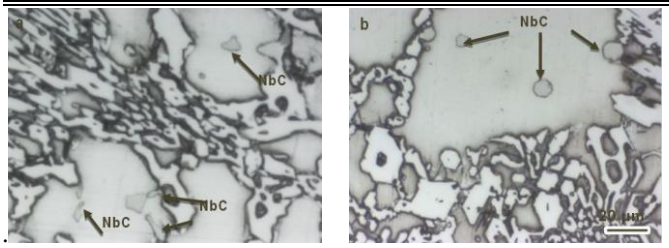

Fig. 3. *Optical micrographs of as-cast grinding balls structure, containing 2,43 wt% of niobium: (a) near surface and (b)central region*

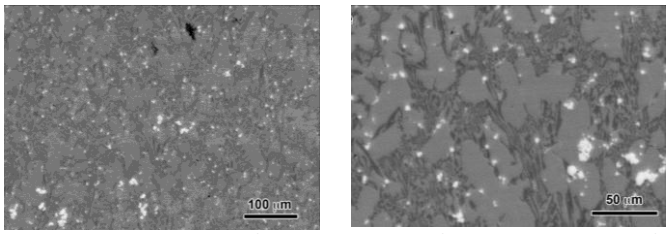

Fig. 4. *SEM micrographs of the microstructure of iron with the addition of 2.43 % Nb at a distance of 5 mm from the surface of the ball.*

Irons alloyed with boron have a significantly finer structure, if compared to the base alloy and iron alloyed with niobium, Fig. 1 (d). The size of micro-constituents is comparable to the size of the those present in the irons alloyed with 1.23 % of vanadium. The size of the particles increases from the surface to the central zone of the balls, with the largest changes in its size being observed in the zone 15 mm from the surface. The morphology of dendrites in boron alloyed irons generally does not change on the observed cross-section from the edge to the center of the balls, in contrast to iron alloyed with vanadium.

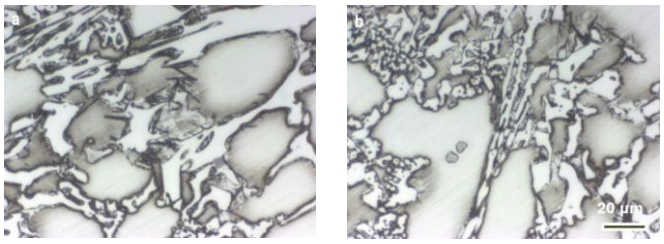

Fig. 5. *Optical micrographs of as-cast grinding balls structure, containing 0,021 wt% of boron: (a) near surface and (b)central region*

Boron affects not only the way of crystallization of high chromium irons, but also the transformation of austenite during cooling after solidification. The degree of transformation of austenite into martensite, both eutectic and primary, is higher than in irons modified with the addition of niobium, and on the other hand, it is somewhat lower compared to irons with the addition of 1.23 wt%V.

Mechanical properties

The results of hardness tests and examination of compressive yield stress are presented in Fig.5. and 6. The hardness of grinding balls was determined by the Rockwell hardness testing method, and the calculated average measured values for the cross-section of the balls are given in Fig.5. All tested alloys have a relatively comparable values of the average hardness in the cross section of cast balls, noting that high chromium iron modified with vanadium

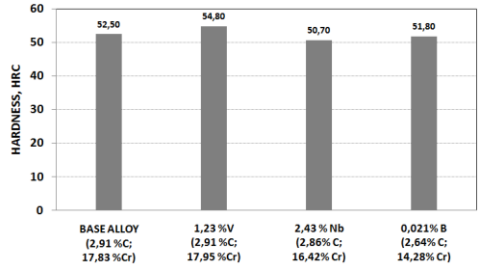

Fig.5. *Rockwell hardness of tested high chromium white iron balls*

has the highest hardness, which is a consequence of the largest volume fraction of eutectic M_7C_3 carbides and a relatively high degree of martensitic transformation in the structure, Fig. 2.

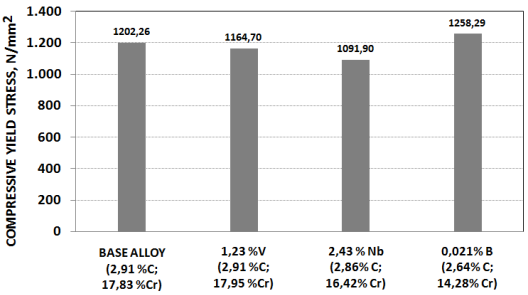

Fig. 6. *Compressive yield stress of tested alloys in as-cast condition*

The highest compression yield stress is measured on samples of high-chromium iron alloyed with the 0,021 wt% of boron, noting that the measurements were made on cylindrical samples taken from the central zone of the casting, Fig. 6.

Corrosion properties

The corrosion properties were evaluated by electrochemical methods, followed by microstructure analysis, in order to detect the relationship between the different alloying elements content and corrosion behavior of grinding balls. Two techniques have been used for testing corrosion properties of cast balls: linear polarization and Tafel extrapolation technique (potentiodynamic polarization). Corrosion parameters of as-cast balls of base alloy and irons containing vanadium, niobium and boron, obtained by linear polarization measurements are illustrated in Fig. 7.

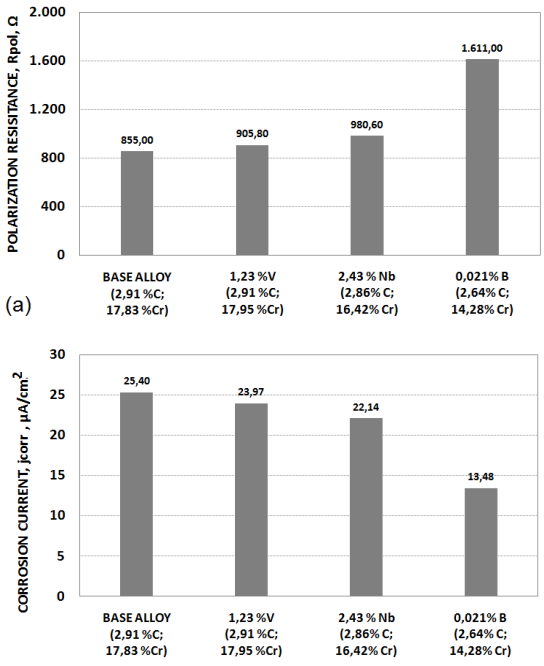

Fig. 7. *Polarization resistance (a) and corrosion current (b) obtained from linear polarization measurements; corrosion ambience fresh water*

From the figures it can be seen that individual addition of all of three used alloying elements cause an increase in polarization resistance and a decrease in corrosion current under the given test conditions. Linear polarization measurements have shown that boron containing high chromium white iron grinding balls have the highest R_{pol} and the lowest j_{corr}, compared to the base alloy and alloys containing the vanadium and niobium.

Tafel curves of high chromium white iron cast grinding balls, containing different alloying elements are given in Fig. 8. The single addition of all of three used alloying elements shifts the Tafel curves of modified high-chromium white irons toward less negative values. Corrosion potentials, $E_{(j=0)}$, of alloyed irons, if compared to

the non-alloyed ones, are less negative in any analyzed case. The value of $E_{(j=0)}$ of boron alloyed iron is less negative by about 80 mV if compared to the base alloy, Fig.8 and Fig, 9.a. Under the potentiodynamic polarization conditions, as well as in linear polarization conditions, the lowest corrosion current density was measured for the boron-modified alloy, Fig. 9.b.

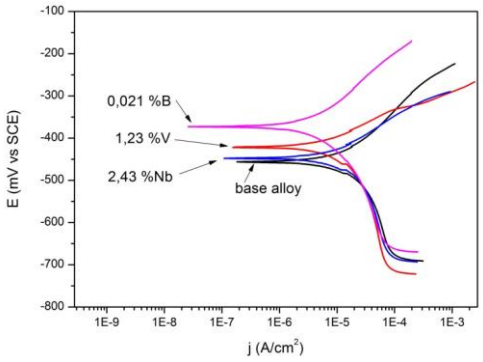

Fig.8. *Tafel curves for high chromium white iron cast grinding balls, containing different alloying elements; corrosion ambience fresh water*

The shift of the Tafel curves towards less negative values of the potential due to alloying with V, Nb and B, is also followed by a decrease in the values of the corrosion current densities, compared to the basic unmodified base alloy; Fig 9.b.

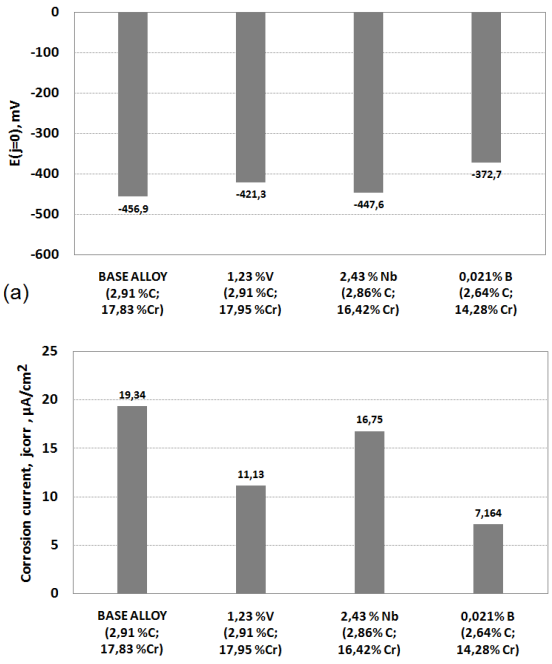

Fig.9. *E(j=0) (a) and j_{corr} (b) obtained from potentiodynamic polarization measurements; corrosion ambience fresh water*

The results of both techniques indicate the less active corrosion of boron modified high chromium white iron grinding balls in tested conditions if compared to base alloy and niobium and vanadium alloyed irons.

3. Conclusion

The alloying elements, vanadium, niobium and boron affect to a greater or lesser extent the size, morphology and volume fraction of both primary austenite dendrites and eutectic colonies in high chromium white irons. The addition of vanadium produces significantly finer microstructure compared to base and niobium alloyed irons. The addition of boron also produces finer microstructure, noting that the size of micro-constituents is comparable to the size of the constituents present in the vanadium alloyed irons. Iron modified with vanadium has the highest hardness, as a consequence of the largest volume fraction of eutectic M_7C_3 carbides and a relatively high degree of martensitic transformation. The highest compression yield stress is measured on samples of boron alloyed iron. Boron containing high chromium white iron have the highest R_{pol} and the lowest j_{corr}, compared to the base and vanadium/niobium containing irons. The single addition of all of three used alloying elements shifts the Tafel curves toward less negative values. The lowest corrosion current densities were measured for the boron-modified alloy. Based on the obtained results it can be concluded that the most favorable combination of mechanical and corrosion properties were obtained for the high chromium white iron modified with 0,021 % of boron.

4. References

1. Eternal Bliss Alloy Casting & Forging Co, Ltd. Technical Dept.: *„Introduction and application of high chromium cast iron materials”*, https://ebcastworld.com/high-chromium-cast-iron/ December 20, 2019
2. High Alloy White Irons, *Total Materia*, ref.13 December 20, 2002
3. The hardness of grinding media ball, https://www.nghexin.com/the-hardness-of-grinding-media-ball/
4. A. Bedolla-Jacuinde: Microstructure of vanadium-, niobium- and titanium-alloyed high-chromium white cast iron. *Int. J. Cast Metals* Res. 13(6) 343-361. (2001)
5. P. Dupin, J.M. Schissler, Influence of Addition of Silicon, Molybdenum, Vanadium, and Tungsten Upon the Structural Evolution of the As-Cast State of a High-Chromium Cast Iron, *AFS Trans.*, 92 355-360(1984)
6. A. Sawamoto, K. Ōgi, K. Matsuda: Solidification structures of Fe-C-Cr-(V-Nb-W) alloys, *AFS Trans.* 94 403-416. (1986)
7. R. Kesri, M. Durand-Charre: Phase equilibria, solidification and solid-state transformations of white cast irons containing niobium, *J. Mater. Sci*. 22(8) 2959-2964. (1987)
8. H.K. Baik, C.R. Loper: The influence of niobium on the solidification structure of Fe-C-Cr alloys, *AFS Trans*. 96 405-412. (1988)
9. A. Sawamoto, K. Ogi and K. Matsuda, Solidification Structures of Fe-C-Cr-Nb Alloys, *J.Japan Inst. Met*., 49) 6, 475-482 (1985)
10. Shen,J.; Zhou,Q.D. Solidification behaviour of boron-bearing high-chromium cast iron and the modification mechanism of silicon, *CastMet.*1988, 1, 79–85.
11. H. Fusheng, W. Chaochang, Modifying high Cr–Mn cast iron with boron and rare earth–Si alloy, *Materials Science and Technology*, 5 918-924(1989)
12. Correa, R.; Bedolla-Jacuinde, A.;Zuno-Silva, J.; Cardoso, E.;Mejía, I. Effect of boron on the sliding wear of directionally solidified high-chromiumwhiteirons.Wear,267(1-4),495–504.(2009)
13. M. Fiset, K. Peev, M. Radulovic (Filipović): The influence of niobium on fracture toughness and abrasion resistance in high chromium white cast irons, *J. Mater. Sci. Lett*. 12 (9) 615-617. (1993)
14. M. Radulović (Filipović), M. Fiset, K. Peev, M. Tomović, The influence of vanadium on fracture toughness and abrasion resistance in high chromium white cast irons, *J. Mater. Sci*. 29 (19),, 5085-5094 (1994)
15. C.P. Tabrett, I.R. Sare, M.R. Ghomashchi: Microstructure-property relationships in high chromium white iron alloys, *Int. Mater. Rev*. 41, 59–82. (1996)
16. Bedolla-Jacuinde, R. Correa, I. Mejia, J.G. Quezada, W.M. Rainforth: The effect of titanium on the wear behaviour of a 16% Cr white cast iron under pure sliding. *Wear*, 263 (1), 808-820. (2007)
17. H. Berns: Comparison of wear resistant MMC and white cast iron, Wear 254(1-2) 47–54. (2003)
18. Filipovic, M.; Kamberovic,Z.; Korac,M.;Gavrilovski,M. Correlation of microstructure with the wear resistance and fracture toughness of the white cast iron alloys.*Met.Mater.Int.*, 19 (3), 473-481. (2013)
19. A. Sawamoto, K. Ōgi, K. Matsuda: Solidification structures of Fe-C-Cr-(V-Nb-W) alloys, *AFS Trans.* 94 403-416. (1986)
20. Q.D. Zhou and Q.C. Rao, 55-th International Foundry Congress, Moscow, , Paper N^{0}15. (1988)
21. B. Lu et al, Corrosion and Wear Resistance of Chrome White Irons – A Correlation to Their Composition and Microstructure, *Metall Mater Trans* A 37A:3029-3038 (2006)
22. L.E. Svensson et al, *J Mater Sci* 21: 1015-19 (1986)
23. Kh. Abd El-Aziz et al, Wear and Corrosion Behavior of High-Cr White Cast Iron Alloys in Different Corrosive Media, *J Bio Tribo Corros* 1:25(2015)

Acknowledgement: This work has been supported by Ministry of Education, Science and Technological Development of the Republic of Serbia, and Ministry of Economic Development of Montenegro, under contract No. E!13302CastBalls: White iron composition and processing design for highly efficient casted milling balls.

Recent developments and regulations in fire resistance of wood and wood-based composites

Nadir Ayrilmis
Department of Wood Mechanics and Technology, Forestry Faculty, Istanbul University-Cerrahpasa, Bahcekoy, Sariyer, 34473, Istanbul, Turkey
nadiray@istanbul.edu.tr

Abstract: This study focused on the fire-retardant treatment of wood and wood-based composites using various methods. The recent developments in the fire-retardant standards and classification of wood and wood-based composites were reviewed. Most commonly used fire-retardants and commercial application methods of fire retardants such as boron compounds and phosphates to improve fire resistance of wood and wood based composites were explained. Furthermore, fire-retardant mechanism was informed. Novel nanomaterials used in the fire resistance of wood and wood-based composites were introduced. Significant criteria in choosing of the suitable fire retardants for wood and wood-based composites were explained.
KEYWORDS: *FIRE, FLAME RETARDANCY, WOOD, FIRE RETARDANTS, COMBUSTION, WOOD-BASED COMPOSI T*

1. Introduction

Fire resistance is one of the main obstacles to use wood and wood-based composites in structural applications in most countries. In figures, fires in dwellings cause in Europe over 4.000 deaths and 80.000 diverse injuries per year. The cause of death is suffocation due to smoke in about two thirds of the cases, while burns result only in about one third of the fatalities [1].

Fire retardants protect wood against to the fire in different ways [2]:

Promotion of char formation,

- Conversion of volatile gases to inert gases such as water vapour and carbon dioxide,
- Dilution of pyrolysis gases,
- Inhibiting chain reactions of burning in the gas phase,
- Protecting the surface by an insulating/intumescent layer.

Significant criteria in choosing of the suitable fire retardants are as follows:

Low-toxicity to human health
Minimal risk to atmosphere, climate and environment
Flame spread of 25 or less or «Class B»
Self extinguishing
Won't spread fire
Reduced heat release rate
Disrupts volatile gases
Suitable with manufacturing process conditions (resin blending and hot pressing) during production of wood based-composites
Minimum effect on mechanical properties of wood and wood based materials
Easy-suppy
Low-cost
Easy preparation and application to wood and wood-based panels
Type of wood based substrate
Regulatory requirement to be satisfied
New build or maintenance/upgrade
Service life conditions/environment
Installation conditions
Maintenance requirements

2. Fire-retardant treatment methods of wood and wood-based composites

Fire retardants, if correctly applied, provide added value to wood materials extend the market potential of the world's most natural building material.

Commercial applications of fire retardants to wood can be divided to three classes:

1) Impregnation of wood with a fire retardant using vacuum and over pressure.
2) Addition of a fire retardant as a surface application.
3) Addition of a fire retardant to wood during its manufacturing process (in particular adhesive with fire retardant). Compatibility between resin and fire retardant (in terms of acidity of the fire retardant) and hot pressing conditions is significant factor.

Other techniques to improve fire resistance of wood and wood based composites are as follows:

a) Chemical modification

The most common fire retarding chemicals used for wood and wood-based panels are inorganic salts, such as ammonium polyphosphate, monoammonium phosphate, diammonium phosphate, ammonium sulfate, melamine phosphate, guanyl phosphate, ammonium sulphate; aluminum trihydrate (the most widely used fire retardant in the U.S.), magnesium hydroxide, and boron compounds, such as borax, boric acid, borax pentahydrate, disodium octaborate tetrahydrate, ammonium pentaborate, zinc-borate, and zinc chloride [3,4]. Waterborne inorganic salts may be hygroscopic and cause to the corrosion metal fixtures in treated wood.

Chemical mechanisms are often accompanied by one or several physical mechanisms, most commonly endothermic dissociation or dilution of fuel. Charring is the most common condensed phase mechanism (Fig. 1).

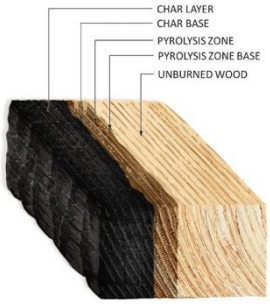

Figure 1. *Superficial carbonization structure of wood exposed to the fire [5].*

b) Physical modification

The physical modifications can include, for instance, combinations of different wood species, methods for higher surface densities, and composites [2]. If the top layer of a wood material consists of a specific species of wood with a relatively low heat release, the heat release peak is smaller, offering possibilities to improve the reaction-to-fire class of the wood material. Alternatively, fire-retardant treated lamellas can be included in wood as surface layers. Using this method, the consumption of fire retardant is reduced compared to wood materials that are fire-retardant treated as a whole. Ignition can be delayed by introducing a high-density surface layer on a wood material. High pressure laminate, for example, might be used for this purpose [2].

c) Nanocomposites

Fire performance of wood and wood-based composites can be improved by using nanocomposites made of layered silicates and

organic polymers. The mechanism of fire retardancy of nanocomposites is generally considered to be due to the structure of the char formed during combustion, which enables the char to thermally insulate the polymer and inhibit the formation and escape of volatiles. Nanoscale fire retardants, such as SiO_2, TiO_2 and ZrO_2, nanoclay, nano-wollastonite, carbon nanotube, nano-silica, have a high ratio of surface area to weight; the smaller the particle size is, the bigger the ratio of surface area to weight. These adavantages improve fire resistance of nanoscale fire retardant chemicals. In addition, nanoscale fire retardants, for example zinc borate, can adsorb more smoke and dust per unit weight than regular sizes during wood combustion.

The most commonly used test methods and guidance documents for the reaction to fire testing of wood materials are as follows:

1. Non-combustibility test EN ISO 1182
2. Gross calorific potential test EN ISO 1716
3. Single Burning Item test EN 13823
4. Ignitability test EN ISO 11925-2
5. Radiant panel test EN ISO 9239-1

3. Fire protection classes of wood materials

Fire protection classes of the materials according to EN 13501-2 and DIN 4102 is given in Table 1. According to Table 1, for example, F90 means that escape routes beneath the fire are protected for up to 90 minutes.

Table 1. *Fire protection classes of the materials.*

Test designation type	Fire protection class		Fire protection in min.
	EN 13501-2	DIN 4102	
fire retarding	REI 30	F 30	30
highly retardent	REI 60	F 60	60
fire resisting	REI 90	F 90	90
fire resisting	REI 120	F 120	120
high fire resistance	REI 180	F 180	180

The relevant classification system is based on the EN 13501-1. In the Euroclass system, building materials are divided to seven classes on the basis of their reaction-to-fire properties. The performance description and the fire scenario for each class are presented in Table 2 according to the main principles used in the development of the Euroclass system [2].

Table 2. Indicative performance descriptions and fire scenarios for Euro-classes.

Class	Performance description	Fire scenario and heat attack		Examples of products
A1	No contribution to fire	Fully developed fire in a room	At least 60 kW/m^2	Products of natural stone, concrete, bricks, ceramic, glass, steel and many metallic products
A2	"	"	"	Products similar to those of class A1, including small amounts of organic compounds
B	Very limited contribution to fire	Single burning item in a room	40 kW/m^2 on a limited area	Gypsum boards with different (thin) surface linings Fire retardant wood products
C	Limited contribution to fire	"	"	Phenolic foam, gypsum boards with different surface linings (thicker than in class B)
D	Acceptable contribution to fire	"	"	Wood products with thickness ≥ about 10 mm and density ≥ about 400 kg/m^3 (depending on end use)
E	"	Small flame attack	Flame height of 20 mm	Low density fibreboard, plastic based insulation products
F	No performance requirements	–	–	Products not tested (no requirements)

The highest possible European class for fire retardant wood materials is class B. Untreated wood usually fulfils class D. The main parameters influencing the reaction to fire characteristics of all wood are product thickness, density and end use conditions such as substrates or air gaps behind the wood material [6].

Table 3. *Classification of wood and wood-based composites according to EN 13986 standard.*

Wood-based panel products[2)]	EN product grade reference	Minimum density (kg/m^3)	Minimum thickness (mm)	Class[3)] (excluding floorings)	Class[4)] Floorings
Particleboards	EN 312	600	9	D-s2, d0	D_{FL}-s1
Fibreboards, Hard	EN 622-2	900	6	D-s2, d0	D_{FL}-s1
Fibreboards,	EN 622-3	600	9	D-s2, d0	D_{FL}-s1
Medium		400	9	E, pass	E_{FL}
Fibreboards, Soft	EN 622-4	250	9	E, pass	E_{FL}
Fibreboards, MDF[5)]	EN 622-5	600	9	D-s2, d0	D_{FL}-s1
Cement-bonded particleboard[6)]	EN 634-2	1000	10	B-s1, d0	B_{FL}-s1
OSB board[7)]	EN 300	600	9	D-s2, d2	D_{FL}-s1
Plywood	EN 636	400	9	D-s2, d0	D_{FL}-s1
Solid wood panels	EN 13353	400	12	D-s2, d0	D_{FL}-s1

1) EN 13986
2) Wood-based panels mounted without an air gap directly against class A1 or A2-s1,d0 products with minimum density 10 kg/m^3 or at least class D-s2,d0 products with minimum density 400 kg/m^3
3) Class as provided for in Table 1 of the Annex to Commission Decision 2000/147/EC
4) Class as provided for in Table 2 of the Annex to Commission Decision 2000/147/EC
5) Dry process fibreboard
6) Cement content at least 75% by mass
7) Oriented strand board

Structural timber with minimum mean density of 350 kg/m^3 and minimum thickness and width of 22 mm may, based on the evidence presented, be classified without further testing as class D-s2, d0. Glued laminated timber (Glulam) with minimum mean density of 380 kg/m^3 and minimum thickness and width of 40 mm can be classified without further testing as class D-s2, d0 [6]. Classes of reaction to fire performance for construction materials excluding floorings are given in Table 4 [2]. The significant parameters affecting the reaction to fire behavior of wood material are its density and thickness, and final use conditions such as substrates or air gaps behind the wood material. For wood materials except floorings the relevant main classes are B, C, D, and E. The relevant additional classes for smoke development are s1, s2 and s3, and for burning droplets d0, d1 and d2 (Table 4).

Table 4. *Euroclass of reaction to fire performance for construction materials excluding floorings [2].*

Class	Test method(s)	Classification criteria	Additional classification
A1	EN ISO 1182 (1); *and*	$\Delta T \le 30°C$; *and* $\Delta m \le 50\%$; *and* $t_f = 0$ (i.e. no sustained flaming)	-
	EN ISO 1716	PCS ≤ 2.0 MJ.kg^{-1} (1); *and* PCS ≤ 2.0 MJ.kg^{-1} (2) (2a); *and* PCS ≤ 1.4 MJ.m^{-2} (3); *and* PCS ≤ 2.0 MJ.kg^{-1} (4)	
A2	EN ISO 1182 (1); *or*	$\Delta T \le 50°C$; *and* $\Delta m \le 50\%$; *and* $t_f \le 20s$	
	EN ISO 1716; *and*	PCS ≤ 3.0 MJ.kg^{-1} (1); *and* PCS ≤ 4.0 MJ.m^{-2} (2); *and* PCS ≤ 4.0 MJ.m^{-2} (3); *and* PCS ≤ 3.0 MJ.kg^{-1} (4)	
	EN 13823 (SBI)	FIGRA ≤ 120 W.s^{-1}; *and* LFS < edge of specimen; *and* $THR_{600s} \le 7.5$ MJ	Smoke production(5); *and* Flaming droplets/ particles (6)
B	EN 13823 (SBI); *and*	FIGRA ≤ 120 W.s^{-1}; *and* LFS < edge of specimen; *and* $THR_{600s} \le 7.5$ MJ	Smoke production(5); *and* Flaming droplets/ particles (6)
	EN ISO 11925-2(8): *Exposure = 30s*	Fs ≤ 150mm within 60s	
C	EN 13823 (SBI); *and*	FIGRA ≤ 250 W.s^{-1}; *and* LFS < edge of specimen; *and* $THR_{600s} \le 15$ MJ	Smoke production(5); *and* Flaming droplets/ particles (6)
	EN ISO 11925-2(8): *Exposure = 30s*	Fs ≤ 150mm within 60s	
D	EN 13823 (SBI); *and*	FIGRA ≤ 750 W.s^{-1}	Smoke production(5); *and* Flaming droplets/ particles (6)
	EN ISO 11925-2(8): *Exposure = 30s*	Fs ≤ 150mm within 60s	
E	EN ISO 11925-2(8): *Exposure = 15s*	Fs ≤ 150mm within 20s	Flaming droplets/ particles (7)
F	No performance determined		

(1) For homogeneous products and substantial components of non-homogeneous products.
(2) For any external non-substantial component of non-homogeneous products.
(2a) Alternatively, any external non-substantial component having a PCS ≤ 2.0 MJ/m^2, provided that the product satisfies the following criteria of EN xxxx(SBI) : FIGRA ≤ 20 W.s^{-1}; *and* LFS < edge of specimen; *and* $THR_{600s} \le 4.0$ MJ; *and* s1; *and* d0.
(3) For any internal non-substantial component of non-homogeneous products.
(4) For the product as a whole.
(5) **s1** = SMOGRA ≤ 30m^2.s^{-2} *and* $TSP_{600s} \le 50$m^2 ; **s2** = SMOGRA ≤ 180m^2.s^{-2} *and* $TSP_{600s} \le 200$m^2; **s3** = not s1 or s2.
(6) **d0** = No flaming droplets/ particles in ENxxxx (SBI) within 600s; **d1** = No flaming droplets/ particles persisting longer than 10s in ENxxxx (SBI) within 600s; **d2** = not d0 or d1; Ignition of the paper in EN ISO 11925-2 results in a d2 classification.
(7) Pass = no ignition of the paper (no classification); Fail = ignition of the paper (**d2** classification).
(8) Under conditions of surface flame attack and, if appropriate to the end–use application of the product, edge flame attack.

4. Conclusions

When the wood is heated, it burns by producing flammable volatiles that can ignite. To reduce combustion, wood is treated with fire retardants which significantly decrease the rate at which flames travel across the wood surface. Nevertheless, some fire-retardant treatments may produce unwanted secondary side effects, for example, increased moisture content, reduced strength and increased potential to corrode metal connectors. To decrease these negative effects, fire retardant treatments may improve the fire performance of wood and wood-based composites considerably through reducing ignitability, rate of heat release and flame spread. This study summarized the fire-retardant treatment mechanism, national and international fire testing standards, and commonly used fire retardants in wood industry. When the wood is protected against to the fire using fire-retardants, its use will increase in construction industry, especially for structural timbers as well as home furniture, doors, window frames, and other applications.

5. References

[1] Anonymous. European Project. FP7-SME-2012-1-315425. Flame-retardant coatings based on nano-magnesium hydroxide, huntite and hydromagnesite for wood applications, wood-Flaretcoat, 2015.

[2] Anonymous. Innovative eco-efficient high fire performance wood products for demanding applications. Material related to the Project. 2015 [http://virtual.vtt.fi/virtual/innofirewood/].

[3] Anonymous. Flame retardants under fire. 2015 [https://www2.buildinggreen.com/article/flame-retardants-under-fire].

[4] Ayrilmis, N., Kartal, S.N., Laufenberg, T., Winandy, J.E., White, R.H. Physical and mechanical properties and fire, decay, and termite resistance of treated oriented strandboard. Forest Products Journal 2015;55(5):74-81.

[5] Le, T.D.H., Tsai, M.T. Experimental assessment of the fire resistance mechanisms of timber-steel composites. Materials 2019;12:4003.

[6] Ostman, B.A.L., Mikkola, E. European classes for the reaction to fire performance of wood products. Holz als Roh- und Werkstoff 2006;64:327-337.

New regulations on the formaldehyde emission from wood-based panels

Nadir Ayrilmis
[1]Department of Wood Mechanics and Technology, Forestry Faculty, Istanbul University-Cerrahpasa, Bahcekoy, Sariyer, 34473, Istanbul, Turkey
nadiray@istanbul.edu.tr

Abstract: Formaldehyde is considered a health hazard, hence the wood-based panels must be within the limits imposed by the strictest regulations regarding the formaldehyde release. New national and international international regulations of formaldehyde emission from wood-based panels widely used in furniture industry were investigated in this study. The results of the study can be useful for the wood-based panel factories to follow the standards and regulations in terms of formaldehyde emission.
KEYWORDS: *FORMALDEHYDE EMISSION, WOOD-BASED PANEL, ADHESIVE, FURNITURE, PARTICLEBOARD, MDF*

1. Introduction

Wood-based panel and furniture industries have already reduced formaldehyde emission of raw panels by more than 80% over the past twenty years to minimize indoor air contaminants [1]. Wood based panels such as medium-density fiberboard, particleboard (MDF) and particleboard are increasingly being specified for residential and office furniture applications, especially the use of particleboard in inexpensive bookshelves and similar items. MDF uses more adhesive than particleboard, which causes higher initial formaldehyde emission of MDF than particleboard. Li [2] determined the amount of volatile organic compound (VOC) emission and its composition of six kinds of commercial wood-based panels in a period of time for 28 days. It was found that the formaldehyde emission level from high to low was high-density fiberboard (HDF), MDF, plywood, veneer-faced MDF, and oriented strand board (OSB).

Most of the adhesives currently used in the particleboard industry are formaldehyde-based adhesives (UF, MUF), which have a molar ratio of formaldehyde to urea (F:U) between 1.00 and 1.10. The majority of thermosetting resins used in the wood-based panel industry are based on the formaldehyde-based resins. Among them, the UF resin is the most used resin. Due to its significant advantages such as cheaper, colorless, easy-supply, shorter hot pressing time and temperature than others, good mechanical properties of particleboard in dry conditions. The disadvantages of the UF resin are higher formaldehyde emission from other resins and lower water and moisture resistance. Off-gassing of formaldehyde from wood-based panels can be one of the main contributors to the elevated formaldehyde levels and exposure in the homes. Sensitive people against to the formaldehyde start to experience irritation at 0.6mg/m^3 and most of us will be irritated at 1.2 mg/m^3. This range of 0.6 to 1.2 mg/m^3 is the official IARC (International Agency for Research on Cancer) threshold
for eye, nose and throat irritation [3]. A correlation was determined between the formaldehyde emission of the resin and the formaldehyde emission factor of the wood-based panel. That is, the higher the content of formaldehyde in the adhesive, the higher the level of formaldehyde emission from wood-based panel, and there is a good linear relationship between them [4].

Urea-formaldehyde is classified according to its formaldehyde emission from the wood-based panels (from the lowest to highest level):

1. Super E0
2. E0
3. E1
4. E2
5. E3

For indoor and furniture applications, a lower formaldehyde content is required, if classified under the E1 emission class. Formaldehyde emission classes in finished panels, defined in Annex B of EN 13986:2014+A1:2015 standard are as follows:

- Class E1: ≤ 8mg/100g dry board according to EN 120 or < 0.124 mg/m^3 according to EN 717-1;
- Class E2: > 8 to < 30mg/100g dry board according to EN 120 or > 0.124– < 0.3 mg/m^3 according to EN 717-1.

Formaldehyde emission values (perforator value) of various materials (MDF, particleboard, blockboard, laminate flooring, and parquet) characterized by the perforator extraction method of the Chinese national standard GB 18580 is given in Figure 1.

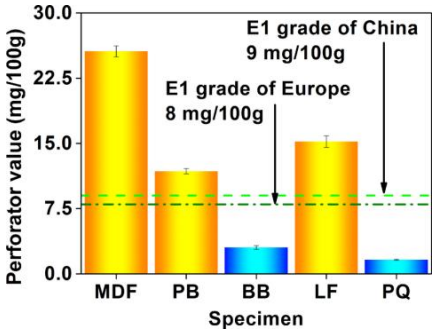

Figure 1. *Formaldehyde emission values (perforator value) of various [5].*

According to the International Composite Board Emission Standards (ICBES), there are three European formaldehyde classes, which are E0, E1 and E2, respectively. This classification is based on the measurement of formaldehyde emission levels from the wood-based panels. For example, E0 is classified as having less than 3 milligrams of formaldehyde out of every 100 grams of the glue used in particleboard and plywood fabrication. E1 and E2, conversely, are classified as having 9 and 30 milligrams of formaldehyde per 100 grams of the panel, respectively. All around the world variable certification and labeling schemes are there for such products that can be explicit to formaldehyde release, like that of Californian Air Resources Board (CARB). In addition, the production of wood-based panels is increasingly influenced by product emission quality standards applied outside Europe, most importantly CARB standards, originating from Californian legislation. The emission limit values in the wood-based panels used in furniture applications are at levels much lower than the corresponding lowest emitting standard in the EN standards. Formaldehyde emission classes defined by ATCM (Airborne Toxic Control Measure) 93120:

- CARB phase 2 standard for MDF: 0.11 ppm;
- CARB phase 2 standard for particleboard: 0.09 ppm.

2. Formaldehyde emission methods and regulations

There are different standardized methods used in the determination of formaldehyde emission from the wood-based panels such as chamber, gas analysis, perforator, desiccator, and flask. These methods can be classified as “measurable emission” (really emitted amount of formaldehyde under the test conditions) and the “emittable potential” of formaldehyde in the panel (maximum emittable formaldehyde under conditioning at forceful conditions) [6]. Each method measures the formaldehyde released

from wood panels (covered and uncovered) and frequently produces results in different and non-interchangeable units. Standard methods and differences between general conditions used for formaldehyde determination from the wood-based panels are presented in Table 1.

Table 1. *Standard methods and differences between general conditions used for formaldehyde determination.*

Test method/ Standard	Equipment characteristics	Sample dimensions/total surface area	Test conditions	Sample conditioning	E1 class limit
Chamber/ EN 717-1	0.25, 1, 40 (12-52)m³	Loading ratio: 1m²/m³ Edge sealing	Temperature: 23±0.5°C RH: 45±3% Air velocity: 0.1-0.3m/s Time:1-4weeks	No (0,225L) T-20 °C, RH-65%	≤0.124mg /m³, or 0.1ppm
Gas analysis/ EN 717-2	4L cylindrical chamber	400x50mm Edge sealing	Temperature: 60± 0.5°C RH:≤3% Air velocity: 1L/min Time: 4hours	Varied T-20 °C, RH-65%	≤3.5mg/ m²h
Perforator/ EN 120	Extractor apparatus	25x25mm (110g) No edge sealing	Extraction with 600ml toluene at 110°C Time: 3h	T-23°C RH- 45%	≤ 8 mg /100 g o.d. board
Flask/ EN 717-3	500 ml flask	25x25mm (20g) No edge sealing	Temperature: (40 ±1) °C Time: 3 hours	No	No official limit are stated
Desiccator / JIS A1460	40L – 240 mm nominal dimension; 120mm outside diameter crystallizing dish/ 60-65mm depth	150x50mm±1mm/ close to 1800 cm² No edge sealing	Temperature: 20°C±0.5°C Time:24h±5min.	7-10 days 65%RH/20°C	F**~E1- ≤1.5mg/L F**** ≤0.3mg/L (SE0)

The formaldehyde emission shows a big challenge for wood-based panel industry because of new regulations concerning the limits of formaldehyde release. Emission databases reveal the interest of consumers for low emitting products in the future. These will lead to an increased requirement for the testing of products to determine the level of formaldehyde emission. To measure the levels of FE, many different methods have been used and the most reliable is the chamber method.

A new class (SE0 and EO) of low formaldehyde emitting panels was established by Japanese standards and European Panel Federation (EPF) launch its own formaldehyde standards that corresponds to a perforator value below 4 mg/100 g oven dry board for particleboard 5 mg/100 g oven dry board for MDF, which is half of the actually limit stated in the EN standard. These new trends force the wood panels' manufacturers and the glue producers to look for alternatives for formaldehyde free wood panels.

Fig. 2. *Typical formaldehyde chamber based on EN 717-1 standard (Guangdong grande automatic test equipment limited, China).*

Formaldehyde scavengers, often called formaldehyde catchers, are chemical compounds added to the glue mix in order to decrease the formaldehyde emission from the finished wood panels. They are widely used today in the European particleboard and MDF industry. Mostly, aqueous solutions of urea (40% or 45% solids content) are applied. Furthermore, some scavengers such as sodium metabisulfite ($Na_2S_2O_5$), ammonium bisulfite ($(NH_4)HSO_3$), or ammonium phosphates, are also applicable in the European panel industry [7]. Formaldehyde scavengers are also added directly on the wood chips ahead of gluing. In some particleboard manufacturers, urea is added as a solid material ahead of blending to keep moisture content of chips as low as possible. They are used up to a maximum 10-15% on the liquid resin, achieving thus reduction in the formaldehyde emission up to 50% [8]. Experience in Europe has shown that instead of using a very low F:U ratio adhesive, a plant can achieve better results by using a system of an equivalent F:U ratio, which is a combination of a higher F:U ratio UF, and a formaldehyde scavenger. Further developments to address these problems included the addition of a small quantity of melamine (usually 1–4%). Although the addition of melamine increases the production cost, it results in quite successful. Another approach to overcome the negative side effects of the low-emission UF adhesives is the addition of small amounts of PMDI (polymeric diphenylmethane diisocyanate) in the UF binder, in the core layer of particleboards [9].

Table 2. *Standards for determining formaldehyde emission from wood-based panels in China, USA, Europe, and Japan.*

Standard	Limit value	Grade	Testing method	Application scope
EN13986:2005	≤3.5 mg/(m²·h) ≤8 mg/(m²·h)	E_1 E_2	Gas analysis	Plywood
	≤8 mg/100 g ≤30 mg/100 g	E_1 E_2	Perforation	MDF PB
Formaldehyde Emission Standards for Composite Wood Act (S.1660, H.R.4805)	≤0.05 ppm ≤0.09 ppm ≤0.11 ppm ≤0.13 ppm		Chamber	Plywood PB MDF ≤8 mm MDF
JIS A 1460-2001	≤0.3/0.4 mg/L ≤0.5/0.7 mg/L ≤1.5/2.1 mg/L	F☆☆☆☆ F☆☆☆ F☆☆	Desiccator	Plywood MDF PB
GB/T9846.3-2004	≤0.5 mg/L	E_0	Desiccator	Plywood
GB18580-2001	≤1.5 mg/L ≤5.0 mg/L	E_1 E_2	Desiccator	Plywood
	≤9 mg/100 g ≤30 mg/100 g	E_1 E_2	Perforation	MDF PB

Some regulations in Europe is given in Table 3. As the French labeling system Decree 2011-321 used as construction material. volatile organic compound of many materials used keeps its emissions at a certain standard.

Table 3. *VOC regulations used in Europe*

EU	Construction Product Regulation (CPR)	CEN/TS 16516:2013 ISO 16000-9
FR	Decree 2011-321 French labelling	ISO 16000-9 ISO 16000-3, 6
DE	Health-related Evaluation of Emissions of Volatile Organic Compounds (VVOC, VOC and SVOC) from Building Products	AgBB ISO 16000-9
BE	Royal Decree establishing the threshold levels of emissions to the indoor building products for specific intended use	CEN/TS 16516:2013 ISO 16000-9

3. *Formaldehyde scavengers*

Main parameters affecting formaldehyde emission from wood-based panels produced using UF resin are as follows:

1. Tree species and wood acidity
2. F/U molar ratio of UF resin
3. The amount of resin used
4. Density and thickness of of fiberboard
5. Hardener type and content
6. Free-formaldehyde content in the UF resin
7. Moisture content of mat
8. Moisture content of finished panel
9. Hot pressing parameters (temperature, time, and pressure)
10. Environmental conditions (humidity and temperature) for finished of fiberboard
11. Overlaying of fiberboard

Formaldehyde scavengers, capable of capturing formaldehyde either physically or chemically and forming stable products, are added to UF resins or to wood particles before pressing. These additives should provide long-term FE reduction, in principle along the panel's service life. Examples used in industry include addition of urea in aqueous solution or powder form, organic amines, scavenger resins such as UF resins with F/U well below 1.0), sulfites, and functionalized paraffin waxes In the last decades, F/U values in resins for WBP production have decreased from about 1.6 to a range between 0.9 and 1.1. In addition to the F/U ratio, the synthesis process has a relevant role in the final resin properties, including formaldehyde emissions. One strategy to counteract the negative effects of decreasing F/U ratio is resin modification with co-monomers, like melamine or phenol [10].

Industrial use of wood adhesives obtainable from natural resources (also called bioadhesives or bioresins) has been researched since 1970's, but industrial implementation is still restricted due to the production costs, limited availability and consistency of raw materials, and land use issues. Some significant advantages of bio-based adhesives are lower toxicity, renewability, sustainability, and biodegradability, biodegradability. Three materials, tannins, lignins, and vegetable proteins, have found commercial success in the industrial applications.

4. Conclusions

The legal regulations on the formaldehyde emission from wood-based panels will help to increase awareness for the consumers and panel manufacturers. Although the legal regulations can be different in different regions on the world, recently most of them have been updated. Especially, furniture industry is strictly affected by the formaldehyde emission issue due to panel-type furniture has been widely used in the market. It is important for customers to know the meaning of the formaldehyde emission class label from panel type furniture.

5. References

[1] Barry A., Corneau, D. Effectiveness of barriers to minimize VOC emissions including formaldehyde. Forest Products Journal, 20006;56(9):38.

[2] Li, S. Design of Small Environment Chamber and Study of VOC Emission Characteristic from Wood-based Panel, Northeast Forestry University, Harbin,China, 2013.

[3] Golden, R. Identifying an indoor air exposure limit for formaldehyde considering both irritation and cancer hazards. Crit Rev Toxicol. 2011;41(8):672-721.

[4] Zhang, J., Song, F., Tao, J., et al. Research Progress on Formaldehyde Emission of Wood-Based Panel", International Journal of Polymer Science, vol. 2018, Article ID 9349721, 8 pages, 2018.

[5] Song, W., Cao, Y., Wang, D., Hou, G., Shen, Z., et al. An Investigation on Formaldehyde Emission Characteristics of Wood Building Materials in Chinese Standard Tests: Product Emission Levels, Measurement Uncertainties, and Data Correlations between Various Tests. Plos One 10(12): e0144374, 2015.

[6] Costa, N.J.A. Adhesive systems for low formaldehyde emission wood-based panels, University of Porto, 2013.

[7] Carvalho, L., Magalhães, F., João, F. Formaldehyde Emissions from Wood-Based Panels -Testing Methods and Industrial Perspectives, 2012.

[8] Alexandropoulos, P.N., Mantanis, G.I. A European Approach to Particleboard and MDF adhesives. Conference: Composite Panel Association (CPA) - Resin and Blending Seminar, December 1998, Charlotte, North Carolina, USA.

[9] Mantanis, G.I., Athanassiadou, E.T., Barbu, M.C., Wijnendaele, K. Adhesive systems used in the European particleboard, MDF and OSB industries. Wood Mater. Sci. Eng. 2018;13:104-116.

[10] Carvalho, L.M.H. Estudo da Operação de Prensagem do Aglomerado de Fibras de Média Densidade (MDF): Prensa Descontínua de Pratos Quentes University of Porto, Ph.D. Thesis, 1999.

Further development of the possibility of creating composite coatings from ash microspheres on a steel basis

Julia Kazymyrenko[1*], Natalia Lebedeva[1], Tetiana Makrukha[1], Olha Syzonenko[2]
Admiral Makarov National University of Shipbuilding, Heroes of Ukraine ave., 9, 54025, Mykolaiv, Ukraine[1]
Institute of Pulse Processes and Technologies of NAS of Ukraine, Bohoyavlenskyi ave., 43-A, 54018, Mykolaiv, Ukraine [2]
u.a.kazimirenko@gmail.com

Abstract: *The article is devoted to the solution of an important scientific and technical problem of development of new composite coatings with the use of industrial waste of thermal power plants – aluminosilicate empty microspheres. The analysis of existing technologies showed the prospects for the use of electric arc spraying, which will expand the scope of compositions. All-drawn wires of* ER346 (Св-08) *and* 1066 (65Г) *brands were used for coating, ash fillers of aluminosilicate composition were used as fillers. The effectiveness of ash microspheres for the formation of coatings is confirmed by the results of hardness measurements. Coatings filled with ash microspheres have increased Vickers hardness by 7… 22%. The use of ash slags in new technologies is a promising practical area, the implementation of which will help in the search for scarce minerals.*

Keywords*: ASH MICROSPHERES, SPRAYED COATINGS, ELECTRIC-ARC SPRAYING, THERMAL POWER PLANTS.*

1. Introduction

The efficient operation of Ukrainian thermal power plants is accompanied by the release of large amounts of fuel waste, the mineral components of which are converted into ash slag. Ash slag accumulates in ash dumps, which has a negative impact on the environment. Therefore, the issue of fuel waste disposal is very acute. As a result of combustion of coal particles at temperatures of 1600… 1800 ° C complex silicates are formed, which in the process of melting under the action of dissolved gases are transformed into spherical droplets (microspheres) with a gaseous atmosphere in the middle, which includes nitrogen, oxygen, and carbon monoxide [1].

Aluminosilicate hollow microspheres (ASHM) are the product of light fraction processing of fly ash in thermal power plants, after capture by electrostatic precipitators from the flue gas composition.

The combination of these unique properties makes the possibilities and prospects of using these microspheres in the oil, gas, chemical industry, automotive industry, refractory ceramics and construction unlimited. Microspheres are a valuable raw material, which is actively used by mining companies and construction industry companies in their technologies, as well as for the production of composite materials.

In the work [2] the authors analyzed the activities of Burshtyn, Prydniprovska, Trypillya, Kryvyi Rih and Chernihiv TPPs with the production of ash microspheres and their promotion in the industrial markets of Ukraine, Germany, Italy, Slovakia, Kazakhstan, Korea, Netherlands, Moldova, Romania and Romania. Their chemical composition directly depends on the mineral components of coal, in particular the presence of clay minerals, hydromica, quartzite and the content of quartz, pyrite, dolomite, magnesite, siderite, which undergo complex chemical and phase transformations during production processes [3].

The addition of ash microspheres to the composition of dry building mixtures and refractories gives them reduced density and thermal conductivity, the ability to dampen dynamic vibrations and vibrations, chemical inertness, which causes their use in solvents, organic liquids, acids, alkalis, water. Materials manufacturing technologies are low-temperature and are based on high fluidity, compact laying of ash microspheres, their ability to inhibit shrinkage processes during curing and polymerization of mixtures. However, it is possible to expand the areas of application and give the materials new operational properties by combining metallic and non-metallic components in one composition, which will require the introduction of high-temperature technologies.

Theoretical prerequisites for the creation of such compositions are scientific ideas about the physico-chemical processes of joining glass or ceramics with metals [4, 5], the formation of polydisperse composite media using non-metallic microspheres [6, 7] and own developments of the authors of the article on the scientific and technical bases of applying electric arc coatings filled with empty glass microspheres on a steel surface [8]. Due to the convenience and energy efficiency of electric arc spraying is considered a promising high-temperature method by which metal coatings can be applied metal-glass or metal-ceramic coatings up to 1.5 mm thick, as evidenced by [9]. The fine-grained structure of the coatings is formed during the melting of solid welding wires due to the occurrence of an electric arc between them and the transfer of compressed gas droplets on the spray surface. The experiments considered in [8, 9] include the addition of dispersed nonmetallic particles to the electric arc zone, but the use of ash microspheres in high-temperature technologies, in particular in electric arc spraying, has not yet been studied. Identifying differences and establishing patterns of formation of the structure of new dispersed coatings can be useful for the development of methods of protection of parts and mechanisms in mechanical engineering, energy, chemical industry.

The aim of the work is to experimentally prove the possibilities of using ash microspheres as a part of composite electric arc coatings on a steel surface and to establish the regularities of their structure formation.

2. Materials and Methodology

Experimental work included the formation on a substrate of carbon steel grade A284Gr.D (Ст3) (GOST 380-2005) two types of composite coatings, which used solid wires of the most affordable and inexpensive steels, capable of structural-phase transformations during thermodeformation treatment. These are wire of spring-spring steel of ferrite-perlite structure of brand 1066 (65Г) (GOST 14959-79) and low-carbon welding wire of brand ER346 (Св-08) (GOST 2246-70). Aluminosilicate hollow microspheres (ASHM) "Pinosphere" of MPk200-400 brand (manufacturer – LLC "Microspheres Production Association", Ukraine) are used as fillers, which are used in technologies of thermopanels, textured paints, etc. Aluminosilicate microspheres (TU 5717-001-11842486-2006) were used in the research, the chemical composition of which: SiO_2 – 74,9%; Al_2O_3 –13,9%; K_2O – 2,8%; Na_2O – 1,9%; Fe_2O_3 – 0,9%; CaO – 1,2%; FeO – 0,6%; TiO_2 – 0,2%. A general view of the microspheres is shown in Figure 1.

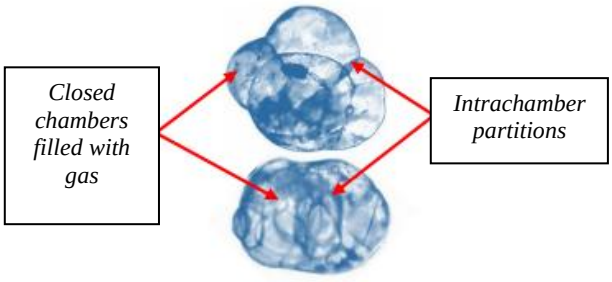

Fig. 1. *A general view of the microspheres*

ASHM are light gray solid bulk particles with a bulk density of 50… 60 kg/m3 and a dispersion of 200…400 μm. Optical microscopes MMP-2P and BIOLAM-I (БИОЛАМ-I); scanning electron microscope JSM-7610F were used for researching of

structure. X-ray diffraction analysis by DRON-3.0 (ДРОН-3.0) in molybdenum radiation $Mo_{k\alpha}$ = 0.071069 nm with U = 40 kW, 40mA were used to study morphological characteristics.

The coating with a thickness of 1.0…1.5 mm was applied on one side to the pre-treated by jet-abrasive treatment of the steel plate with a size of 3×10×140 mm. Technological modes of electric arc spraying are selected in accordance with the recommendations of the authors [9]: current strength – 80; 120; 160 A; air pressure – 0.4; 0.5, 0.6 MPa; consumption of microspheres – 150 g/min; wire feed speed – 4.2 m/min; distance from the nozzle to the spray surface – 80 mm.

The topography of the sprayed surface was studied by electron microscopy, the phase composition was studied on samples separated from the substrate by X-ray diffraction. The chemical composition of the microregions around the microspheres was studied using micro-X-ray spectral analysis using a microscope-microanalyzer REMMA-102-02 (PEMMA-102-02). The volumetric content of the microsphere coatings was determined by spot analysis with the processing of digital microphotographs.

Hardness (HV_5) was determined according to DSTU ISO 6507-4: 2008 (ДСТУ ISO 6507-4:2008) on a Vickers device with a load of 5 kg.

3. Results and discussion

The chemical composition of microspheres was investigated by X-ray diffraction analysis, which proved the general amorphous nature of microspheres, but showed the presence of α- and β-cristobalite, α- and β-quartz, and crystalline modifications of Al2O3 on diffractograms (Table 1).

Table 1: *Results of X-ray diffraction analysis of ASHM*

Reflection angle, 2θ, °	Interplanar distance, d, Å	Crystal modifications
16.7	2.447	γ-Al_2O_3
16.9	2.4189	SiO_2 (α- cristobalite)
17.05	2.397	γ-Al_2O_3
19.45	2.1036	α-Al_2O_3
20.45	2.00183	γ-Al_2O_3
20.65	1.9826	γ-Al_2O_3
22.3	1.837	SiO_2 (β- quartz)
22.55	1.817	SiO_2 (α- quartz)
22.75	1.8016	SiO_2 (α-кварц)
24.95	1.645	SiO_2 (β- cristobalite)
26.275	1.563	SiO_2 (β- quartz)
29.35	1.402	γ-Al_2O_3
30.00	1.372	γ-Al_2O_3

By means of optical analysis of microspheres, the ideal sphericity of experimental particles was established, the Gaussian distribution of which by diameter are: 80% – 200… 300 μm; 20% – 300… 400 microns.

The problem of energy saving in recent years is one of the main for all developed economies. In this regard, one of the revolutionary solutions for heat preservation can be considered liquid ceramic coatings, which at a thickness of 2…3 mm provide the same thermal insulation effect as a layer of mineral wool with a thickness of 50 mm. The method relates to the field of obtaining coatings with high strength characteristics, heat, fire and weather resistance characteristics for the protection of pipelines of heating systems and air ducts of air heating and ventilation systems.

Variation in the values of current and air pressure during application of the composite coating makes it possible to obtain samples with different fillings of microspheres: from 10 to 25%. Experimental work has shown the tendency of aluminosilicate hollow microspheres to form conglomerates and a high percentage of material loss by spraying (more than 50%), which does not allow accurate calculation of dosage and exact volume content and presents certain technological difficulties.

A schematic representation of a steel-based composite coating with the addition of aluminosilicate hollow microspheres is shown in Figure 2.

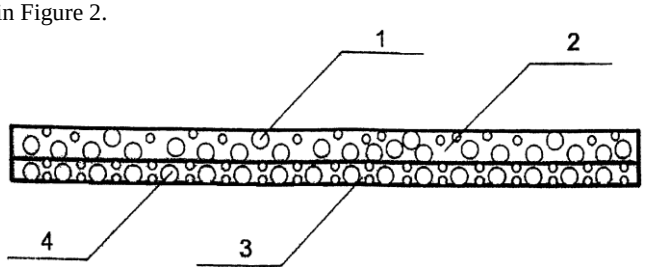

Fig. 2. *Scheme of coating with aluminosilicate microspheres: 1– microspheres; 2 - acrylic latex; 3 - layer with empty microspheres; 4 - aluminosilicate microspheres are covered with metal*

Sprayed coatings based on ER346 (Св-08) and 1066 (65Г) will have a similar polydisperse porous structure (Figure 3) with spherical inclusions, which according to the results of RSA do not undergo phase transformations. The intensity on the X-ray diffraction patterns of Fe [111] indicates that the microspheres acquire the effect of surface metallization due to envelope of dispersed molten metal, which when cooled on a steel substrate is cooled to form microvolumes with spherical inclusions.

The number of microspheres on the surface can be seen with the help of photographs of microstructures taken with the JSM-7610F scanning electron microscope. Since aluminosilicate hollow microspheres are not conductive, they are lighter in structure (figure 2, b, d).

No new chemical compounds are formed on the interface between the steel matrix and the microspheres, which shows the absence of interfacial interaction processes during electric arc spraying, which is also confirmed by the results of micro-X-ray spectral analysis. In figure 4, as an example, shows a spectrogram from the surface of the microsphere in the coating based on ER346 (Св-08).

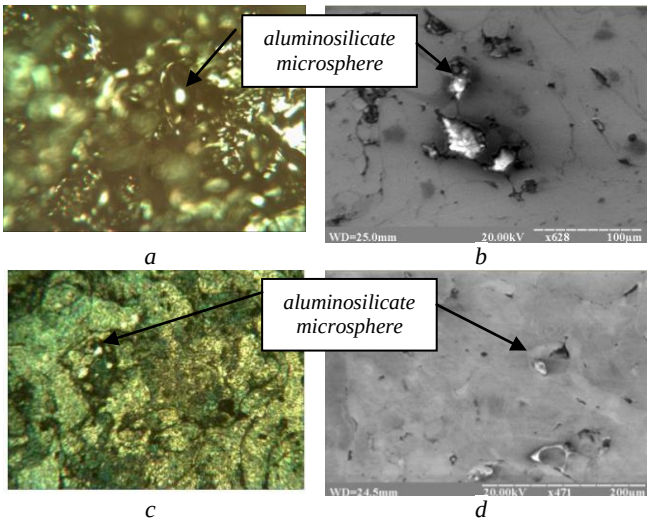

Fig. 3. *Optical micrographs of coatings filled with APHM: a – transverse section (× 150) of the composition of ER346 (Св-08); b – transverse section (× 628) of the composition of ER346 (Св-08); c – surface topography (× 150) of the composition with 1066 (65Г); d – surface topography (× 471) of the composition with 1066 (65Г)*

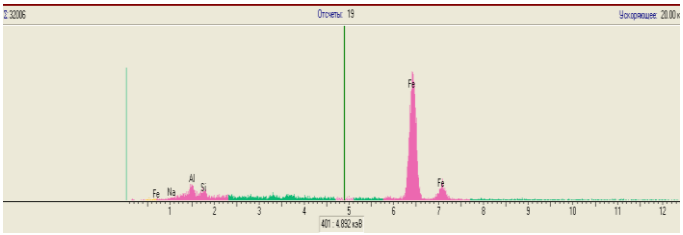

Fig. 4. *Spectrogram of aluminosilicate microsphere*

The results of research were compared to the features of the structure of electric arc coatings filled with glass microspheres and powders [10]. It was determined that the structure of the experimental coatings, in contrast to metal-glass compositions, is not associated with liquation processes in ASHM: short-term exposure to the arc jet in the walls of microspheres does not form glass phase, which will strengthen adhesive and cohesive bonds.

The effect of filling electric arc coatings with ash microspheres was determined by the results of hardness measurements HV_5 (Table 2), the measurement error did not exceed ± 10%.

Table 2: *Results of X-ray diffraction analysis of ASHM*

Material	Coating without filler	Coating with ASPM (volume 18%)	Hardness gain,%
ER346 (Св-08)	2.10	2.56	21.9
1066 (65Г)	2.50	2.70	7.4

Comparison of the results with coatings without filler showed an increase in hardness by 7… 22%, which can be explained by the formation of microstresses around the spherical inclusion in the hardening structure of the steel matrix, which arise due to differences in linear expansion coefficients.

Prospects for further work are related to the study of their physical and mechanical properties.

The use of ash microspheres in the technologies of functional coatings will have a significant economic and social effect, while associated with the creation of new compositions using cheap material resources and identifying ways to dispose of waste thermal power plants. The obtained coatings can be used in the chemical industry, energy, shipbuilding and mechanical engineering.

The research results reveal the regularities of structure formation of ER346 (Св-08) and 1066 (65Г) coatings with the addition of aluminosilicate ash microspheres deposited on steel substrate with A284Gr.D (Ст3) by electric arc method, which is aimed at solving the current scientific and technical problem of developing new coatings for industrial waste power plants. The use of ash slag in new technologies is a promising practical area, the implementation of which will help in the search for scarce minerals.

4. Conclusions

1. The possibility of adding to the composition of electric arc coatings with ER346 (Св-08) and 1066 (65Г) ash microspheres of aluminosilicate composition in a volume of 10…25% has been experimentally proved.

2. Regularities of formation of structure of composite coatings on steel substrate with A284Gr.D (Ст3) are determined: when spraying microspheres, they are enveloped by dispersed drops of molten metal, but will retain spherical shape, microcrystalline structure, phase and chemical composition; no new phases are formed on the interface between the wall and the steel matrix.

3. The efficiency of ash microspheres for the formation of coatings is determined by increased by 7… 22% Vickers hardness, as well as by economic and social values.

5. References

1. V. O. Demchenko, O. I. Simyachko, V. A. Sviderskyi, Technolohycnyi audit i rezervy vyrobnytstva. **6**. 28-34. (2017). (In Ukrainian).

2. N. V. Merezhko, V. M. Shkola, Tovaroznavchyi visnyk. **12**. 212-220. (2019). (In Ukrainian).

3. V. O. Demchenko, Visnyk Lvivskoho torhivelno-ekonomichnoho universytetu (LTEU). Tehnichny nauky. **17**. 38-41. (2016). In Ukrainian.

4. R. M. do Nascimento, A. E. Martinelli, A. J. A. Buschinelli, Cerâmica. **49**. 178-198 (2003).

5. Yu. V. Naidich, V. S. Zhuravlev, I. I. Gab, B.D. Kostyuk, V. P. Krasovskii, A.A. Adamovskyy, N. Yu. Taranets, Journal of the European Ceramic Society. **28(4).**717-728. (2008).

6. G.A. Bagliuk, V.Ya. Kurovskyi, O. Kostenko, Machines. Technologies. Materials. **Year X**, Issue 12. 52-57. (2016).

7. Z. An, J. Zhang, Materials Letters. **85**. 95–97. (2012).

8. Yu. O. Kazymyrenko, N. Yu. Lebedeva, East European Scientific Journal Wschodnioeuropejskie Czasopismo Naukowe. **5 (33), vol. 1.** 41-49. (2018.)

9. O. Syzonenko, O. Dubovyi, T. Makrukha, A. Karpechenko, M. Bobrov, A. Torpakov, Machines. Technologies. Materials. **2**. 240-243. (2021).

10. O. V. Savvova, S. M. Logvinkov, O. V. Babich, A. R. Zdoryk, Voprosy khimii i khimicheskoi tekhnologii. **3.** 96-104. (2018). (In Ukrainian).

Acknowledgements

Authors would like to express gratitude to the Armed Forces of Ukraine for their bravery which made this work possible even in the dark times of war.

About corrosion damage of the railway wheels

Svetlana Gubenko
Iron and Steel Institute of National Academy of Science of Ukraine,
Prydniprovska State Academia of Civil Engineering and Architecture
Dnepr, Ukraine
sigubenko@gmail.com

Abstract.. *Corrosion mechanism and rate of different chemical composition and structural condition of wheel steel were investigated. It was shown that "white layers", variation in grain size and banding of wheel steel structure results in corrosion rate. Microstructure of steel from different elements of railway wheels after operation with corrosion was investigated. Wheel steel with addition of vanadium corroded more quickly than steel without vanadium. Non-metallic inclusions are the centres of corrosion nucleation and their influence on corrosion depends on type of inclusion. Mechanism of corrosion of wheel steel corrosion was discussed.*
KEYWORDS: *WHEEL STEEL, RAILWAY WHEELS, CORROSION DAMAGE*

1.Introduction.

Operation and transportation of railway wheels are realized without effective anticorrosion protection. The increase in the influence of aggressive environmental factors by large industrial enterprises exacerbates the problem of preventing the corrosion damage of railway wheels [1 - 7]. Railway wheels are exposed to corrosion during operation. Corrosion fracture of steel promotes embrittlement of wheels [8 - 10]. Corrosion of different parts of railway wheel takes place in dynamic and static conditions (atmospheric, wet, soil, gas, sea-water, stress, fretting, stray-current corrosion). The goal of this work is the compare investigation of corrosion rate of wheel steel with different structure from different elements of wheels after hot deformation, heat treatment and operation.

2. Materials and Procedures.

Microstructural research of wheel after operation was done. Structural changes near tread were researched in worn-out wheel 1. The zones of corrosion in different parts of wheel 1 and non-operated wheel 3 were studied. Selection of specimens for corrosion tests were realized from different parts of tread, rim and disk of wheels 1 and 2 after operation (5 years), non-operated wheels 3 and 4. Wheel 4 was produced from steel with microalloying of vanadium, wheels 1 – 3 were from usual wheel steel. Chemical composition of wheels are given in Table 1.

Table 1. *Chemical composition of wheel steels*

Wheel	Contents of elements, %								
	C	Mn	Si	S	P	Cr	Ni	Cu	V
1	0,59	0,72	0,34	0,025	0,012	0,14	0,15	0,20	-
2	0,65	0,79	0,36	0,027	0,010	0,13	0,18	0,18	-
3	0,61	0,78	0,30	0,029	0,024	0,17	0,15	0,16	-
4	0,46	1,04	0,47	0,024	0,018	0,09	0,11	0,18	0,10

Accelerate corrosion tests were carried out in special camera with moist atmosphere contained 10 mg/m^3 SO_2, also NO, NO_2 at temperature 20-25^{0}C, time 25 days. These conditions are coincided with industry atmosphere [11], but in another operation conditions atmosphere may be aggressive too by wet, soil, sea water, etc. Before corrosion tests specimens were weighed and all their faces were covered by paraffin but one of them was exposed to corrosion.

Microstructure of corrosion zones of wheel steel before and after operation of railway wheels and also after hot deformation and heat treatment was investigated with optical microscope "Neohpot-21" and scanning microscope JSM-35.

3. Results and discussion.

Examination of wheels 1 and 2 after operation was shown that many parts of their surface are covered by rust. Oxidation of steel takes place on tread, disk, hub. The particles of oxides were discovered by metallographic research (Fig. 1). Oxidation of steel is started from surface and penetrated to considerable depth. Thus long operation of railway wheels allow to show big sections of the corrosion.

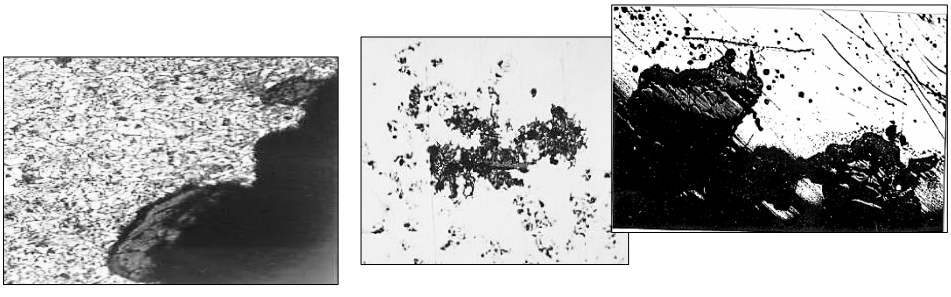

a b c

Fig. 1. *Sections of corrosion in railway wheels 1 and 2: a, c –x500, b –x200*

It is interesting to research role of corrosion processes in the development of structural changes near tread during operation of railway wheels. Macrostructural analyses of wheel 1 with heavy worn-out tread was discovered fatigue-corrosion wear accompaned distorting of the tread profile. Lots of the cracks with corrosion of steel were shown from the slidder to depth parts of the wheel. Microstructure of wheel rim near tread is characterized by presence of deformed grains zone and also sections of "white layer" [12 - 15]. The nature of structural changes is due to the combined action of thermal, dynamic and contact stresses arising in the interaction zone of wheel-rail rolling surfaces [16 - 19]. The important role of the structure of the outer surface of the wheels, which takes on external influences, should be taken into account [20 - 22].

Analyses of metallography investigation results allows to assept that structural changes happened near tread of railway wheel are accompaned by corrosion (Fig. 2). Zones of corrosion fracture were discovered along section of rim in areas with strong deformed structure also in areas of "white layer". By the roll formation on the side of rim when thin layers of steel are removaled to side of rim and disposed one over another the areas with oxidated surface of steel are finded oneself in internal parts of rim. They are arrenged between layers of deformed metal. Evidently presence of large oxide particles promotes not only to local fracture of tread areas but also to heterogeneous development of structural changes in thin layer of metal.

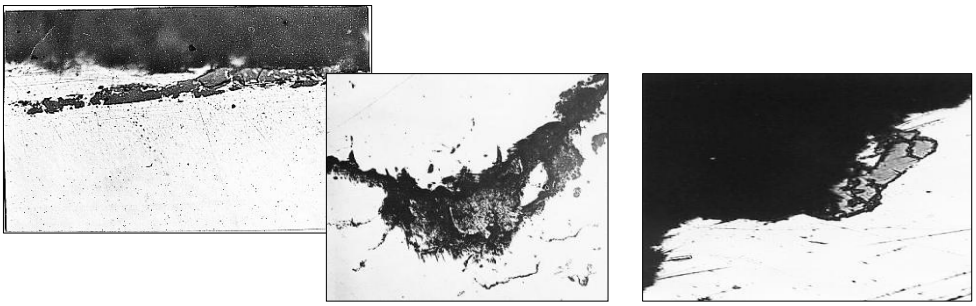

a b c

Fig. 2. *Sections of corrosion near tread of railway wheel 1 and 2 after operation: x500.*

Structural changes happened near tread were promoted different behavior of wheel steel by corrosion tests. Specimens from shabby wheels 1 and 2 were exposed to corrosion tests. Specimens from wheels 1 corroded with different rate which was decreased from cove zone along rim width and only near end of tread in the roll zone it again was increased (Fig. 3, curve 1). Thin parts of "white layer" corroded very quickly and were not discovered in structure of steel.

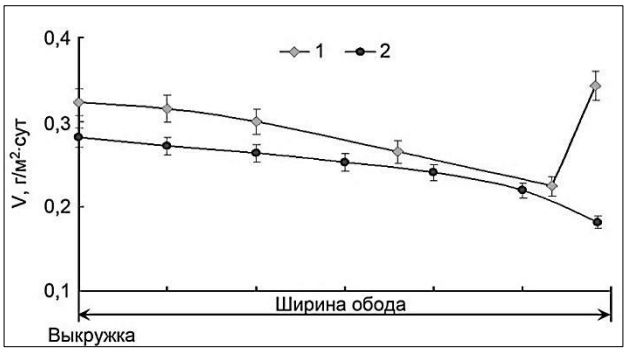

Fig. 3. *Change of corrosion rate V of specimens of wheel steel from tread along width of wheels 1 and 2 rims*

Change of corrosion rate and mechanism is obviously connected with change of character of plastic shear zone. In cove zone where grains are elongated and thin layer of steel was strongly deformed corrosion rate was maximum. Numerous small (< 20 mcm) oval pockets of localized corrosion were discovered, which were penetrated to considerable depth. In the time of corrosion the layer of elongated grains almost fully dissapeared. Maximum corrosion rate in the cove zone are explained by influence of plastic deformation created stresses in metal. In the middle of tread character of corrosion was changed. Along surface of specimens porosity corrosion film was formed and microcracks near oxides were discovered. Corrosion rate of specimens from the middle of tread and along to side of rim is essentially lower. In roll zone corrosion rate was increased again (Fig. 3, curve 1), and large pockets of the pitting corrosion were discovered. Their average size was 0,6 mm. Increase of corrosion rate of wheel steel in roll zone is explained by influence of considerable plastic deformation and also by the presence of cracks between layers of the rollig metal. Pockets of corrosion in roll zone are considerably larger then in cove zone. Thus heterogeneous plastic deformation along tread tooking place during operation of railway wheels promotes to heterogeneous corrosion fracture of tread.

Specimens from shabby wheel 2 also were corroded with different rate which was decreased from cove zone along width of rim (Fig. 3, curve 2). "White layer" was pittineged by the pitting corrosion practically on the all depth. In areas with base structure of steel (pearlite + ferrite) and small zones of "white layer" corrosion was founded on surface and penetrated deep into steel by cracks or by compact front. From the corrosion areas microcracks were penetrated into interphase boundaries ferrite-pearlite and also by

pearlite, which has well-developed interphase boundaries ferrite-cementite.

Corrosion of specimens from central part of rims of wheels 1 and 2 took place by formation of large pockets of oxidation of steel. Pockets of corrosion were formed on the surface of specimens and then were penetrated into depth of specimens and were grown by width to the contact one another. Under corrosion in oxides and on the interphase boundaries oxide-steel structural and phase stresses and microcracks were founded. Sizes of pockets of corrosion in these cases are 1…2 mm. Corrosion rate of rim metal of wheels 1 and 2 possessed ferrite-pearlite structure are approximately the same and was higher than corrosion rate of steel from tread (Tabl. 2).

Metal of disk corroded more quickly than metal of central part of rim (Tabl. 2). Corrosion process was spreaded along pearlite areas, and also along ferrite-pearlite boundaries. Kind of corrosion damages of metal from rim and disk is different: in the first case small pockets of corrosion were discovered, in second case large pockets of corrosion were discovered. From the pockets of corrosion intercrystalline cracks were spreaded along pearlite and ferrite-pearlite boundaries. Corrosion rate of specimens from disk of wheel 1 was a little higher then corrosion rate of disk of wheel 2.

Table 2. *Results of corrosion tests of wheel steels*

Wheel №	Place of specimens selection	Microstructure of wheel steel	Corrosion index		h, mcm
			K_1,g/cm^2	K_2,g/m^2.h	
1	middle of tread after operation	elongated grains of ferrite and pearlite	24,058	0,408	222
2		“white layer”	22,9643	0,359	204
1	central part of rim after operation	equiaxed grains of ferrite and pearlite	13,30	0,225	140
2		equiaxed grains of ferrite and pearlite	17,0642	0,289	125
1	disk after operation	ferrite and pearlite, banding	21,7702	0,389	166
2		ferrite and pearlite, no banding	22,8889	0,368	159
4	tread after heat treatment	sorbite of tempering	17,8182	0,302	148
4	central part of rim after heat treatment	ferrite and pearlite	18,8102	0,319	167
3	tread after heat treatment	sorbite of tempering	19,6316	0,327	115
3	central part of rim after heat treatment	ferrite and pearlite	24,069	0,401	138

Corrosion of specimens from tread of heat treated wheels 3 and 4 (with addition of vanadium) having structure of sorbite of tempering had lamellar or film character. Specimens from central part of rim of wheels 3 and 4 had the same character of corrosion (Fig. 4, a, b). Brittle cracks were spreaded from the porosity oxides to steel. Steel with addition of vanadium corroded more quickly than ordinary wheel steel (Tabl. 2). It is known vanadium promotes to decrease of corrosion resistance of steel and influence of manganese is the same [1]. The tread after heat treatment corroded more quickly than tread after operation. Corrosion of specimens from central part of rims of wheels 3 and 4 had pitting character with small pockets of corrosion and cracks were spreaded by the pearlite. Steel with addition of vanadium corroded more quickly than ordinary wheel steel (Tabl. 2). It is known the steels with martensite structure have a low corrosion resistance [1]. By heat treatment in martensite structure considerable stresses are formed which decrease corrosion resistance of steels. Also the martensite structure decreases the resistance of brittle fracture of steels. So martensite structure is inadmissible in railway wheels.

Investigation of corrosion product of wheel steel was discovered the heterogeneous structure of powder. Upper part is white powder – hydrate $Fe(OH)_2$, under it - red rust containing Fe_{com} - 48,25%, Mn - 0,37%, C - 2,87% (Fig. 5).

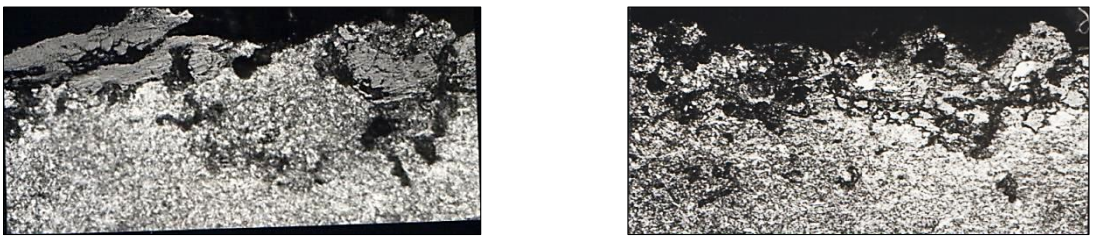

a b

Fig. 4. *Microstructure of surface of wheel steel specimens with addition of vanadium (a) and ordinary wheel steel (b) after corrosion tests: x200*

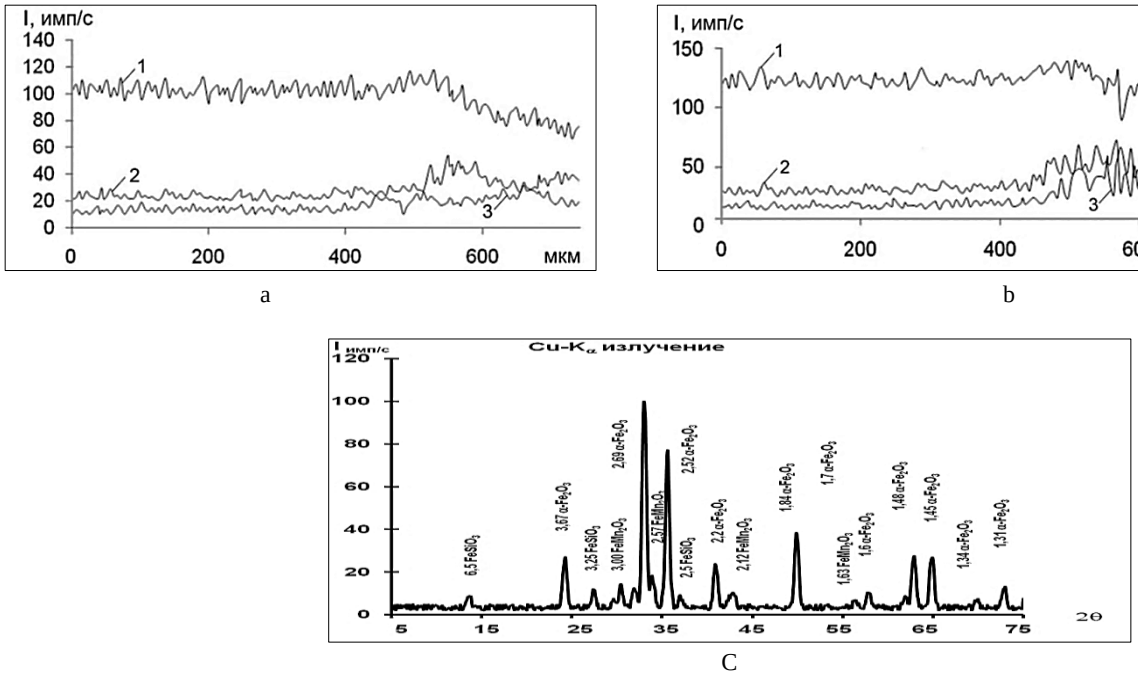

Fig. 5. *Distribution of chemical elements in oxide phases of corrosive origin (a, b; cur. 1 - Fe, cur. 2 - Si, cu. 3 - Mn) and the phase composition of corrosion products of the wheel steel (c)*

Different corrosion rate of wheel steel is explained by its different structural state. In worn-out railway wheels tread corroded more quickly than metal from central part of rim. This is explained by influence of stresses creating plastic deformation in thin surface layer. Areas of "white layer" on the tread promote delay of corrosion. These connect with ultrafine structure of the "white layer" [2, 3]. Metal from disk corroded more quickly than metal from central part of rim thanks to more rough of ferrite-pearlite structure of disk and also more ferrite banding of steel structure.

In heat treated railway wheels tread corroded more slowly than metal from central part of rim. This connect with more disperse ferrite-pearlite steel structure of tread after heat treatment. Microaddition of the vanadium promotes accelerate of corrosion of tread and metal from central part of rim.

Principles of wheel steel structure influence on the corrosion rate are confirmed also by results of definition of the depth of corrosion penetration *h* from surface to specimens having different microstructure (Tabl. 2). Average value of *h* was determined from the depth of all researching corrosion zones by metallography method. By analysis of these results it is necessary to take into value of *h* are cited for middle part of tread after operation

It is known the considerable thermal and deformational stresses causing by different physical-mechanical properties of non-metallic inclusions and steel matrix are exited near these particles [23]. Stresses are formed on the different stages of railway wheels production. Concentration of stresses promotes reinforcement of corrosion damage for all kinds of non-metallic inclusions. of wheels 1 and 2. But in cove zone of wheel 1 value of *h* was 342 mcm, in roll zone – about 600 mcm.

Thus corrosion rate is smaller when structure of the wheel steel is more disperse. Coarse-graininess, variation in grain size and banding of wheel steel structure promotes increase of corrosion rate.

Research of corrosion areas in railway wheels after operation and heat treatment before operation was shown the big influence of non-metallic inclusions on process of corrosion (Fig. 6). One of the main factors defining corrosion behavior of wheel steel is electro-chemical heterogeneity of railway wheel surface. Presence of non-metallic inclusions differing from steel matrix by physical-chemical properties results in corrosion microcells and reinforcement of electro-chemical heterogeneity of railway wheel surface [8, 9, 20, 23]. In wheel steel oxides Al_2O_3, $MnO{\cdot}Al_2O_3$, (Fe,Mn)O, sulphides (Fe,Mn)S, silicates SiO_2, $MnO{\cdot}SiO_2$, $FeO{\cdot}SiO_2$ and carbo-nitrides TiCN are present. All these non-metallic inclusions are cathodes by relation to metal matrix and they are arranged in order to decrease of the value of electrode potential difference of wheel steel surface near non-metallic inclusions in decreasing series: sulphides, corundum, silica, nitride of titanium. Increasing series by electrical resistance of non-metallic inclusions is the same.

Especially it is displayed by applying of the stresses. In our research the nucleation and localization of corrosion fracture of wheel steel was observed near different kinds of non-metallic inclusions in worn-out railway wheels and also in heat treated railway wheels.

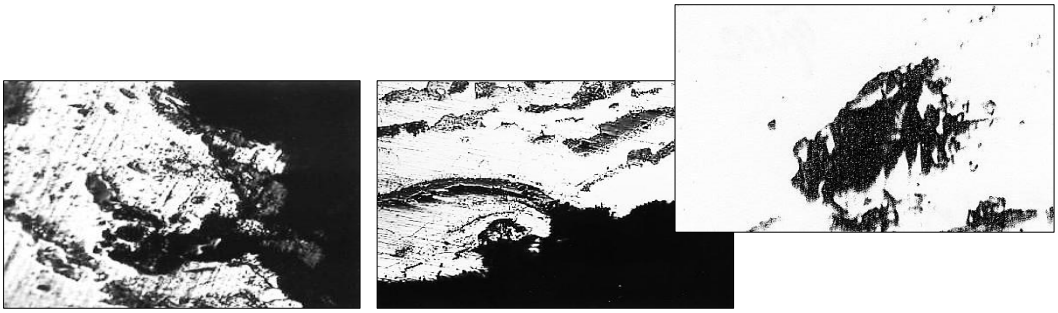

a b c

Fig. 6. *Corrosion fracture of wheel steel near non-metallic inclusions; x600*

Thus metallurgical factor namely contaminant of wheel steel by non-metallic inclusions is very important in the problem of corrosion fracture of railway wheels.

Corrosion is very dangerous for reliability and service life of railway wheels. It is known by the tests in air the time for nucleation of fatigue crack on the surface of metal can to compose till 90% from common service life of metal but corrosion promotes shortening of its share till 10% [5]. Chemical energy releasing in results of corrosion can to compose effective surface energy necessary for nucleation of crack. Wear-resistance of tread depends on surface condition. Formation of the oxides on the tread by corrosion of steel changes properties of this surface (strength, plasticity, wear-resistance) and influence on the condition of interaction between railway wheel and rail during operation.

4. Conclusions.

Corrosion of railway wheels during operation is decreased their reliability and service life. Mechanism and corrosion rate depend on chemical composition and structural condition of wheel steel. Non-metallic inclusions render great influence on corrosion fracture of railway wheels. It is necessary to work out anticorrosion actions during all stages of wheel production, keeping of railway wheels, their transportation to consumer and also their operation.

5. Literature.

1. Feraud P., Viet J., Diener M., Grab M.. Influence of corrosion on the behavior of wheelsets in service // The 15-th International Wheelset Congress (October 2007): Praga.Chesh. Repub, 2007, pp. 308-314.

2.. Beretta S., Carboni M., LoConte A.. Impact of corrosion upon fatigue properties of ainsteel // The 15-th International Wheelset Congress (October 2007): Praga.Chesh. Repub, 2007, pp. 294-300.

3. Resource and maintainability of wheelsets of rolling stock of railways / Vorobyov A.A., Gubenko S.I., Ivanov I.A. and others // Moscow: INFRA-M, 2011. – 264 p.

4. Influence of the structure and mechanical characteristics of wheel steels on the wear and modes of restoration of the profile of wheel sets /V.S. Kushner, A.A. Kutko, A.A. Vorobyov, S.I. Gubenko, I.A. Ivanov. // Omsk: ed. OmGTU, 2015. - 221 p.

5. Bogdanov A.F., Gubenko S.I., Zhukov D.A., Ivanov I.A. Surface layer and operational properties of the solid-rolled wheel rim \\ Structural and technological support of the reliability of the wheels of rail vehicles. Sat scientific. tr. PGUPS, St. Petersburg, 2009, pp. 15-23.

6. Changes in the rim surface and wheel life during operation / Bogdanov A.F., Budyukin A.M., Gubenko S.I., Ivanov I.A., Urushev S.V. // Structural and technological support of the reliability of the wheels of rail vehicles. Sat scientific. tr. PGUPS, St. Petersburg, 2009, pp. 23-40.

7. Bogdanov A.F., Gubenko S.I., Zhukov D.A., Ivanov I.A.. Surface Layer and Performance Properties of Solid Wheel Rim // Transport and engineering. Railway Transport, Scientific Proceedings of Riga Technical University, 2008, N 30, pp. 56-61.

8. Gubenko S.I., Pinchuk S.I., Belaya E.V.. Investigation of non-metallic inclusion effect on corrosion behavior of wheel steel. Metallurgical and Mining Industry, 2011, N 3 (2), pp. 63-66.

9. Gubenko S. I.. Influence of Nonmetallic Inclusions and Corrosion Products on the Wear Resistance of Railroad Wheels. Steel in Translation, 2019, v. 49, N. 6, p. 427–431.

10. Pinchuk S., Gubenko S., Belaya E.. Correlation between electrochemical corrosion and structural state of steel by simulation of operation conditions of railway wheels. Chemistry & Chemical Technology. Publishing House of Lviv Polytechnic National University, 2010, № 4 (2), p[. 151-158.

11. Karpenko G.V. , Vasilenko II. Corrosion cracking of steels. K .: Technique, 1971. - 191 p.

12. Taran Yu. N., Esaulov V. P., Gubenko S. I. Increase of wear-resistanceof railway wheels with different profile of trea. Metallurgical and Minning Industry, 2000, N 2, pp. 42-44.

13. Taran Yu. N., Esaulov V. P., Gubenko S. I. Structural changes in rims of railway wheels with different profile of tread. News of Higher Education. Black Metallurgy, 2989, N 9, pp. 101-105

14. Gubenko S., Proidak Y .. Investigation of wear mechanism of tread during operation of railway wheels. Transport problems, 2012, N 7, pp. 119-125.

15. Wear reduction on working surface of railway wheels / Taran Y, Yessaulov V, Sladkovsky A, Kozlovsky A, Gubenko S. WIT Transactions on Modelling and Simulation, 1970, v. 23, N 1, pp. 45-52.

16. Savrukhin A.V., Neklyudov A.N., Efimov R.A. Modeling of the thermal loading of solid-rolled wheels. World of Transport, 2014, N 5, pp. 22-30.

17. Stresses-deformed state of railway wheels of different design / Taran Uy., Esaulov V., Gubenko S., Sladkovsky A., Staroseletsky M. // Proceedings of the 13-th International Wheelset Congress (17-21 Sept. 2001). Rome: Italy, 2001, pp. 305-311.

18. An Analysis of Stress and Strain in Freight Car Wheels. / Sladkovsky A., Yessaulov V., Shmurygin N., Taran Y., Gubenko S. Transactions on Modelling and Simulation, 1997, N 16, pp. 15-24.

19. Rail vehicle dynamics and associated problems: monograph / Sladkowski A., Gubenko S., Pogorelov D., Iwnicki S., Licciardello R.V. Gliwice: Silesian University of Technology, 2005, 187 ppp.

20. Improving the performance of wheel sets of rolling stock / Valinsky O.S., Vorobyov A.A., Gubenko S.I., Ivanov I.A., Kerentsev D.E. Krotov SV , Urushev S.V. // Kazan, Izd.OOO "Buk", 2022. - 324 p.

21. Ivanov I.A., Gubenko S.I., Kononov D.P. Surface of machine and mechanism parts. St. Petersburg: LAN, 2021. - 156 p.

22. Gubenko Svetlana. Physical nature of the plasticity and strengthening of metals under deformation. Germany-Mauritius, Beau Bassin,: LAP LAMBERT Academic publishing, 2020. - 341 p.

23. Gubenko S.I., Oshkadepov S.P. Non-metallic inclusions in steel. – Kiev: Naukova dumka, 2016. - 528 p.

Деформационно поведение на материалите, използвани при изграждането на пружиниращата част от структурата на тапицерията

Deformation behavior of the materials used in the construction of the springing part of the upholstery structure.

Rostislav Bozhkov
University of Forestry, Bulgaria
10 bulevard Sv. Kliment Ohridski, Sofia, Bulgaria
rostislav.bojkov@gmail.com

Abstract: *Polyurethane foams and spring packages type "Bonnel" and "Pocket" are some of the basic materials in the construction of the springing part of the upholstery structure in the furniture industry. The produced soft and elastic polyurethane foams, as well as spring packages are in many variants, according to their load characteristics.*

The study looked at the deformation behaviour of two types of polyurethane foam and two types of spring packages used in the construction of the upholstery of modern upholstered furniture. The criteria used to assess the material are a softness coefficient and parameters for general deformation of the upholstery, in the specifics of the elements of the seat and the backrest.

Based on the results obtained, conclusions and recommendations have been made for their application in the upholstery structure of upholstered furniture.

Keywords*: Polyurethane foam, spring packages, upholstery, structure, density, deformation.*

1. Въведение

Производството на тапицирани мебели заема голям дял от общото производство на мебели. Причина за това е голямата степен на функционалност и задоволяване на утилитарните изисквания на потребителя. Трябва да се отбележи и факта, че потребителите изпълняват голяма част от дейностите си през денонощието (четене, писане, работа на компютър, хранене, развлечение, седене в транспортно средство, почивка, лежане, спане и др.) при експлоатация на тапицирани мебели.

Делът на производство на тапицирани мебели възлиза на 35% от общия дял на произведените мебели в европейски и световен мащаб. С всяка изминала година, той бележи ръст или в най-добрия случай се запазва, поради непрекъснатото откриване на нови материали за изграждането на тапицерската структура, както и внедряването на модели с нови форми и конструкции.

Полиуретановите пеноматериали са синтетични, леки, с равномерна клетъчна структура. Разделят се на следните основни групи: меки, полутвърди, твърди и интегрални.

В последните години на пазара се налагат все повече трудногоримите меки пенополиуретани, които отговарят на европейските и американски стандарти за опазване здравето на хората и са задължителни при производството на тапицирани мебели за обществени сгради, градски транспорт и др.

Основните критерии за избора на пенополиуретаните са плътност, твърдост, наричана в България „мекост“, еластичност и остатъчна деформация. Всички тези характеристики са тясно свързани с критериите за удобство и комфорт, дълготрайност и износоустойчивост.

Твърдостта е една от най-важните характеристики за поведението на полиуретановите пени, особено за малки натоварвания [4,5,10].

До настоящия момент не е ясно изяснено влиянието на дебелината на материалите върху стойността на критериите, характеризиращи деформационното им поведение в структурата на тапицерията. За използваните в България материали за тапицерия има ограничена, непълна и в голяма степен неясна информация. Всеки производител на тапицирани мебели разчита главно на опита си и до голяма степен на правилото „проба-грешка” при внедряването на нови материали в тапицерското производство, голяма част от които са със задължителни характеристики, съгласно Европейското законодателство и стандарти. Това води до допускане на грешки, производствени и финансови загуби и трудности при правилното въвеждане и използване на материалите в структурата на тапицираните мебели.

В България са направени задълбочени, подробни и аналитични проучвания на материали, използвани в различни видове тапицерия [3]. В тях е обобщен опита в тази насока до 2000-та година, поради което с днешна дата данните не могат да се считат за валидни. Голяма част от изследваните материали вече не се прилагат в структурата на тапицираните мебели.

Изследвани са тапицерии с пружинни пакети с различни комбинации от материали [6]. Тествано е поведението на напрежение на конвеционални (N) и високоеластични (HR) полиуретанови пени с различна дебелина [7].

Към днешна дата не са изследвани стандартните трудногорими (СМЕ) меки пенополиуретанови пени, които навлизат все по-масово в изграждането на структурата на тапицерията и не е правен сравнителен анализ на деформационното им поведение спрямо конвенционалните полиуретанови пени (N).

Целта на това изследване е определянето на деформационното поведение при натоварване на тапицерии с пружиниращ част, изградена от конвенционални и/или СМЕ пенополиуретани, както и от пружинни пакети тип „Бонел“ и „Покет“.

2. Материали и метод

На изследване са подложени два основни типа тапицерии (фиг.1): **A** и **B** - с пружиниращ част, изградена от пружинен пакет тип „Бонел“ и „Покет“, **C** и **D** - с пружиниращ част, изградена от конвенционална полиуретанова пяна – KOVAFOAM N 3540 и трудногорима полиуретанова пяна KOVAFOAM СМЕ 3530, произведени по непрекъснат метод от Паралел Севлиево ООД.

Всички останали материали, използвани при изграждането на тапицерската структура са идентични по вид и дебелина и с еднакви физико-механични характеристики. Това е необходимо, за да бъде достоверно направеното сравнение на деформационното поведение на изследваните материали.

Тестът се извършва по стандартен метод съгласно БДС 8962:1990 [1]. Тествани са образци с размери 600x600 mm., което от своя страна води до сравнимост на резултатите

от теста с тези на тапицерия с подобни размери. Дебелината на изследваните пружинни пакети тип „Бонел“ (2), „Покет“ (2-1), конвенционалната полиуретанова пяна N 3540 (2-2) и на трудногоримата полиуретанова пяна KOVAFOAM CME 3530 (2-3) е 140 mm. Общата дебелина на всички изследвани тапицерски структури е 250 mm. (фиг.2.1).

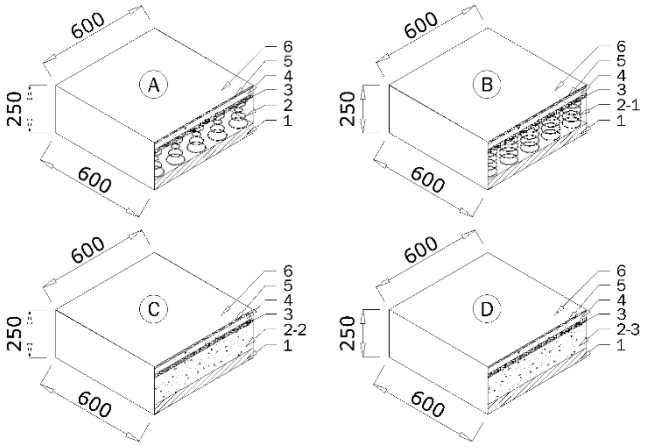

Фиг.1. *Основни схеми на изграждане на структурата на тапицерията: 1 –твърда основа на тапицерията: 2 - пружинен пакет тип „Бонел-Стандарт”; 2-1 пружинен пакет тип „Покет-Стандарт” 2-2- конвенционална полиуретанова пяна KOVAFOAM N 3540; 2-3- трудногорима полиуретанова пяна - KOVAFOAM CME 3530; 3 - Тапицерска вложка; 4- конвенционална полиуретанова пяна KOVAFOAM N 3030 5- Полиестерна вата; 6 - Мебелен плат.*

Преди изпитването, образците се кондиционират в продължение на 24 часа в среда от 23±2 ° С и относителна влажност 50±5 % .

Изпитваните образци са закрепени за хоризонтална, твърда, гладка основа с отвори ϕ 35 mm., позволявайки изтичането на въздух отдолу на образеца. Пробите предварително се зареждат с последващо разтоварване, след което са оставени 30 min за кондициониране. Първоначалната дебелина (височина) на образците е записана при товар от 3 daN. След постепенно увеличаване на силата, следващите дебелини на образците са отчетени на интервали от 5 daN (до 20 daN) и на интервали от 10 daN (от 20 daN до 100 daN).

Използваният натоварващ диск за изследването е плосък с кръгла форма, с диаметър 250 mm.

Изследваните показатели са:

- Коефициент на начална мекост ($M_н$), който се изчислява по формулата:

(1) $$M_H = \frac{H_5 - H_{15}}{10}$$, mm/daN.

където:

H_5 е височината на образеца при натоварване със сила от 5 daN,mm.

H_{15} - височината на образеца при натоварване със сила от 15 daN,mm.

Обща деформация на облегалката ($Д_{о.о.}$) и Обща деформация на седалката (До.с.) и се изчисляват по формулите:

(2) $Д_{о.о.} = H_0 - H_{30}$, mm.

(3) $Д_{о.с.} = H_0 - H_{75}$, mm.

където:

H_0 е началната височината на образеца.

H_{30} - височината на образеца при натоварване със сила от 30 daN,mm.

H_{75} - височината на образеца при натоварване със сила от 75 daN,mm.

- Коефициент на мекост на облегалката ($K_{м.о.}$) и Коефициент на мекост на седалката ($K_{м.с.}$) и се изчисляват по формулите:

(4) $$K_{M.O.} = \frac{H_{30} - H_{40}}{10}$$, mm/daN.

(5) $$K_{M.C.} = \frac{H_{75} - H_{85}}{10}$$, mm/daN.

където:

H_{30} е височината на образеца при натоварване със сила от 30 daN,mm.

H_{40} - височината на образеца при натоварване със сила от 40 daN,mm.

H_{75} - височината на образеца при натоварване със сила от 75 daN,mm.

H_{85} - височината на образеца при натоварване със сила от 85 daN,mm.

Съгласно БДС 7669-89. „ Мебел. Тапицерия. Технически изисквания.” [2], меката мебел се класифицира в зависимост от степента на мекост, определяща се от стойностите на деформацията и коефициент на мекост на:

- Полутвърда - такава тапицерия отговаряща на:
  $Д_{о.} \leq 35$ mm.
  $K_м$ – не е нормиран.

- Полумека - такава тапицерия отговаряща на:
  $Д_{о.}$ - от 35 mm. до 75 mm.
  $K_м$ - от 1,4 mm/daN. до 2,4 mm/daN.

- Мека - такава тапицерия отговаряща на:
  $Д_{о.} > 75$ mm.
  $K_м \geq 2,4$ mm/daN.

3. Резултати и анализ

Резултатите на показателите за мекостта на изследваните различни схеми на тапицерски структури са представени в таблица 1. Те се характеризират със стойности, покриващи изискванията на БДС 7669-89. „Мебел. Тапицерия. Технически изисквания“ за полумека и мека тапицерия [2].

От таблица 1 и фигура 2 е видно, че тапицерската структура тип А продължават своята деформация до натоварване с 100 daN, докато тапицерската структура тип В до 80 daN. Това се дължи на по-малкия диаметър на телта, използвана при производството на цилиндричните пружини за пружинен пакет тип „Покет“, както и на различната структура на пружинния пакет.

Табл. 1. *Показатели за мекост на изследваните тапицерски структури.*

Тип:	Мн (mm/daN)	До.о. (mm)	До.с. (mm)	Км.о. (mm/daN)	К м.с. (mm/daN)
A	1,6	72	110	2,5	2,4
B	1,4	73	128	2,7	2,5
C	0,7	68	108	2,2	2,1
D	1,8	78	130	2,8	2,7

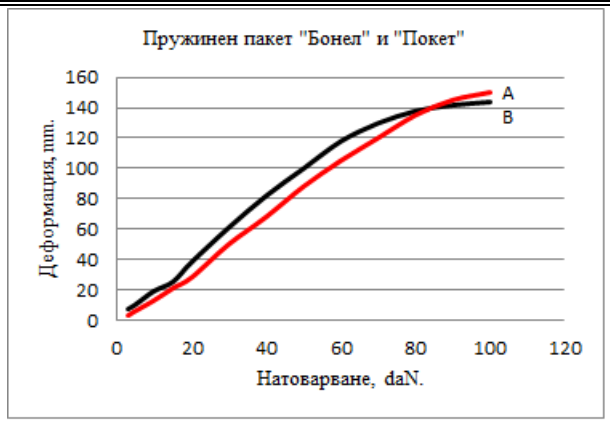

***Фиг. 2**. Деформация при натоварване на тапицерска структура с пружинираща част, изградена от пружинен пакет тип „Бонел“ и „Покет“.*

Получените резултати при изпитване на пробните тела на тапицерските структури тип С (с пружинираща част, изградена от конвенционална полиуретанова пяна – KOVAFOAM N 3540) и тип D (с пружинираща част, изградена от трудногорима полиуретанова пяна KOVAFOAM CME 3530), са показани в таблица 1 и фигура 3. Тапицерската структура тип С продължава своята деформация до натоварване с 100 daN, докато тапицерската структура тип D продължава деформацията си до 90 daN. Това се дължи на различните физико-механични свойства на двата пенополиуретана KOVAFOAM N 3540 и KOVAFOAM CME 3530).

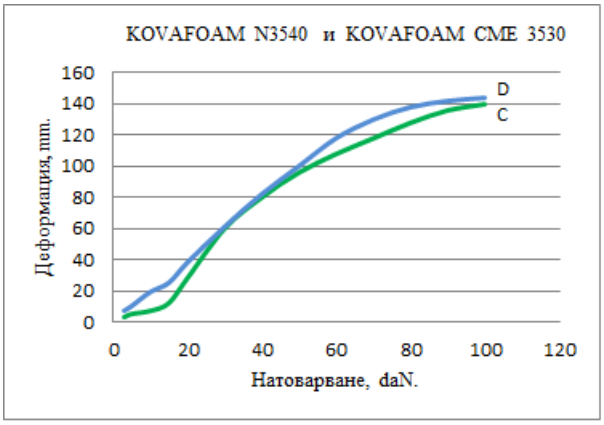

***Фиг.3** . Деформация при натоварване на тапицерска структура с пружинираща част, изградена от конвенционална полиуретанова пяна – KOVAFOAM N 3540 и трудногорима полиуретанова пяна KOVAFOAM CME 3530.*

От таблица 1 и фигура 4 и направен анализ е видно, че изследваните тапицерски структури тип A,B,C и D покриват изискванията на БДС 7669-89. „Мебел. Тапицерия. Технически изисквания“ [2] и критериите за изграждане на тапицерската структура (седалката - мека тапицерия, облегалката - мека или полумека тапицерия и подлакътниците - твърда тапицерия), както и в голяма степен критериите за Удобство и Комфорт на тапицираните мебели.

Показателите на обща деформация на облегалката ($Д_{о.о.}$) при тапицерия тип А и В покриват критериите за полумека тапицерия, докато показателите на обща деформация на седалката ($Д_{о.с.}$), при двете тапицерски структури, покриват критериите за мека тапицерия. Изчислените коефициенти на мекост на облегалката ($К_{м.о.}$) и коефициента на мекост на седалката ($К_{м.с.}$) при тапицерия тип А са на долната граница, докато при тапицерия тип В напълно покриват критериите за мека тапицерия. Това показва пригодността за използване на тапицерските структури тип А и В, главно за изработване на седалката, и в по-малка степен за изработване на облегалката на тапицираните мебели, осигурявайки постигането на критериите за Удобство и Комфорт на тапицираните мебели. Основната причина за ограниченото използване на тези видове тапицерски структури за облегалката на тапицираните мебели е заложената в тях дебелина от 250 mm., както и използването на твърда тапицерска основа. Тези факти ги правят с ограничен ресурс за постигане на форми на седалката, отличаващи се със съвременен дизайн и добра ергономичност.

Показателите на обща деформация на облегалката ($Д_{о.о.}$), при тапицерия тип С, покриват критериите за полумека тапицерия, докато на тапицерия тип D за мека тапицерия. Показателите на обща деформация на седалката ($Д_{о.с.}$), при двете тапицерски структури, покриват критериите за мека тапицерия. Изчислените коефициенти на мекост на облегалката ($К_{м.о.}$) и коефициента на мекост на седалката ($К_{м.с.}$) при тапицерия тип С покриват критериите за полумека тапицерия, докато при тапицерия тип D напълно покриват критериите за мека тапицерия.

Стойността на показателите показват, че тапицерските структури тип С (с пружинираща част, изградена от конвенционална полиуретанова пяна – KOVAFOAM N 3540) и тип D (с пружинираща част изградена от трудногорима полиуретанова пяна KOVAFOAM CME 3530) имат добри показатели за изработване на облегалката на тапицираните мебели, осигурявайки постигането критериите за Удобство и Комфорт на тапицираните мебели. Тапицерската структура тип С се характеризира със стойности на показателите си за мекост, покриващи изискванията за полумека тапицерия. Това обстоятелство я превръща в не особено подходяща при изработване на седалката на тапицираните мебели. Препоръчва се използването на допълнителни материали в структурата и за постигане на стойности, отговарящи на изискванията за мека тапицерия.

Тапицерска структура тип D (с пружинираща част, изградена от трудногорима полиуретанова пяна KOVAFOAM CME 3530) има деформационно поведение, което в по-голяма степен покрива критериите за Удобство и Комфорт на тапицираните мебели.

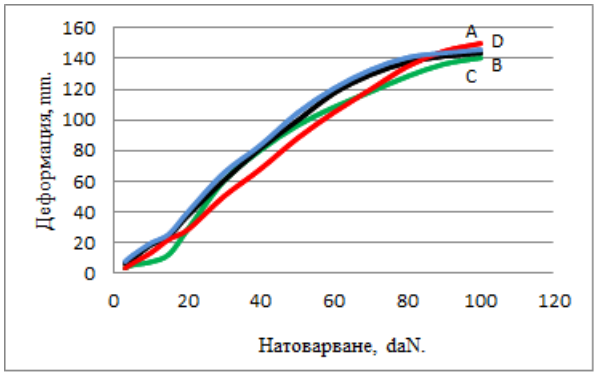

***Фиг. 4**. Деформация при натоварване на тапицерска структура с пружинираща част, изградена от пружинен пакет тип „Бонел“ и „Покет“, конвенционална полиуретанова пяна – KOVAFOAM N 3540 и трудногорима полиуретанова пяна KOVAFOAM CME 3530.*

4. Заключение

Въз основа на направените изследвания на тапицерските структури тип А (с пружинираща част изградена от пружинен пакет тип „Бонел“), тип В (с пружинираща част изградена от пружинен тип „Покет“), тип С (с пружинираща част изградена от конвенционална полиуретанова пяна – KOVAFOAM N 3540) и D (с пружинираща част изградена от трудногорима полиуретанова пяна KOVAFOAM CME 3530), могат да се направят следните изводи:

1. Видът на тапицерската структура оказва влияние върху деформационното поведение на тапицерията;

2. Тапицерските структури тип С (с пружинираща част изградена от конвенционална полиуретанова пяна – KOVAFOAM N 3540) и D (с пружинираща част изградена от трудногорима полиуретанова пяна KOVAFOAM CME 3530) се характеризират с подобно поведение подложени на напрежение на натиск, сравними с тапицерските структури тип А (с пружинираща част изградена от пружинен пакет тип „Бонел“), тип В (с пружинираща част изградена от пружинен пакет тип „Покет“).

3. Изследваните тапицерски структури отговарят на изискванията на БДС 7669-89. „Мебел. Тапицерия. Технически изисквания“ за полумека и мека тапицерия.

4. Изследваните тапицерски структури могат да бъдат използвани успешно за производството на седалките и облегалките на съвременни тапицирани мебели.

4. Литература

1. БДС 8962-90. *Мебел. Мебел за седене и лежане. Метод за изпитване на мекост.* К29. С., Комитет по стандартизация,сертификация и метрология, 1991.
2. БДС БДС 7669-89. *Мебел. Тапицерия. Технически изисквания.* К25. С., Комитет по качество, 1990.
3. Генчев, Я. *Оптимизиране структурата на тапицерията на меката мебел*. Дисертация за получаване на образувателна и научна степен „Доктор”. София, 1998.
4. BDS EN ISO 3386-1:2010. *Polymeric materials, cellular flexible – Determination of stressstrain characteristic in compression* – Part 1: Low density materials.
5. BDS EN ISO 2439:2009. *Flexible cellular polymeric materials – Determination of hardness (indentation technique)* (ISO 2439:2008).
6. Genchev, J., Lulchev T., Hristodorova D. (2016): *Influence of the type of upholstery materials on the softness of upholstery with inner spring units*. INNOVATION IN WOODWORKING IDUSTRY AND ENGINEERING DESIGN,1/2016(9)
7. Genchev, J., Lulchev T. (2015): *Comparative Analysis of the deformation behavior of upholstery materials*. SECOND INTERNATIONAL SCIENTIFIC CONFERENCE „WOOD TECHNOLOGY & PRODUCT DESIGN ―,2015, OHRID, REPUBLIC OF MACEDONIA
8. Jancova, V. *Reciprocni perfomace souboru poliuretanovy pen v konstrukcie alounenovi nabutku*. 2008.
9. Polyurethane foam association, (1991): *Density.* InTouch Technical Bulletin Vol.1, No.2.
10. Polyurethane foam association, (1994): *Firmness.*InTouch Technical Bulletin Vol.4, No.3.
11. Zubauskiene, D. Strazdiene, E. Urbelis, V. Sacevivience, V. *The Investigation of Soft Furniture Upholstery Deformational Behaviour*. L., ISSN 1392–1320 MATERIALS SCIENCE (MEDŽIAGOTYRA). Vol. 18, No. 4. 2012.

Analytical approach to crack tip plasticity of dental CoCrMo alloy

Martina Lovrenić-Jugović[1,*], Ljerka Slokar Benić[1] , Ivan Jandrlić[1]
University of Zagreb, Faculty of Metallurgy, Croatia[1]
mlovrenic@simet.unizg.hr

Abstract: *In this paper, a thin infinite plate of CoCrMo alloy with a straight crack was loaded perpendicularly to the crack plane. CoCrMo alloys are due to their suitable mechanical and corrosion properties widely used for dental applications. The importance of good mechanical properties is reflected in ensuring the functional and technical durability of dental appliances. The intention of this paper is to use a mathematical approach in analyzing a thin infinite plate with a straight crack to the rather complex occurrences within the cohesive zones around the crack tips. The dependence of plastic zone magnitude around the crack tip on an external load of dental CoCrMo alloy plate was considered in this paper. Static tensile tests were carried out to determine the mechanical properties of dental CoCrMo alloy. At plastic deformation, the dental CoCrMo alloy is nonlinearly hardened in accordance with the Ramberg-Osgood equation which parameters were determined using a least-squares method from experimental data. The application of the Dugdale model the plastic zone magnitude around the crack tip was determined. The stress intensity coefficient from the cohesive stresses was calculated using Green functions. The analytical methods, assuming a small plastic zone around a crack tip, were used in the analysis. The results were obtained by means of a commercial software package and presented in the form of diagrams.*

Keywords*: CrCoMo ALLOY, STRAIN HARDENING EXPONENT, DUGDALE MODEL, PLASTIC ZONE MAGNITUDE AROUND CRACK TIP*

1. Introduction

In spite of the fact that numerical methods are widely used in solving engineering problems in different fields of mechanics, in particular the finite element method, the analytical methods will be applied in solving the problems presented in this paper. A straight crack, with the length 2*a*, in a thin infinite plate loaded on its edges, is considered here. The plate is made of a ductile material (dental CoCrMo alloy); therefore, cohesive zones around crack tips occur when the plate is loaded. Our aim is to investigate the dependence of the magnitude of the plastic zone around crack tip r_p on an external load of dental CoCrMo alloy plate. The mechanical properties of dental CoCrMo alloy were determined by performing a static tensile test. It is an alloy that, in addition to the absence of nickel, its biocompatibility and corrosion resistance, has excellent mechanical properties such as hardness, tensile strength**,** and toughness [1]**.**

Since there is a lack of literature data investigating the dependence of the magnitude of the plastic zone around crack tip r_p of dental CoCrMo alloy, this paper deals with the analytical solution to the posed problem.

A thin, infinite plate with an embedded central straight crack of a length 2*a* was modelled analytically in this paper. A plate is uniaxially loaded in a direction perpendicular to the crack plane by monotonously increasing loading $\sigma_{yy}^{\infty} = \sigma_{\infty}$. A crack surface is unloaded. A plate material has the property of isotropic strain hardening (nonlinear strain hardening). A plane stress state is determined by the stress tensor components $\sigma_{xx}(x,y)$, $\sigma_{yy}(x,y)$ and $\sigma_{xy}(x,y)$ is assumed. For an analysis of the elastic-plastic fracture mechanics parameters, it is important to consider the stress tensor components and the displacement vector components of the points lying on a direction of a crack plane, i.e. on the *x*-axis. Since there is symmetry with respect to the *x*-axis, the shear stresses at the points laying on the *x*-axis will be equal to zero, i.e. the normal stresses $\sigma_{xx}(x,0)$ and $\sigma_{yy}(x,0)$ are the principal stresses. Equivalent stress σ_{equ} is determined according to the Tresca or the Mises yield criteria. The equivalent stress is dependent on the equivalent plastic strain $\varepsilon_{equ,p}$. Because a distribution law of equivalent plastic strain $\varepsilon_{equ,p}$ is not known, the distribution law of the cohesive stresses within a yield zone will be also unknown.

There are a great number of different methods, especially numerical, which can be used for determining the magnitude of the plastic zone around the crack tip. The Dugdale strip yield model [2-4] in the yielding zone around the crack tip is used for that purpose here. According to this model, the plastic zone is a narrow strip extending from the crack tip in the direction of the crack plane, as it is shown in Figures 1a and 1b. The Dugdale model considers, instead of a real, physical crack, an equivalent elastic crack of length 2*b*, as it is shown in Figure 1c. Partial areas of this imaginary elastic crack $a \le x \le b$ are subjected to nonlinear cohesive stresses $p(x)$, (Figure 1c).

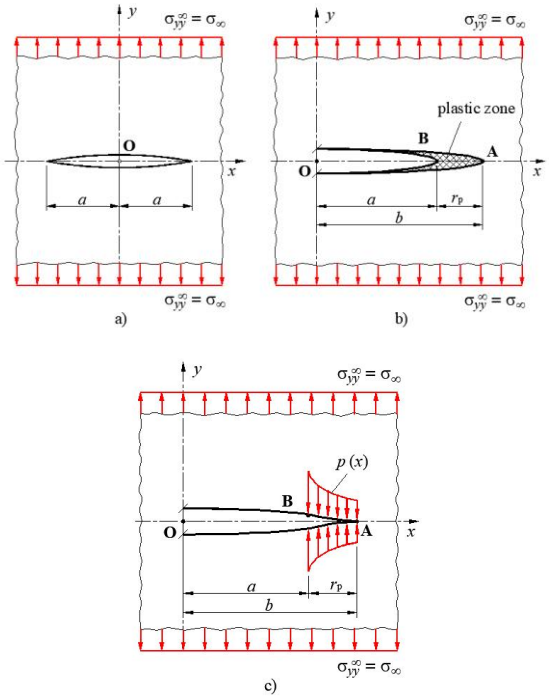

Fig. 1 *a) Thin, infinite plate with the straight crack of a length 2a loaded perpendicular to the crack plane,*
b) fictitious elastic crack including a small plastic zone around crack tip,
c) variable cohesive stresses act on a part of the fictitious elastic crack.

On the edges of plastic zones, or on the tips of an equivalent elastic crack, the normal stress $\sigma_{yy}(b,0)$ will not have singularity but will have a definite quantity equal to the yield stress of the plate material σ_0. In other words, the stress intensity coefficient *K* in these points will be equal to zero, i.e.

$$K(a+r_p) = K_{ext}(a+r_p) + K_{coh}(a+r_p) = 0 \qquad (1)$$

where K_{ext} and K_{coh} are the stress intensity coefficient of external and cohesive loading of the plate, respectively. The singularity at the tip of the fictitious elastic crack $x = b = a + r_p$, from the external load of the plate, is canceled with the singularity of the cohesive stresses within the plastic zone.

2. Mechanical properties of dental CoCrMo alloy

A static tensile test was performed to determine the mechanical properties of the dental CoCrMo alloy of the following chemical composition: 58.9–69.5% Co, 27.0–30% Cr, 5.0–7.0% Mo, with small quantities of Mn, Si, Ni, Fe, <0.05 wt.% C.

Two specimens according to DIN 50 125 - A6×30 shown in Fig. 2 were prepared for the static tensile test.

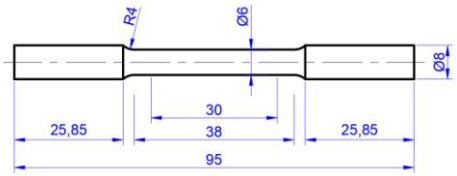

Fig. 2 *Dimensions of the specimen according to DIN 50 125 – A6×30*

Static tensile test was performed on a mechanical test machine Inspekt table 100kN according to DIN EN ISO 6892-1A, which includes the use of an external extensometer (see Fig. 3).

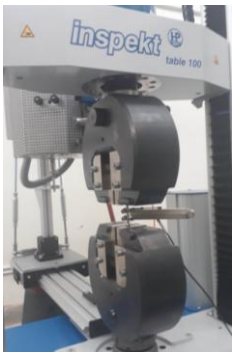

Fig. 3 *Static tensile test conducted with extensometer*

After the static tensile test, the engineering stress-strain dependences (Fig. 4) were obtained and shown in Table 1.

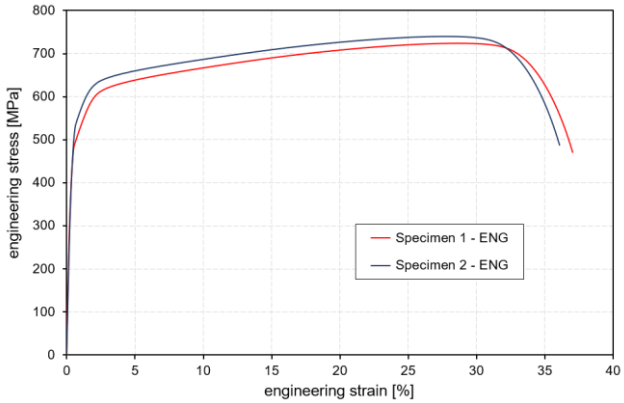

Fig. 4 *Engineering stress-strain diagrams of dental CoCrMo alloy*

Table 1: *Mechanical properties of dental CoCrMo alloy*

Specimen	Modulus of elasticity E [GPa]	0.2% offset yield stress $R_{p0.2}$ [MPa]	Ultimate tensile stress R_m [MPa]	Elongation A [%]
1	127.93	485.48	723.99	37.04
2	119.90	529.08	739.92	36.08

During the plastic deformation, the dental CoCrMo alloy is nonlinearly hardened and the correlation between stress and strain could be found in accordance with the Ramberg-Osgood equation, [5]

$$\frac{\varepsilon}{\varepsilon_0}=\frac{\sigma}{\sigma_0}+\alpha\left(\frac{\sigma}{\sigma_0}\right)^n \tag{2}$$

where σ_0 and ε_0 denote the material's yield stress and strain, respectively, while α and n denote Ramberg-Osgood's material constant and strain hardening parameter, respectively. If it is taken, the Ramberg-Osgood equation takes the form

$$\varepsilon=\frac{\sigma}{E}+\alpha\frac{\sigma_0}{E}\left(\frac{\sigma}{\sigma_0}\right)^n \tag{3}$$

According to Table 1, the dental CoCrMo alloy has a yield stress of 0.2% offset ($R_{p0.2}$). Instead of the yield stress σ_0 in equation (5), the 0.2% offset yield stress $R_{p0.2}$ was introduced. The plastic component of the strain tensor ε_{pl} has an amount of 0.002 for $\sigma=\sigma_0=R_{p0.2}$. Then equation (3) becomes

$$\varepsilon(\sigma=\sigma_0=R_{p0.2})=\frac{\sigma}{E}+\alpha\frac{\sigma_0}{E}=\varepsilon_{el}+0.002 \tag{4}$$

Fitting data in Figure 4 of two samples of dental CoCrMo alloy using a least-squares method, the material parameters of nonlinear Ramberg-Osgood equation (3) were found and shown in Table 2.

Table 2: *Ramberg-Osgood's material parameters of dental CoCrMo alloy*

Specimen	α	n	R^2
1	0.527	13.02	0.976523
2	0.453	15.43	0.978425

The Ramberg-Osgood's material curve of dental CoCrMo alloy was shown with the averaged values of the strain hardening parameter n=14.225 and a comparison with the curves obtained by the static tensile test is shown in Fig. 6.

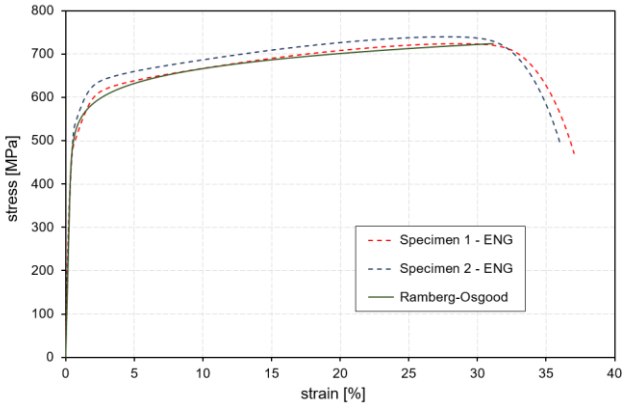

Fig. 4 *Comparison of Ramberg-Osgood's and engineering stress-strain diagrams of dental CoCrMo alloy*

3. Determination of plastic zone magnitude around the crack tip

The best approximation of the nonlinear distribution of the cohesive stresses [2,4] is achieved by the analytical expression

$$p(x)=\sigma_0\left(\frac{r_p}{x-a}\right)^{1/(n+1)} \tag{5}$$

The physical quantity $p(x)$ (see Fig. 1c) is a function of the two parameters, i.e. r_p and n. The stress intensity coefficient K and the magnitude of the plastic zone around a crack tip r_p can be determined by using the method of weight functions (Green's function). The Green's function for an infinite cracked plate, loaded on stretching in a direction perpendicular to the crack plane, according to D. Pustaić [6] amounts

$$m(x,b)=2\sqrt{\frac{b}{\pi}}\left(b^2-x^2\right)^{-1/2} \tag{6}$$

The stress intensity coefficient can be calculated using Green's function [2, 7], knowing the distribution of the cohesive stresses (7), as

$$K_{coh}(b)=\int_a^b p(x)\cdot m(x,b)\,\mathrm{d}x \tag{7}$$

Introducing a new variable ξ, according to [2], the variable x has the form $x = a + r_p(1-\xi) = b - r_p\xi$ ($\xi = 1$ for $x = a$, and $\xi = 0$ for $x = b$), the expression (7) is transformed in the following form

$$p(\xi) = \sigma_0 (1-\xi)^{-1/(n+1)} \tag{8}$$

Inserting the expressions (6) and (8) in (7) and after arranging the following expression is obtained

$$K_{\mathrm{coh}}(b) = \sqrt{\frac{2}{\pi} r_p} \cdot \sigma_0 \int_0^1 \frac{1}{(1-\xi)^{1/(n+1)}} \cdot \frac{1}{\left[\xi\left(1-\frac{r_p}{2b}\xi\right)\right]^{1/2}} \mathrm{d}\xi \tag{9}$$

By forming the above expression the assumption about the small crack tip plastic zone can be introduced. Under small-scale yielding (SSY) conditions it could be taken $r_p / 2b \approx 0$. After integration, the final result for $K_{\mathrm{coh}}(b)$ has the form

$$K_{\mathrm{coh}}(b) = \sqrt{\frac{2}{\pi} r_p} \cdot \sigma_0 \frac{\Gamma\left(\frac{1}{2}\right) \cdot \Gamma\left(\frac{n}{n+1}\right)}{\Gamma\left(\frac{1}{2}+\frac{n}{n+1}\right)} = \sqrt{\frac{2}{\pi} r_p} \cdot \sigma_0 B\left(\frac{1}{2}, \frac{n}{n+1}\right) \tag{10}$$

where $\Gamma(x)$ stands for the gamma function or the Euler's integral of the second type and $B(x, y)$ is the beta function or the Euler's integral of the first type. This result must be taken with the opposite sign because the stress intensity coefficient $K_{\mathrm{coh}}(b)$ takes the negative value if calculations are being conducted for the direction of the cohesive tensile stresses. The stress intensity coefficient, corresponding to a remote tension of a plate with an imaginary crack of length b, amounts to

$$K_{\mathrm{ext}}(a + r_p) = \sigma_\infty \sqrt{\pi (a + r_p)} \,. \tag{11}$$

By equating the right sides of the expressions (10) and (11) and by arranging that equation, the magnitude of plastic zone r_p in front of the crack tip [7], normalized to the initial crack length a, by an assumption of the small plastic zone, is obtained as

$$\frac{r_p}{a} = \frac{\pi}{2}\left(\frac{\sigma_\infty}{\sigma_0}\right)^2 \cdot \frac{\left[\Gamma\left(\frac{1}{2}+\frac{n}{n+1}\right) \Big/ \Gamma\left(\frac{n}{n+1}\right)\right]^2}{1 - \frac{\pi}{2}\left(\frac{\sigma_\infty}{\sigma_0}\right)^2 \cdot \left[\Gamma\left(\frac{1}{2}+\frac{n}{n+1}\right) \Big/ \Gamma\left(\frac{n}{n+1}\right)\right]^2} \tag{12}$$

4. Results and discussion

On the basis of analytical expression (12), the values of plastic zone magnitude r_p in front of the crack tip, normalized to the initial crack length a, are calculated in dependence upon monotonously increasing external load σ_∞/σ_0, for dental CoCrMo alloy. The results were obtained by means of the commercial software package *Mathematica* and presented in the form of diagrams in Fig. 5.

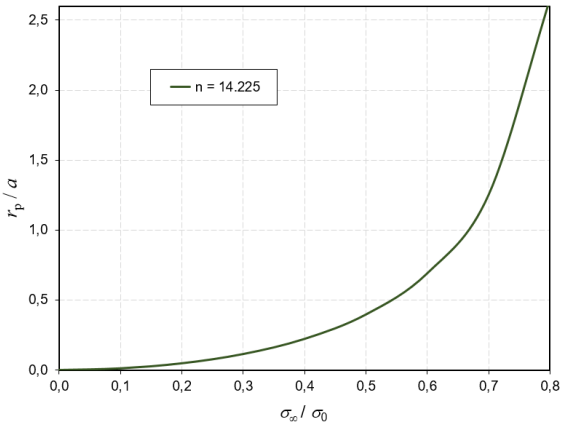

Fig. 5 *Dependence of plastic zone magnitude r_p on load σ_∞/σ_0 of dental CoCrMo alloy*

The results of the magnitude of plastic zone r_p in Fig. 5 are presented as a function of the external load which is normalized to 0.2% offset yield stress (σ_∞/σ_0). This display of results in the non-dimensional form includes only the strain hardening parameter n of the Ramberg-Osgood equation for dental CoCrMo alloy.

From the diagram in Fig. 5, it can be seen that the magnitude of the plastic zone at the crack tip does not increase linearly with the external load of the thin plate. If we assume that the crack is 20 mm (a=10mm), the size of the plastic zone at the crack tip in the direction of the x-axis according to Fig. 1 at an external load of 100MPa (σ_∞/σ_0=0.2) is 0.47mm, while at 200MPa (σ_∞/σ_0=0.4) it is 2.22mm. That's an increase in the magnitude of the plastic zone at the crack tip by 372%. With a higher external load, the magnitude of the plastic zone at the crack tip is larger.

5. Conclusion

The aim of this investigation was to establish if, and, in what measure the isotropic hardening of the dental CoCrMo alloy influences the magnitude of the plastic zone around the crack tip. The goal was to develop the corresponding analytical expressions for calculating the r_p and not to use the numerical methods. One well-known cohesive model for the crack analysis was applied. The non-singularity condition of the stress distribution at the tip of the fictitious elastic crack is noted in the form (1). In this paper, the analytical expression (5) for the distribution of the cohesive stresses is taken. On the basis of analytical expression (12), the values of plastic zone magnitude r_p in front of the crack tip, normalized to the initial crack length a, are calculated in dependence upon monotonously increasing external load σ_∞/σ_0, for dental CoCrMo alloy. The results were obtained by means of the commercial software package *Mathematica* and presented in the form of diagrams in Fig. 5. From the diagram in Fig. 5, it can be seen that the magnitude of the plastic zone at the crack tip increase non-linearly with the external load of the thin plate.

Acknowledgments: Investigations were performed within research project IP-124 University of Zagreb Faculty of Metallurgy, Centre for Foundry Technology—SIMET, KK.01.1.1.02.0020 and VIRTULAB—Integrated laboratory for primary and secondary raw materials, KK.01.1.1.02.0022.

6. References

1. B. Li, A. Mukasyan, A.Varma, Mater. Res. Inovations, **7**, 4 (2003).
2. X.G. Chen, X.R. Wu, M.G Yan, Eng. Fract. Mech., **41**, 6 (1992).
3. M. Hoffman, T. Seeger, Dugdale Solutions for Strain Hardening Materials. The Crack Tip Opening Displacement in Elastic-Plastic Fracture Mechanics. In: Proceedings of the Workshop on the CTOD Methodology, 57-77. Geesthacht, (1985).
4. A. Neimitz, Eng. Fract. Mech., **71**, 11 (2004).
5. P.S. Patwardhan, R.A. Nalavde, D. Kujawski, Procedia Struct. Integrity, 17 (2019).
6. D. Pustaić, M. Lovrenić, Analytical and Numerical Investigation of Crack Opening in Strain-Hardening Material. In: *Proceedings of 5th International Congress of Croatian Society of Mechanics* and CD-ROM, Croatian Society of Mechanics. Croatia, Trogir (2006).
7. D. Pustaić, M. Lovrenić-Jugović, Mathematical Modeling of Cohesive Zone in the Ductile Metallic Materials. In: *Proceedings of the 9th International Congress of Croatian Society of Mechanics*. Croatian Society of Mechanics. Croatia, Split (2018).

Nanomaterials: Properties and Applications in Structural engineering

Elisaveta Doncheva[1], Jelena Djokikj[1]
Ss. Cyril and Methodius University, Faculty of Mechanical Engineering, Skopje, North Macedonia[1]
e-mail: elisaveta.doncheva@mf.edu.mk, jelena.djokikj@mf.edu.mk

Abstract: *Nanotechnology has grown in popularity due to the enormous potential for producing materials and products with diverse properties, allowing significant advancement of existing technology and the development of new innovative technologies. Nanomaterials behave differently at the nanoscale than their conventional counterparts, opening exciting new possibilities in a wide range of construction applications. Nonetheless, the lack of information on nanomaterials' suitability, high costs, and health risks limits their use in construction and structural engineering. As a result, research must be conducted to provide accurate information and facts about the properties and performance of nanomaterials under various load conditions, as well as information on the advantages of using nanomaterials over other construction materials. This paper provides information on nanomaterial properties and how they affect structural materials' microstructure and mechanical properties. It also demonstrates the benefits of using nanotechnology and suggests new possibilities.*
Keywords*: NANOMATERIALS, NANOPARTICLES, PROPERTIES, CONSTRUCTION, COATING*

1. Introduction

The rapid development of nanoscience and nanotechnology in recent years is due to nanomaterials' enormous potential in terms of material and product production. The primary distinction between nanoscience and nanotechnology is that nanoscience provides knowledge of the fundamental properties and arrangements of atoms, whereas nanotechnology uses matter to create new materials with advanced properties [1]. Nanotechnology is the understanding, fabrication, and application of small-scale structures and materials (nanostructures and nanoparticles). It is gaining popularity in almost all engineering branches because it is regarded as an interdisciplinary advanced technology that creates nanomaterials composed of ultra-small particles with properties and behaviors distinct from the larger building blocks of the substances [1],[2]. The independence of electrostatic and quantum forces from gravity at the nanoscale suggests new effects on properties, making nanotechnology more powerful than the traditional practice of manipulating materials on a macro-scale [3]. When obtaining nanoparticles from one matter, surface atoms are much more likely to improve the material's properties than those in the interior [4]. The new properties result from the fact that a small particle has a limited number of molecules and thus interacts differently with the surrounding area [2].

Nanomaterials have at least one nanoscale dimension, and depending on the number of nanoscale dimensions, they can be classified as zero, one, two, or three-dimensional. They are classified based on their morphology (spherical, flat, needle, or random orientations with various shapes such as quantum dots, nanowires, nanotubes, nanofluids, nanobelts, nanosheets, nano-springs, nano-capsules) and composition (monometallic, bimetallic, trimetallic, metal oxide, magnetic, hybrid) [5]. According to their design, nanomaterials can be classified as carbon-based, metal-based, dendrimers, and composites [2]. They can occur naturally as a byproduct of biological systems, accidentally as a byproduct of an industrial process, or deliberately manufactured through some engineering process to obtain materials with specific properties [6].

The use of nanomaterials is appropriate for technological advancement because modifications to the shape, size and internal order of the nanostructures can improve a variety of chemical and physical properties such as melting point, conductivity, absorption, and light dispersion [2]. It's already utilized in numerous engineering disciplines and research areas, but there are still possibilities that are yet to be discovered for further developments. Fig. 1 depicts the interests and role of nanoscience and nanotechnology in science and engineering [1].

Although public awareness of the advantages of using nanotechnology in structural engineering has grown in recent years, there is still a scarcity of information on the subject. This article outlines the most recent achievements in structural engineering of nanotechnology, with an emphasis on properties, the benefits of their application, and their potential for further development and use in construction.

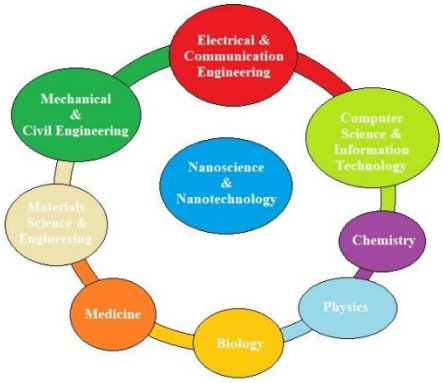

Fig. 1 *Nanotechnology and nanoscience in relation to other sciences and engineering disciplines [1]*

2. Application and properties of nanomaterials in structural engineering

The development of new concepts and understanding of the use of nanoparticles in construction materials is important in structural engineering. Materials can be made stronger, more durable, and tougher using nanotechnology. Furthermore, self-cleaning, insulating, and water resistance properties can be introduced to new structures on their glass surfaces or applied by paint, making these buildings modern and self-sustaining. These materials are used to create stronger and lighter structural composites, low-maintenance coatings, water repellents, UV light protection, and nano-sensors for structural health monitoring [4].

Carbon nanotubes (CNT) are the most commonly used nanomaterials in construction, used for concrete strengthening and monitoring. These nanotubes are made up of graphene-embedded sheets that are rolled into tubes [1]. CNTs are classified into two types: single-wall CNTs and multi-wall CNTs. The single-walled (SW) CNT is made up of one cylindrical shape with various atom arrangements, whereas the multi-walled (MW) CNT is made up of two or more cylindrical shapes packed layer by layer, as shown in Fig.2 [8]. They have significantly higher mechanical properties than steel, such as young's modulus and strength, as well as exceptionally high thermal conductivity along their axis. These carbon-based nanomaterials have good electrical properties and have a growing potential for smart materials and self-monitoring structures [7]. Nanotubes are used in concrete to increase strength and durability, as well as to prevent cracks. They are used in ceramics to improve mechanical and thermal properties, as well as in structures for health assessments [4]. Fullerenes, which have a hollow cage structure of particles with sixty or more carbon atoms and exhibit good electrical conductivity, electron affinity, and high strength [1], are another carbon-based nanomaterial. Carbon

nanomaterials may also be used in automobiles as batteries, engine oils, self-lubricating materials, nano-lubricants, and coatings to improve surface wear and antifriction [5]. The molecular structure of carbon can be changed using nanotechnology to a spherical geodesic form, making it more fluid, resulting in the development of nanotubes with an extremely high elastic modulus of 1 TPa, yield strength of 60 GPa, and yield strain of the order of 6% [8]. The CNT can be used to reinforce polymers, glass, composites, and metals in addition to ceramics and cement-based matrix. Materials with a great deal of potential for use in structural engineering include cutting tools, springs, wear-resistant, impact, and earthquake-resistant structures, ductile cement, and glass. In cementitious composites, graphene oxide and graphene nanoparticles are used to enhance the material's mechanical qualities. They are somewhat investigated for application in reinforcing cement composites due to their exceptional elastic characteristics and tensile strength. The structure of graphene and graphene oxide is depicted in Fig.3 [8].

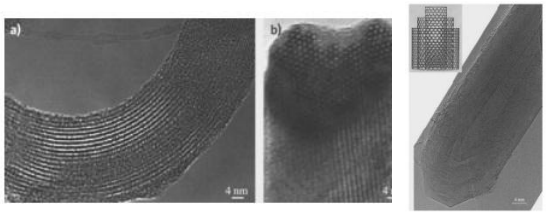

Fig. 2 *Images made of high-resolution transmission electron microscope: a) SWCNT rope – longitudinal view, b) SWCNT rope – cross-sectional view, c) MWCNT with a representation of the layers in the left top corner [8]*

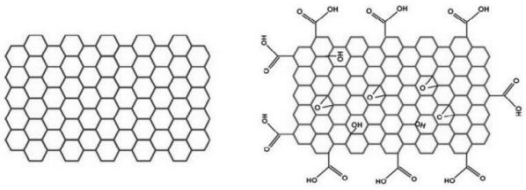

Fig. 3 *Structure of graphene (left) and graphene oxide (right)[8]*

Metal nanoparticles, also known as quantum dots, monometallic oxides (zinc oxide, titanium dioxide, iron oxide), nano-gold, and nano-silver can be used to create nanomaterials [2]. Metal nanoparticles with a high surface area and good absorption of small molecules are formed by reducing divalent and trivalent metal ions with agents [1]. Titanium dioxide (TiO2) is a two nano-sized particle used as a white pigment in paints, cement, windows, and tiles for sterilizing, deodorizing, and anti-fouling properties, and it reduces airborne pollutants through a photocatalytic process. When exposed to UV light, it becomes water-repellent and can be used for anti-fogging or self-cleaning. Furthermore, TiO_2 nanoparticles can be used in concrete as a partial replacement for cement because they increase compressive, flexural, durability, and split tensile strength [10]. Similarly, Fe_2O_3 and CuO nanoparticles are used to improve the mechanical properties of cement and concrete, but they can reduce setting time, workability, and mechanical properties by 3–4%. For denser cement with improved porosity, nanoparticles of silicious dioxide SiO_2 (nano-silica) are used in cement composites. Al_2O_3 nanoparticle use offers comparable advantages when added in small amounts to cement and concrete with an average particle size of 15 nm or less, but it also reduces workability and setting time due to the nanoparticles' quick reactivity with $Ca(OH)_2$ [10]. With the addition of ZrO_2, the concrete's compressive, flexural, and tensile strength can also be increased. However, because of the quick reaction between ZrO_2 and calcium hydroxide, this also affects the workability and setting time, hence superplasticizer is recommended [10]. Nano ZnO_2 particles can help concrete's pore structure and its recovery from polycarboxylate's harmful impacts. The application of CaO_3 nanoparticles provides enhancing characteristics of cement and concrete and increases hydration, setting time, and compressive properties. The silver nanoparticles are used in paints for antibacterial properties on surfaces, this is usually applied to the walls of hospitals to lower the growth of infectious viruses and bacteria [10]. There are also bimetallic nanoparticles (Fe/Pd, Fe/Ag, or Zn/Pd), they can serve as catalysts and reductants [9]. Semiconductor nanomaterials contain metallic and nonmetallic properties. They are used in photocatalysts, electron devices, solar cells, nanoscale electronic devices, light-emitting nanodevices, laser technology, waveguide, chemicals, and biosensors. This type of nanomaterials are made of different compounds and are referred to as II-VI, III-V or IV-VI semiconductor nanocrystals [1]. They have interesting attractive physical and chemical properties, narrow and intensive emission spectra, continuous absorption bands, high chemical and photobleaching stability, processability, and surface functionality [11]. These nanomaterials are advanced materials intended for various applications like new emerging technologies, nanoelectronics, nanophotonic, energy conservation, non-linear optics, miniaturized sensors and imaging devices, solar cells, detectors, and biomedicine [12].

There has been significant progress in exploring a wide range of materials such as nanocomposites and nanohybrids [2]. Nanocomposites are materials with more than one phase where one of the phases has at least one dimension that is less than 100nm, whereas nanohybrids are a combination of 2 or more nanomaterials for satisfying a different function. Compared to the traditional composites, these materials have a high surface volume ratio, and based on their size, shape, or properties they can be different types like ceramic matrix nanocomposites, metal matrix, and polymer matrix nanocomposites [1]. Nano-clay particles are already being added to different products from auto parts to packaging materials as reinforcement in high-performance composites. Nanocomposites with incorporated nanotubes are popular because nanotubes show outstanding properties that in the composite mixture improve the overall properties of the materials. For example, alumino-silicates and nanotubes mixture produces strong and durable films and by further reducing the size of alumino-silicates to 5 to 10 nm more advancement in properties can be achieved [11]. Wrapping existing concrete structures with a fiber sheet matrix of nano-silica show excellent results for strengthening [11].

Steel is extensively used as a construction material in structures that are subjected to cycling loading which can lead to fatigue failure. It is a durable material that holds a high-strength-to-weight ratio in comparison to other construction materials. By adding copper nanoparticles, the surface unevenness can be reduced, and this will limit the stress concentrations and lower fatigue crack initiation [12]. Vanadium and molybdenum nanoparticles can lower fractures in bolts. Stronger steel can be produced by adding nanoparticles in paints and coatings when used as reinforcement bars in concrete [13]. These are known as micro-composite multi-structural formable (MMFX) that are corrosion resistant and have durable properties. The effect of hydrogen embrittlement and their inter-granular cementite phase are reduced through the improvement of steel microstructure [13]. With nanoparticles, steel can become corrosion resistant which is a challenging matter with the traditionally used steel and by adding nanoparticles like calcium and magnesium finer grains in the microstructure of the weld and heat-affected zone can be achieved [14]. Nanotechnology in the metallurgy of steel is used for the reduction of ural steel where microalloying steel with nitride phases is combined with plastic-deformation nanotechnology make the steel stronger [14]. Table 1 contains information on the application of nanoparticles added to traditional materials and summarizes the benefits of their use.

Table 1: *Summarized data on nanomaterials used in traditional construction materials for enhanced properties*

Category	Nanomaterial		Application/Base material	Nanoparticle
Carbon-based nanomaterials	Carbon Nanotube		Cement/Concrete	Improved durability, compressive and flexural strength, self-sensing, and self-cleaning properties,
			Ceramics	Enhancement in thermal and mechanical properties, reduced shrinkage, antibacterial
			Nano electrical mechanical systems	Real-time health assessment of structures
			Solar cell	Effective electron mediation
	Graphene and graphene oxide		Cement/Concrete	improved microstructure, mechanical properties, and durability. improved microstructure, mechanical properties, low cost, accelerated hydration, enhanced corrosion resistance
\Metal- based nanomaterial Metal- based nanomaterial	Semiconductor	Silicon dioxide	Cement and concrete	Enhancement in mechanical strengths and durability, denser cement paste, improved porosity, corrosion reduction, insulating properties
			Glass	Enhancement in mechanical Strengths and durability, nonreflective, fire and heat protection, easy-to-clean properties
			Coatings	Antibacterial, photocatalytic, self-cleaning, hydrophobic, scratch resistance, fire retardant
			Ceramics	Coolant; light transmission; fire resistant
		Titanium dioxide	Solar cell	Producing non-utility power
			Glass	Antifogging, hydrophilicity, fouling resistance, IR reflection, photocatalytic self-cleaning
			Cement and concrete	Self-cleaning, rapid hydration and improvement in mechanical strengths, increased flexibility, pore structure improvement, improved performance at elevated temperatures
			Coatings/Paints	Antibacterial, photocatalytic, self-cleaning, hydrophobic properties, UV protection on wood, active air pollution reduction on asphalt, road pavement blocks, sound barriers, and tunnels
			Solar cell	Non-utility electricity generation
		Ferric oxide	Cement and concrete	Improvement in strength, durability, compression, and abrasion resistance, hydration of cement is increased
		Copper oxide	Cement and concrete	Improved mechanical strengths and durability, reduced the porosity
			Steel	Improved weldability, formability, and corrosion resistance
		Calcium carbonate	Cement and concrete	Improve rheological properties of concrete, increased rate of hydration, setting time, and improve compressive strength
		Chromium Oxide	Cement and concrete	Improves properties of concrete, higher mechanical strength, and durability properties
		Aluminium oxide	Cement and concrete	Compacted microstructure, decreased porosity, enhanced compressive strength, frost resistance, accelerated hydration, reduced water absorption
			Coatings	Scratch resistance
		Zirconium oxide	Cement and concrete	Enhancement in mechanical strengths
		Zinc dioxide	Cement and concrete	Advancement in mechanical strengths, antibacterial properties
			Coatings/Paints	Antimicrobial activity, UV protection
		Silver (Ag)	Paints	Antimicrobial properties, reduce the growth and multiplication of fungi, viruses and bacteria

3. Conclusion

The interest in nanomaterials and their application is constantly growing in many industries. It opens a variety of new possibilities in structural engineering for implementing novel innovative technologies and solutions through improving the properties of the available traditional materials and obtaining and with that obtaining a wider spectrum of new materials. The basic properties of the materials on the nanoscale level bring up significant changes in the mechanical, physical, and thermal properties. The research and applications of nanomaterials are mainly focused on the understanding of the nanostructure of materials and their modification, functional films and coatings, smart structures and devices, and their effect on the environment and health [5]. In structural engineering, there are carbon-based, metal-based nanomaterials, semiconductors, dendrites, nanocomposites, and nanohybrids that can improve the construction materials and bring them completely new capabilities. Table 1 summarizes all of the benefits that nanoparticles bring to materials like cement, concrete, glass, coatings, composites, and steel. It is evident that nano-alumina, nano-titania, nano-silica, nano-magnesium oxide, nano-zinc oxide, silver nanoparticles, carbon nanotubes, or graphene derivatives may have enhanced hydration, microstructure, porosity, and thus mechanical properties and transport-related properties of cementitious composites and introduce new properties such as self-cleaning, self -sensing and antimicrobial properties. There are most recent advancements in applications of nanomaterials in cement composites and structural health monitoring, but the industrial-scale application and toxicity remain a challenge for further development of nanomaterials. Also, lowering the already high energy consumption in buildings and structures is the possible direction of future investigations. A broader perspective should be considered when investigating the possibilities of nanomaterials for enhancing sustainability. Improving the properties of materials, and conserving energy and toxicity are important and should be a high priority for further investigations. Advanced analytical techniques are required for the detection and characterization of nanomaterials realization or incorporation in construction materials [8]. This paper presents a review of the achievements in structural engineering with an emphasis on properties and applications. Further investigation should be done on the sustainability possibilities of incorporating nanotechnology in the construction industry.

References

[1] L. A. Kolahalam, I.V. K. Viswanath, B. S. Diwakar, B. Govindh, V. Reddy, Y.L.N. Murthy, Review on nanomaterials: Synthesis and applications, in: Materials Today: Proceedings, Vol. 18, 6, 2182-2190 (2019)

[2] A. Bratovcic, Different Applications of Nanomaterials and Their Impact on the Environment, SSRG International Journal of Material Science and Engineering, Vol. 5, 1, 1-7, (2019)

[3] A.Srivastava, K. Singh, Nanotechnology in civil engineering and construction: a review on the state of the art and future prospects, Proceedings of Indian Geotechnical Conference, 1(024), 1077-1080, (2011)

[4]F.Trotta, A.Mele, Nanosponges: Synthesis and applications, Chapter 1 Nanomaterials: Classification and properties, 1- 26, (2019)

[5] K. RB Singh, P. R. Solanki, B.D. Malhotra, A. C. Pandey, R. P. Singh, "Introduction to Nanomaterials: An Overview toward Broad-Spectrum Applications", In: Nanomaterials in Bionanotechnology: Fundamentals and Applications, Chapter: 1, Publisher: CRC Press (2021)

[6] M.N.O. Sadiku, Y.P. Akhare, A. Ajayi-Majebi, S.M.Musa, Nanomaterials: A Primer, IJASRE, Vol. 7, 3, 1-6, (2021)

[7] M. Krystek, and M. Górski, "Nanomaterials in Structural Engineering", in New Uses of Micro and Nanomaterials, London, United Kingdom: IntechOpen, (2018) [Online].

[8] H.V. Tien, G. Ngoc Ha, V. P. Phuong Trang, V. Bao Khanh, Nanomaterials in construction: an overview, Tạp chí Khoa học công nghệ và Thực phẩm **15** (1), 34-45, (2018)

[9] W. Zhu, P.J.M. Bartos and A. Porro, Application of nanotechnology in construction: Summary of a state-of-the-art report, Materials and Structures / Matériaux et Constructions, Vol. **37**, 649-658, (2004)

[10] M. Daniyal, A. Azam and Sabih Akhtar, Application of Nanomaterials in Civil Engineering, Chapter 6, 169-189 (2018)

[11] S. Suresh, Semiconductor Nanomaterials, Methods, and Applications: A Review, Nanoscience and Nanotechnology 3(3), 62-74, (2013)

[12] A. A. Firoozi, M. R. Taha, Ali Asghar Firoozi, Nanotechnology in Civil Engineering, EJGE, Vol. 19 4674 -4682 (2014)

[13] A. Mohajerani, L. Burnett, J. V. Smith, H. Kurmus, J. Milas, A. Arulrajah, S. Horpibulsuk and A. A. Kadir, Nanoparticles in Construction Materials and Other Applications, and Implications of Nanoparticle Use, Materials **12**, 3052 (2019)

[14] A.A.Ali, Nanotechnology in Civil Engineering Construction, International Journal of Structural and Civil Engineering Research, Vol. **9**, No. 1 (2020)

Features of the tribological behavior of the magnesium alloy Mg -1% ca depending on the structural state

Vladimir I. Semenov [a+], Hsin-Chih Lin [b], Sergey V. Chertovskikh [a], Olga B. Kulyasova [a, c]

[a] Ufa State Aviation Technical University,
12 K. Marx St., Ufa 450008, Russia.
[b] National Taiwan University
1, Roosevelt Road, Sec. 4, Taipei 106, Taiwan R.O.C.
[c] Bashkir State University,
32 Zaki Validi St., Ufa 450076, Russia
[+]corresponding author, e-mail: semenov-vi@rambler.ru

Abstract: *This paper presents experimental data on the tribological properties of the Mg-1%Ca magnesium alloy with different microstructures (coarse-grained microstructure in the initial state, and ultrafine-grained and nanocrystaline microstructures after severe plastic deformation via two processes – equal-channel angular pressing and high pressure torsion) in contact with an indenter made of the Fe-18W-4Cr-0.8C steel without any coating and with applied hydroxyapatite, which is the main mineral component of bones. An indenter with hydroxyapatite on the surface was used as a bone simulator. As a result of the experiments, it was found that the shear strength of adhesive bonds and the adhesive component of the friction coefficient are structurally sensitive parameters. For all the samples in the considered contact pairs, when using a bone tissue simulator the strength of adhesive bonds was lower than that when using a steel indenter. It is noted that ultrafine-grained and nanocrystalline structures produced as a result of severe plastic deformation via two processes, equal-channel angular pressing and high pressure torsion, contribute to a decrease in the shear strength of adhesive bonds and the adhesive component of the friction coefficient due to strengthening resulting from grain size reduction from originally 100 μm to 1.4–4 μm on average in the investigated Mg-Ca magnesium alloy.*

KEYWORDS: *STRENGTH OF ADHESIVE BONDS, ADHESIVE COMPONENT OF THE FRICTION COEFFICIENT, SEVERE PLASTIC DEFORMATION, HYDROXYAPATITE.*

1. INTRODUCTION

In [1, 2], a brief review of modern scientific literature on the main achievements and problems of biomedical magnesium alloys for traumatology and orthopedics is presented. Great interest in these materials is due to the fact that magnesium alloys are highly biocompatible, bioinert, hypoallergenic and, moreover, non-toxic [3, 4]. The disadvantage of magnesium alloys with a coarse-grained (CG) structure is its low strength. To increase the strength and functional properties of Mg alloys, rather widely used is alloying with different elements [5–8]. Such a method for increasing strength is quite efficient, but is not always acceptable for materials intended for the use in medical implants due to the possible adverse effects of some alloying elements on the human body.

According to expert evaluation, it is promising to use Mg-Ca magnesium alloys in medical implants for osteosynthesis [9], since both of these chemical elements are present in bone tissue and have a beneficial effect on the body. It has been found that the presence of Ca in a Mg alloy normally reduces its strength and ductility at room temperature. As noted in [10], the effect of Ca is not so unambiguous. Although the offset yield strength increases from 30–35 MPa for pure Mg to about 95 MPa for the Mg-0.9 Ca alloy, elongation decreases from 10–12% to 2–3%, respectively.

The applied technologies of deformation treatment make it possible to achieve a high-strength state due to the formation of an ultrafine-grained (UFG) and nanocrystalline (NC) microstructure, which contributes to an increase in mechanical and functional properties [11]. Severe plastic deformation (SPD) methods, in particular, equal-channel angular pressing (ECAP) and high pressure torsion (HPT) [12, 13, etc.] due to the formation of UFG and NC structures, enable increasing the strength of alloys by 20-60% while preserving a rather high ductility (about 8–10%).

Currently, magnesium alloys are used as load-bearing implants, such as plates, screws and pins, to repair bone fractures. Degradable coronary stents are an important area of research. Degradable vascular stents contribute to the stable regeneration of vessels, in contrast to permanent stents [14].

It is known that in many conjugations that are in a mobile or static contact, the tribological [15, etc.] and adhesive [16, 17] interactions of surfaces play an important role and are among the main functional properties in implantology during osteosynthesis. In this case, the adhesive interaction can activate the processes of corrosion and dissolution of protective films and coatings. The authors plan further research in this area in the future.

A number of papers [18-20, etc.] are devoted to the problem of evaluating the shear strength of adhesive bonds. However, the presented papers lack practically any analysis into the effect of microstructure on the tribological properties of a Mg-Ca magnesium alloy contacting bone tissue, where one of the main components in hydroxyapatite. Besides, it is known than bones serve as a magnesium depot in the body [21], which is of practical interest in terms of the contact interaction between Mg-containing implants and bone tissue.

It follows from the given analysis that the issues of adhesive interaction between implants made of a Mg-Ca magnesium alloy with different microstructures and bone tissue have not yet been sufficiently studied. At the same time, these issues are important for understanding various phenomena related to the bioresorption time (speed) of these materials and call for further study [14].

Thus, the aim of this paper is a comparative evaluation of the adhesive interaction with a Mg-Ca magnesium alloy having different microstructures (coarse-grained one in the initial state after casting, preliminary extrusion and annealing, and UFG/NC one after SPD processing) in the contact pairs “magnesium alloy – steel” and “magnesium alloy – bone tissue” to reveal the potential of the deformation treatment of the material under study.

A contribution to solving this set task is of scientific and practical interest. The novelty of the proposed tribological studies with the evaluation of the strength of adhesive bonds is that it is practically the first time such studies are conducted for a Mg-Ca magnesium alloy, and that they may be used when designing processes for the production of next-generation medical implants.

2. RESEARCH METHODS AND MATERIALS

As the material for the study, we used the low-alloyed, specially manufactured in a laboratory, Mg-1%Ca magnesium alloy with a coarse-grained (CG) structure after casting and preliminary extrusion, with UFG/NC microstructures after SPD processing by ECAP and HPT. The microhardness of the samples in the initial as-extruded condition was 53.3 ± 3 HV, after ECAP processing – 71,1 ± 4 HV, and after HPT processing – 98 ± 5 HV. The roughness of the contact surfaces, *Ra*, was about 1.6.

For the tribological studies aimed at finding the shear strength of adhesive bonds and the adhesive component of the friction coefficient, a single-ball adhesion tester was used. The test principle is shown in Fig. 1.

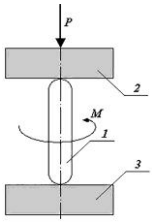

Fig. 1. Principle of the test to find the shear strength of adhesive bonds and the molecular component of the friction coefficient: 1 is a spherical indenter; 2 and 3 are test samples

The presented principle was used to evaluate the shear strength of adhesive bonds and the adhesive component of the friction coefficient. The test samples were in the form of disks with a diameter of 25 mm and a thickness of 5 mm. The spherical indenter with a sphere radius of 2.5 mm was made of the Fe-18W-4Cr-0.8C high-speed steel. The normal load was 1500 N.

The tests were carried out at room temperature (25°C) according to the method described in [22]. This method is based on a physical model which in the first approximation reflects the real conditions of friction at a local contact.

According to this model, the spherical indenter 1, compressed by two plane-parallel samples 2 and 3, rotates under a load around its own axis. The force F spent on the rotation of the indenter is mainly related to the shear strength of adhesive bonds, τ_n.

The shear strength of adhesive bonds, τ_n (MPa), was determined from the ratio:

$$\tau_n = 0.75 \cdot \frac{M}{\pi \cdot \left(\frac{d_{1,2}}{2}\right)^3}, \quad (1)$$

where $d_{1,2}$ are the diameters of imprints on the test samples, mm; *M* is the indenter's torque, *N mm*.

The adhesive (molecular) component of the friction coefficient was determined from formula (2) as the relation of the strength of adhesive bonds to normal pressure:

$$f_M = \frac{\tau_n}{p_r}, \quad (2)$$

where p_r *is* normal pressure, *MPa*,

$$p_r = \frac{P}{\pi \cdot \left(\frac{d_{1,2}}{2}\right)^2} \quad (3)$$

where *P* is the compressive force of the samples, *N*.

The contact surfaces of the indenter and the samples in different structural states were prepared for the comparative tribological tests in the following manner: in the first case – in a clean form (after degreasing) and in the second case – with an applied hydroxyapatite (HA) suspension. HA was used as a material imitating bone tissue. The suspension was applied onto the contact surfaces of the indenter 1 and the test samples 2 (Fig. 1).

As noted above, the test samples had CG and UFG/NC microstructures produced, in the first case, as a result of casting, extrusion and annealing at 250 °C for 1.5 hours, and in the second case, as a result of SPD processing by ECAP and HPT. The principles of the SPD processes are shown in Fig. 2.

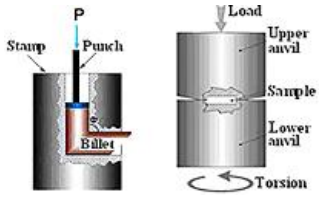

a *b*

Fig. 2. Equipment and die-set for SPD processing: *a* –ECAP processing; *b* – HPT processing

ECAP processing for 8 cycles (Fig. 2 *a*) was performed via route Bc route with 90° rotation around the longitudinal axis of the billet after each processing cycle. The cross-member speed was 6 mm/s. The channels intersection angle was 120°. 4 cycles were performed at a temperature of 250 °C and the following 4 cycles – at a temperature of 230 °C.

HPT processing (Fig. 2 *b*) was performed at room temperature under a normal pressure of 6 GPa at a speed of 1 rpm with a total number of revolutions of 10. The samples for HPT were in the form of disks with a diameter of 20 mm and a thickness of 1 mm.

Metallographic studies were carried out using an Olympus GX51 optical microscope, a JEM-6390 scanning electron microscope (SEM), and a JEM-2100 transmission electron microscope (TEM) with accelerating voltages of 10 kV and 200 kV.

3. RESULTS OF METALLOGRAPHIC STUDIES

Fig. 3 shows an image of the microstructure of the Mg-1%Ca alloy after extrusion. The intermetallic compound Mg2Ca separated during extrusion into small particles which became uniformly distributed. Based on this observation, it can be stated that the presence of small particles in grain interiors will lead to a significant increase in the mechanical properties of the Mg-1%Ca alloy [23, 24].

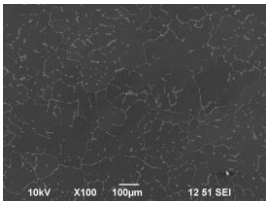

Fig. 3. SEM image of the Mg-1%Ca alloy after extrusion

In order to produce bulk billets, the ECAP method was applied to the extruded samples. A typical view of the samples after ECAP processing is shown in Fig. 4 *a*.

After ECAP processing, the alloy contains Mg_2Ca particles with a size of 2-3 µm, arranged in lines (Fig. 4 *b*). Microstructural studies of the Mg-1%Ca alloy samples after ECAP processing revealed an average α-Mg grain size of 4 µm and the presence of particles of the Mg_2Ca second phase with a volume fraction of 3% (Fig. 4 *b*, *c*). Study by TEM revealed a high density of dislocations (Fig. 4 *d*, *e*) and the presence of twins in the structure, 500 nm in width and up to several microns in length (Fig. 4 *d*).

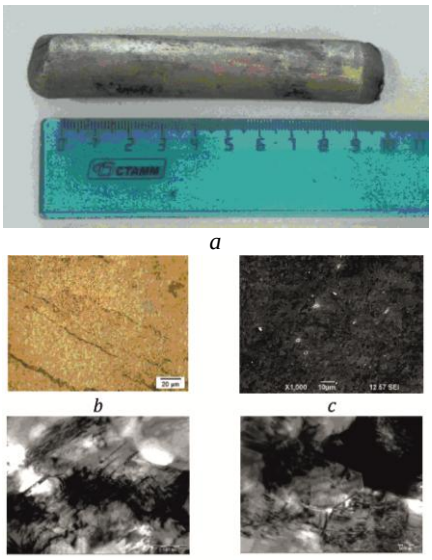

a *b* *c* *d* *e*

Fig. 4. View of a billet and the microstructure of the Mg-1%Ca alloy after ECAP: *a* – view of the sample after ECAP; *b* – Mg_2Ca particles with a size of 2-3 μm, arranged in lines; *c* – particles of the Mg_2Ca second phase; *d* – twins in the structure; *e* – dislocations.

Study by SEM of the structure of the samples after HPT processing and additional annealing at 250 °C revealed the presence in the structure of particles and eutectics with a total volume fraction of 4.0% (Fig. 5 *a*). According to the SEM images, the average grain size is 1.4 μm.

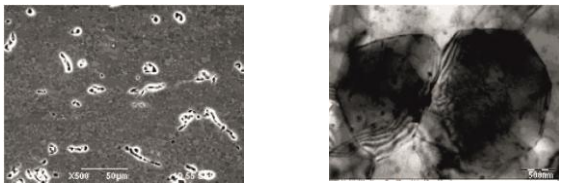

a *b*

Fig. 5. Microstructure after HPT (*a*) and additional annealing at 250 °C (*b*).

The structure contains particles that obviously formed during the decomposition of the supersaturated solid solution formed in the process of HPT (Fig. 5 *b*).

4. RESULTS OF TRIBOLOGICAL TESTS

Fig. 6 shows the imprints of the indenter on the surface of the test material, obtained during tribological tests to determine the shear strength of adhesive bonds and the adhesive component of the friction coefficient. Samples of the magnesium alloy had different microstructures and differently treated contact surfaces.

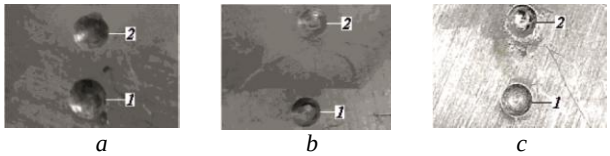

a *b* *c*

Fig. 6. Imprints of the indenter on the surface of the test samples: *a* – the initial state of the test material with a CG structure; *b* – sample after ECAP with a UFG structure; *c* – sample after HPT with UFG and NC structures. Index 1 corresponds to the degreased contact surface, index 2 – to HA applied onto the contact surface. 10x magnification.

As it can be seen in Fig. 6 *a*, the imprints of the indenter on the surface of the material in the initial (coarse-grained) state are somewhat larger in comparison to those in the SPD-processed material (Fig. 6 *b*, *c*). This indicates the lower strength of the material with a coarse-grained structure. As noted in [25-27], SPD processing leads to the formation of a structural and phase state that ensures a higher strength. In this case, there are two mechanisms responsible for a higher strength after SPD processing, namely grain-boundary strengthening, since the length of grain boundaries is larger at a smaller mean grain size, precipitation hardening expressed in dispersed particles of the second phase, as well as strengthening due to the accumulation of a high dislocation density. In addition, it was noted that the diameters of the indentation cups practically do not depend on the presence or absence of hydroxyapatite on the contact surfaces of the investigated triboconjugations. In this case, this speaks of the decisive role of the rheological properties of the investigated material itself – the Mg-1%Ca magnesium alloy.

The results from finding the shear strength of adhesive bonds in the friction pairs "Mg-1%Ca magnesium alloy – *Fe-18W-4Cr-0.8C* high-speed steel" in a clean form after degreasing and with HA applied onto the contact surfaces of the indenter and the test samples are shown in Fig. 7.

In order to increase the reliability of the test results, during the tribological studies three duplicating tests (loading of the test samples with an indenter) were performed, measuring the imprint diameters and averaging the measurement results with a subsequent statistical processing of the values of the shear strength of adhesive bonds [28]. The diagrams shown in Fig. 7 correspond with 95% probability to the 5% confidence interval of significant values, which enabled approximating the obtained values as direct lines.

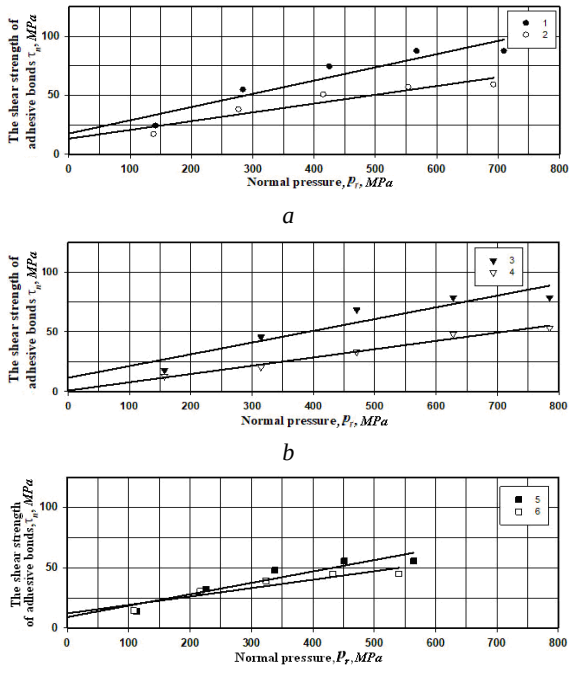

a *b* *c*

Fig. 7. Dependence of the shear strength of adhesive bonds on the normal stress at the contact:
a – 1 – the initial state of the tested material with a CG structure, the contact surfaces are degreased; 2 – the initial state of the tested material with a CG structure, HA is applied onto the contact surfaces;
b – 3 – samples after ECAP with a UFG structure, contact surfaces are degreased; 4 – samples after ECAP with a UFG structure, HA is applied onto the contact surfaces;
c – 5 – samples after HPT with UFG and NC structures, contact surfaces are degreased;
6 – samples after HPT with UFG and NC structures, HA is applied onto the contact surfaces.

As it can be seen from the dependencies presented in Fig. 7 (*a*, *b*, *c*), the values of the shear strength of adhesive bonds and the adhesive component of the friction coefficient, under the experimental conditions, tend to decrease with increasing strength of the Mg-1%Ca magnesium alloy, evidently due to grain size reduction after the deformation treatment [12, 13] and the presence of a bone tissue simulator in the form of hydroxyapatite suspension on the contact surfaces. At the same time, analyzing the tribological behavior of each pair of test samples with the same structure, but in the presence and absence of hydroxyapatite in the triboconjugation, it was noted that, within the experiment error, the load-bearing capacity remains practically constant. This is visibly illustrated in Fig. 7 by the length of the branch of each presented diagram. For example, in diagrams (*a* - 1 and 2), (*b* - 3 and 4), (*c* - 5 and 6) in each of the examined tribological pairs the branch length varies insignificantly. This may indicate that the load-bearing capacity of the investigated material (Mg-1%Ca) depends primarily on the rheological properties of the investigated material, which in their turn are determined by microstructure.

Table 1 shows the complete results of the tribological tests to determine the shear strength of adhesive bonds and the adhesive component of the friction coefficient.

Table 1. Results of tribological tests.

Material (line number in Fig. 7)	p_{rn}, **MPa**	τ_n, **MPa**	τ_n/p_r	β^*	τ_0^*, **MPa**
Mg - 1% Ca in the initial state, Fe-18W-4Cr-0.8C indenter (contact surfaces are degreased) **(1)**	710	97.2	0.14	0.11	17.6
Mg - 1% Ca in the initial state, Fe-18W-4Cr-0.8C indenter (HA on the contact surfaces) **(2)**	693	73.4	0.11	0.07	13.2
Mg - 1% Ca after ECAP, Fe-18W-4Cr-0.8C indenter (contact surfaces are degreased) **(3)**	785	88.7	0.11	0.1	11.4
Mg - 1% Ca after ECAP, Fe-18W-4Cr-0.8C indenter (HA on the contact surfaces) **(4)**	785	55.2	0.07	0.07	0.7
Mg - 1% Ca after HPT, Fe-18W-4Cr-0.8C indenter (contact surfaces are degreased) **(5)**	564	62.4	0.11	0.1	9.1
Mg - 1% Ca after HPT, Fe-18W-4Cr-0.8C indenter (HA on the contact surfaces) **(6)**	540	49.9	0.09	0.07	12.2

β^* is the strengthening coefficient of molecular bonds under compressive stresses;

τ_0^* is the shear strength of adhesive bonds in the absence of normal loading

It can be seen from the table that the smallest values of the strength of adhesive bonds and the adhesive component of the friction coefficient are observed for samples processed by HPT in the presence of a bone tissue simulator in the form of hydroxyapatite suspension on the contact surfaces. This may be related to the fact that despite the post-processing annealing after HPT processing and some grain size growth, the high strength of the investigated material is preserved [13]. In addition, this may be due to the lubricating effect of HA which provides the creation of an intermediate "third body" [29]. This is confirmed by the results of the tribological tests for the samples in the initial state and after SPD processing by HPT and ECAP with the use of hydroxyapatite.

5. CONCLUSIONS:

1. The performed research demonstrates a high efficiency of increasing the strength of the Mg-1%Ca magnesium alloy by deformation treatment. The SPD processing by ECAP and HPT reduced the mean grain size from originally 100 μm to 4 μm and 1,4 μm, respectively, which had an effect on the tribological behavior of the examined conjugations.
2. With decreasing grain size, the values of the shear strength of adhesive bonds and the adhesive component of the friction coefficient also decreased, by 9% after ECAP processing and by 35% after HPT. The adhesive component of the friction coefficient decreased by about 18% after both types of deformation treatment.
3. Bone tissue simulator (hydroxyapatite) applied onto the contact surfaces in the initial state enables reducing the shear strength of adhesive bonds and the adhesive component of the friction coefficient by 24%. After ECAP processing the shear strength of adhesive bonds decreased by 37%, and after HPT processing – by about 18%.
4. Based on the performed research, it was established that the Mg-1%Ca magnesium alloy can be used as a material for an implant that contacts bone tissue.

Acknowledgments: The authors thank the Russian Foundation for Basic Research for the financial support under project No. 20-58-S52001 and the Ministry of Science and Technology, Taiwan, for the financial support under Grant No. MOST 109-2221-E-002-116.

REFERENCES

1. I.A. Khlusov, D.V. Mitrichenko, A.B. Prosolov, O.O. Nikolaeva, G.B. Slepchenko, Yu.P. Sharkeev, *Short review of the biomedical properties and application of magnesium alloys for bone tissue bioengineering*, Bulletin of Siberian Medicine. 2019; 18 (2): 274–286. DOI:10.20538/1682-0363-2019-2-274-286
2. F. Witte, *The history of biodegradable magnesium implants: A review*, Acta Biomater. 2010; 6 (5): 1680–1692. doi:10.1016/j.actbio.2010.02.028
3. R.Z. Valiev, Y. Estrin, Z. Horita, T.G. Langdon, M.J. Zehetbauer, Y.T. Zhu, *Producing bulk ultrafine-grained materials by severe plastic deformation*, JOM: the journal of the Minerals, Metals & Materials Society 58(4): pp 33-39//2006. DOI:10.1007/s11837-006-0213-7
4. T.C. Lowe and R.Z. Valiev, *The use of severe plastic deformation techniques in grain refinement*, JOM: 56(10): pp. 64-68//2004. https://doi.org/ 10.1007/s11837-004-0295-z
5. B. Stalin, V. S. Vidhya, M. Ravichandran, A. Naresh Kumar, G.T. Sudha, *Characterization and Properties of Mg–TiO_2 Composites Produced via Ball Milling and Powder Metallurgy*, Metallofiz. Noveishie Tekhnol., 42, No. 4: 497–509 (2020), DOI:10.15407/mfint.42.04.0497.
6. S. Manivannan, J. Vairamuthu, Samuel Tilahun, M. D. Vijayakumar, C. Ramesh Kannan and B. Stalin, *The influence of rare earth cerium addition on mechanical and corrosion properties cast Mg-6Al-1Zn magnesium alloy*//2020 IOP Conf. Ser.: Mater. Sci. Eng. 988 012111. https://doi.org/ 10.1088/1757-899X/988/1/012111
7. B. Stalin, M. Ravichandran, V. Mohanavel, L.P. Raj, *Investigations on microstructure and mechanical properties of Mg-5wt.% Cu-TiB_2 composites produced via powder metallurgy route*, Journal of Mining and Metallurgy, Section B: Metallurgy 2020 Vol. 56, Issue 1, pp. 99-108. https://doi.org/10.2298/JMMB190315047S
8. J Vairamuthu, S. Tilahun, M.D. Vijayakumar, C. R. Kannan, S. Manivannan and B. Stalin, *The squeeze casting parametric effect on magnesium metal matrix composite*, 2020 IOP Conf. Ser.: Ma-

ter. Sci. Eng. 988 012112 https://doi.org/10.1088/1757-899X/988/1/012112
9. V.M. Chornyi, *The prospects of using biodegradable magnesium-based alloys in osteosynthesis*, Zaporozhskii Meditsinskii Zhurnal. 2013; 6 (81): 76–79 (in Russian).
10. A.Yu. Vinogradov, E.V. Vasiliev, M.L. Linderov, D.L. Merson, E.O. Rzhevskaya, *The effect of equal-channel angular pressing on the structure and mechanical properties of Mg-Zn-Ca magnesium alloy*, Science Vector of Togliatti State University. 2015. № 4 (34), p. 18-24 (in Russian).
11. R.Z. Valiev, *Design of nanostructured metals and alloys with unique properties using severe plastic deformation*, Rossiiskie Nanotekhnologii. – 2006, V.1, №1-2, p. 208-216 (in Russian).
12. R.Z. Valiev, A.P. Zhilyaev, T.G. Langdon, *Bulk Nanostructured Materials: Fundamentals and Applications*, 2014 by John Wiley & Sons, Inc., 456 pages. DOI:10.1002/9781118742679
13. O. Kulyasova, R. Islamgaliev, H.-C. Lin, H. Yılmazer, Microstructure and Mechanical Properties of the UFG Magnesium Alloy Mg-1%Ca, Materials Science Forum. 2020. V. 1016, pp 768-773. DOI: 10.4028/www.scientific. net/MSF.1016.768
14. F. Živić, N. Grujović, G. Manivasagam, C. Richard, J. Landoulsi, V. Petrović, *The Potential of Magnesium Alloys as Bioabsorbable /Biodegradable Implants for Biomedical Applications*//Tribology in Industry, Vol. 36, No. 1 (2014) 67-73.
15. S.-J. Huang, Y.-R. Jeng, V. I. Semenov and Y.-Z. Dai, *Particle Size Effects of Silicon Carbide on Wear Behavior of SiC_p-Reinforced Magnesium Matrix Composites*, Tribology Letters (2011), V. 42, No. 1, p. 79-87. https://doi.org/10.1007/ s11249-011-9751-4
16. V.I. Semenov, L.Sh. Shuster, C.V. Chertovskikh, Y.-R. Jeng, S.-J. Huang, Y.-Zh. Dao, S.-J. Hwang *Tribology of Composite Materials on the Basis of Magnesium Alloy with Powder Filler of SiC*, Tribology in Industry, Volume 29, No. 1&2, 2007, p. 37-40.
17. V.I. Semenov, Y.-R. Jeng, S.-J. Huang, Y.-Zh. Dao, S.-J. Hwang, L.Sh. Shuster, S.V. Chertovskikh and P.-Ch. Lin, *Tribological properties of the AZ91D magnesium alloy hardened with silicon carbide and by severe plastic deformation*, Journal of Friction and Wear. Vol. 30, (2009), pp. 194–198
18. Y.D Liao, Z.Y Li, G.Q Tang. *Evaluation for adhesion strength of coating and substrate by burying beforehand specimen*, Journal of Wuhan University of Technology-Mater Sci Ed Vol. 18, (2003), pp. 31-35.
19. S.A. Lurie, P.A. Belov, D.B. Volkov-Bogorodsky, *Multiscale modeling in the mechanics of materials: cohesion, interfacial interactions, inclusions and defects*, in book: Lecture Notes in Applied and Computational Mechanics–Analysis and Simulation of Multield Problems, vol. 12, Springer, 2003 DOI:10.1007/978-3-540-36527-3_9
20. Y. Ichikawa, S. Barradas, F. Borit, V. Guipont, M. Jeandin, M. Nivard, L. Berthe, K. Ogawa, T. Shoji, *Evaluation of Adhesive Strength of Thermal-Sprayed Hydroxyapatite Coatings Using the LAser Shock Adhesion Test (LASAT)*, Materials Transactions, Vol. 48, No. 4 (2007) pp. 793-798. DOI.org/10.2320/matertrans.48.793
21. Y. Zheng, *Magnesium Alloys as Degradable Biomaterials*, CRC Press, 2015, 578 p. DOI:10.1201/b18932
22. L.Sh. Shuster *Adhesive Interaction Between Solid Metallic Bodies*, Ufa: Gilem, ISBN 5-7501-0147-9, 1999, 198 p. (in Russian).
23. J.F. Nie, *Precipitation and Hardening in Magnesium Alloys*, Metall Mater Trans A 43, 3891–3939 (2012). DOI:10.1007/s11661-012-1217-2.
24. K. Oh-ishi, R. Watanabe, C.L. Mendis, K. Hono, *Age-hardening response of Mg–0.3 at.%Ca alloys with different Zn contents*, Materials Science and Engineering (2009) A 526(1) p.177-184 DOI:10.1016/j.msea.2009.07.027
25. E.V. Vasilev, V.I. Kopylov, M.L. Linderov, A.I. Brilevsky, D.L. Merson, A.Yu. Vinogradov, *High strength and fatigue properties of Mg-Zn-Ca alloys after severe plastic deformation*, Letters on Materials. 9(2) (2019), pp 157-161. https://doi.org/10.22226/2410-3535-2019-2-157-161
26. S.V. Dobatkin, E.A. Lukyanova, N.S. Martynenko, N.Yu. Anisimova, M.V. Kiselevskiy, M.V Gorshenkov, N.Yu. Yurchenko, G.I. Raab, V.S. Yusupov, N. Birbilis, G.A. Salishchev and Y.Z. Estrin, *Strength, corrosion resistance, and biocompatibility of ultrafine-grained Mg alloys after different modes of severe plastic deformation*, IOP Conf. Ser.: Mat. Sci. Eng. 194 (2017) 012004. DOI:10.1088/1757-899X/194/1/012004
27. W. Li, X. Liu, Y. Zheng, W. Wang, W. Qiao, K.W.K. Yeung, K.M.C. Cheung, S. Guan, O.B. Kulyasova, R.Z. Valiev, *In vitro and in vivo studies on ultrafine-grained biodegradable pure Mg, Mg-Ca alloy and Mg-Sr alloy processed by high-pressure torsion*, Biomaterials Science. V.8, I.18, p. 5071-5087. DOI:10.1039/d0bm00805b
28. F.S. Novik, Ya.B. Arsov, *Optimization of Metal Technology Processes by Experiment Design*, Moscow: Mashinostroenie, 1980. 304 p. (in Russian).
29. I.V. Kragelskiy, *Friction and Wear*, Moscow: Mashinostroenie, 1968. 480 p. (in Russian).

Nanophase structures in vacuum multilayer coatings formed on tool and high-speed steels

Yauheni Auchynnikau[1], Nikolai Chekan[2], Gennady Kostukovich[1], Igor Akula[2], Alexander Ogorodnikov A.[3]
Faculty of Innovative Mechanic Engineering [1], Faculty of Engineering and Construction [3] – Yanka Kupala State University of Grodno, Belarus
Department of thin films and coatings - Physical-Technical Institute of the National Academy of Sciences of Belarus [2]

Abstract: *The most common coatings for metalworking tools include titanium nitride, titanium carbide, titanium carbonitride, zirconium nitride, zirconium carbide, zirconium carbonitride, compounds based on chromium, titanium, aluminum, diamond-like coatings that are formed in vacuum using PVD, CVD, PCVD methods or a combination of the above methods. The current trend in the deposition of vacuum coatings is the production of multifunctional coatings, which can significantly increase operational characteristics compared to the starting materials. To form multifunctional coatings, the creation of "sandwich" structures is used, since each layer performs various functions - forming, antiwear, anticorrosion. Thus, the use of a composite multilayer coating containing layers of titanium nitride, titanium, diamond-containing compounds with a thickness of one layer from 0.1 to 2 microns makes it possible to increase the wear resistance of a metalworking tool by 1.5-5 times.*

KEYWORDS*: MORPHOLOGY, DIAMOND-LIKE COATINGS, PROPERTIES, STRUCTURE.*

1. Introduction

Coatings of diamond-like carbon (DLC) have a whole range of necessary tribological characteristics, the main of which are high hardness, low values of the friction coefficient, and chemical inertness. However, it is well known that the tribological properties of DLC coatings—whether hydrogenated (a-C:H) or non-hydrogenated (a-C)—are highly dependent on the operating conditions of the medium. The mechanism responsible for this effect is probably associated with the interaction of carbon with uncompensated bonds in gas phase particles, for example, water. Consequently, the use of conventional DLC coatings may not be applicable when extreme or labile operating conditions are expected, as in internal combustion engines, turbines, which must operate in both high and low temperatures, humidity. In this connection, there was a nanocomposite coating consisting of nanoparticles of solid WC and solid lubricant WS_2 embedded in a non-hydrogenated matrix. DLC principles have been described in a number of works. According to data available in the literature, coatings based on tungsten carbides in combination with titanium and cobalt are significantly less sensitive to environmental influences. The combination of DLC coatings and coatings based on tungsten carbide will significantly change the tribological and corrosion characteristics of the formed multifunctional coatings. However, most works do not consider the formation of nanocomposite structures in multilayer coatings based on systems modified tungsten carbide - APP. Nanocomposite coatings with a microstructure consisting of nanocrystalline grains in an amorphous matrix of a diamond-like coating must have unique mechanical and tribological parameters. Thus, it is possible to create superhard coatings with microhardness values of ~50–55 GPa, i.e. nanocomposite coatings were created in which plastic deformation was reduced in order to increase hardness. This mechanism for reducing the deformation strength can be carried out due to grain boundary and dispersion strengthening. Materials with low ductility are quite brittle.

Therefore, they are not ideal for applications where high contact stresses occur, such as plain bearings, where high wear resistance and ductility as well as a low coefficient of friction are required. There are publications that show the creation of good ductile properties in brittle ceramics at room temperature by reducing the grain size to the nanometer level. This approach will make it possible to obtain good tribological characteristics of nanocrystalline oxides of various materials [1-4].

2.1. Preconditions and means for resolving the problem

Further work in this direction showed the promise of including nanocrystalline ceramic grains in a lubricating matrix (if this system is considered as a tribological one), such as coatings based on amorphous carbon (a-C). As a rule, the technologies used for the production of nanocrystalline / amorphous composite coatings lead to the heating of the substrate to a temperature of about 500–600 ° C, which is due to the ongoing processes of the formation of a crystalline phase in the coating. On the other hand, this temperature range can significantly limit the choice of substrate material and reduce the benefits of creating protective coatings. Moreover, at these temperatures, the sp^3 hybridization of bonds in carbon atoms in DLC coatings, which causes high hardness, can pass into a graphite-like phase with a bond of sp^2 hybridizations. Thus, it is necessary to develop other methods for the implementation of crystal formation processes in composite DLC coatings with a-C solid matrix. It is possible to carry out the formation of carbide and carbonitride crystals by sharing a low-energy metal plasma formed by magnetron sputtering with high-energy torches created by pulsed laser ablation of graphite. This technology is Magnetron Pulsed Laser Deposition (MPLD), it can also be used to deposit TiC, TiCN, Hydrogen-Free A-C DLC coatings. The obtained coatings TiC and APP (a-C) have a very high hardness of 27 and 60 GPa, respectively. In addition, the APP coating (a-C) had low friction coefficient values of less than 0.1 under most tribological test conditions. During the formation of this composite coating, a transition of coatings Ti –> APP was observed, with the formation of an intermediate layer according to the scheme Ti → TiC → APP (a-C). This process occurred with an increase in the carbon content. Studies have shown that even when the deposition process is carried out at a temperature of 100 °C, a two-phase TiC → APP region is formed. This approach is used in obtaining the production of nanocrystalline composite coatings TiC / APP (a-C). Thus, the approach of forming multilayer coatings is quite promising for obtaining multifunctional coatings, due to the formation of thin-layer systems of nanocrystalline particles and phases in the structure. Figure 1-8 shows the results of atomic force microscopy of DLC coatings formed on steel substrates of the M2 (HSS) and H13 types.

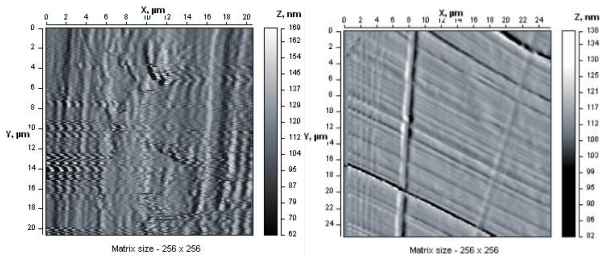

a) b)

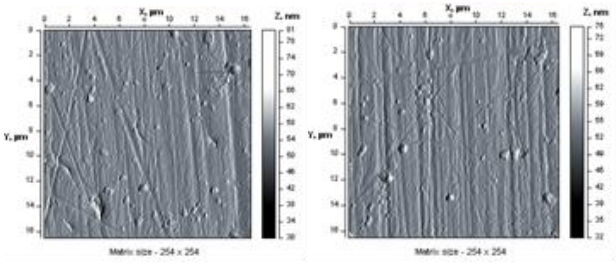

c) d)

Figure 1 *- Morphology of the surface layers of vacuum coatings formed on carbon and high-speed steels (2D image): a - original steel H13, b - original steel HSS; v-steel H13 with a diamond-like coating; g - HSS steel with a diamond-like coating.*

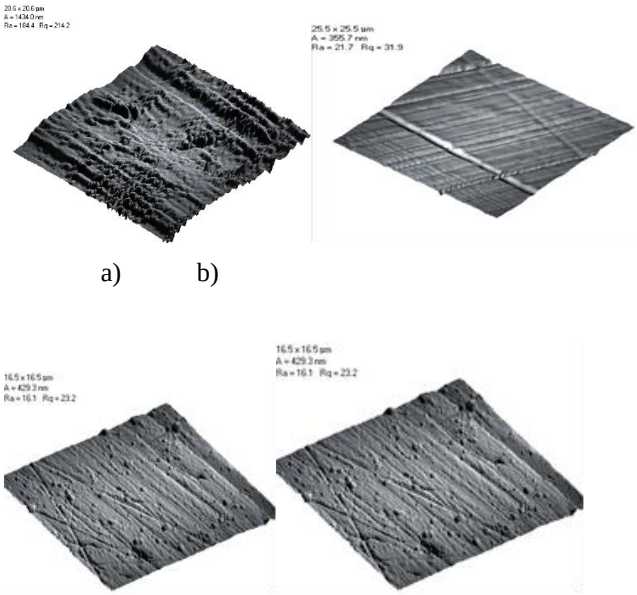

a) b)

c) d)

Figure 2 *- Morphology of the surface layers of vacuum coatings formed on carbon and high-speed steels (3D image): a - original steel 4Kh5MFS, b - original steel R6M5; v-steel 4Kh5MFS with a diamond-like coating; g - R6M5 steel with a diamond-like coating.*

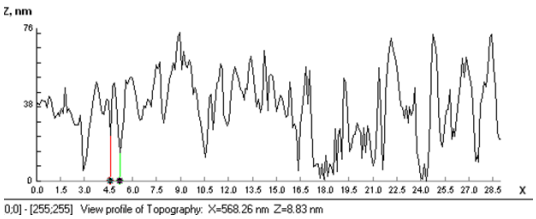

a)

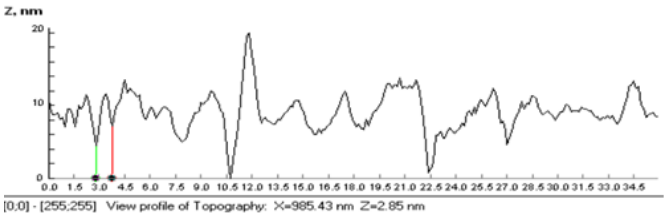

b)

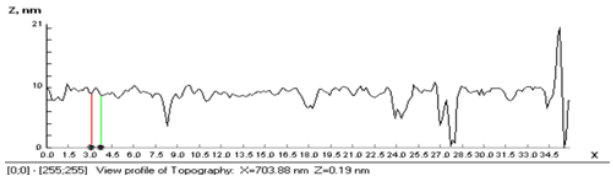

c)

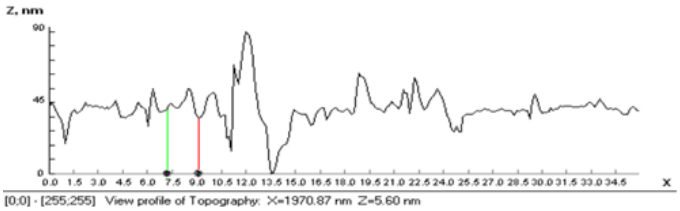

d)

Figure 3 *- Topography of the surface layers of vacuum coatings formed on carbon and high-speed steels): a - original steel H13, b - original steel HSS; v-steel H13 with a diamond-like coating; g - HSS steel with a diamond-like coating.*

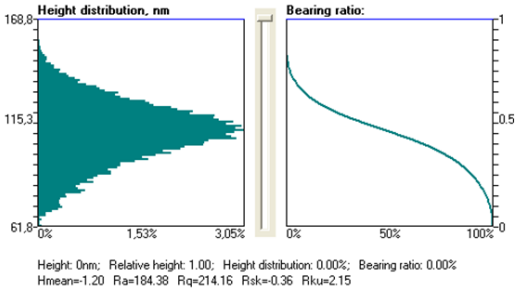

a)

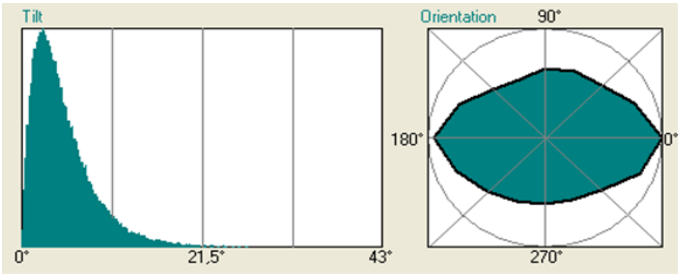

b)

Figure 4 *- The main characteristics of the morphology of the surface layers of steel H13. a-distribution by heights; b-angular distribution*

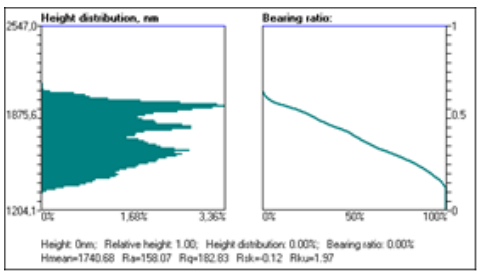

a)

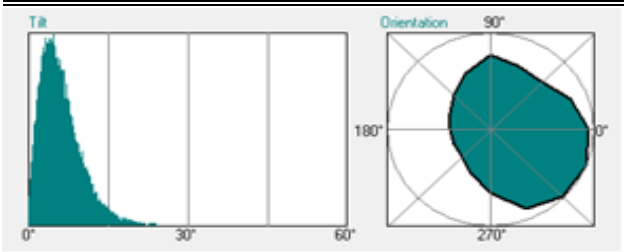

b)

Figure 5 *- The main surface characteristics of steel HSS: a-height characteristic, b-angular distribution.*

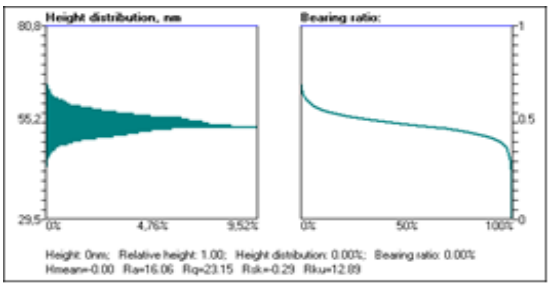

a)

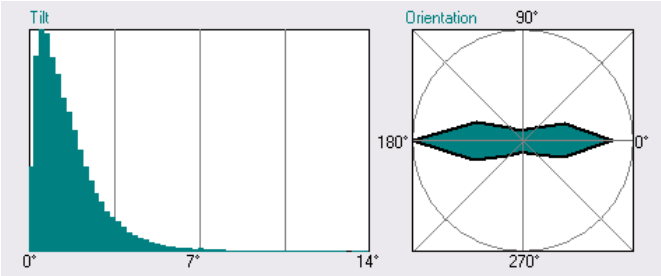

b)

Figure 6. The main surface characteristics of steel H13 with a diamond-like coating: a-height characteristic, b-angular distribution.

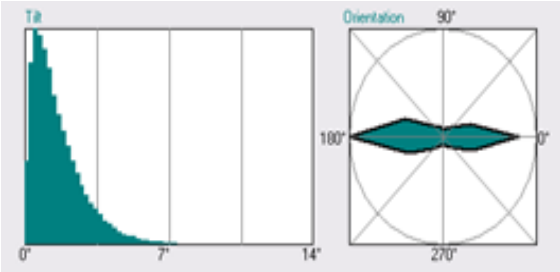

a)

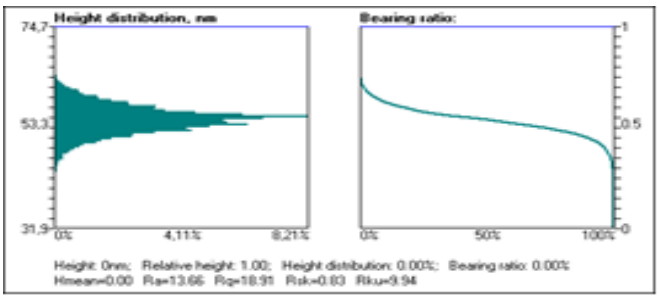

b)

Figure 7 *- The main surface characteristics of HSS steel with a diamond-like coating: a-height characteristic, b-angular distribution.*

Based on the presented data, it can be seen that nanodispersed structures begin to form in diamond-like coatings when they are deposited on the surface of steel substrates. This process is intensified during the formation of APP on superhard layers deposited on steel substrates (Figure 8).

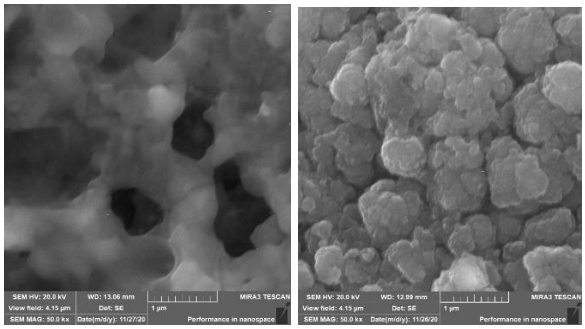

a) b)

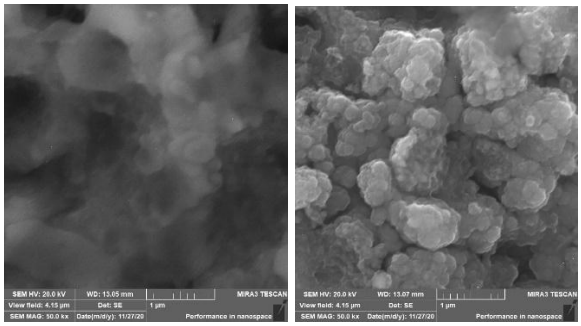

c) d)

Figure 8 *- Morphology of APP coatings formed on superhard sublayers of HSS and H13 steel substrates. a - HSS substrate, VK6 sublayer, Norma 1 sublayer formation mode, b – H13 substrate, VK6 sublayer, Norma 2 sublayer formation mode, c - HSS substrate, VK6 sublayer, Norma 1 sublayer formation mode, b – H13 substrate, VK6 sublayer, sublayer formation mode Norma 2*

The most common coatings for metalworking tools include titanium nitride, titanium carbide, titanium carbonitride, zirconium nitride, zirconium carbide, zirconium carbonitride, compounds based on chromium, titanium, aluminum, diamond-like coatings that are formed in vacuum using PVD, CVD, PCVD methods or a combination of the above methods. The current trend in the deposition of vacuum coatings is the production of multifunctional coatings, which can significantly increase operational characteristics compared to the starting materials. To form multifunctional coatings, the creation of "sandwich" structures is used, since each layer performs various functions - forming, antiwear, anticorrosion. When using a cutting tool with multilayer and composite coatings, the stability of the cutting tool and its performance characteristics change radically, wear is reduced, cutting accuracy is increased, it becomes possible to increase the feed, the quality of surface treatment increases and tool durability increases. Thus, the use of a composite multilayer coating containing layers of titanium nitride, titanium, diamond-containing compounds with a thickness of one layer from 0.1 to 2 μm makes it possible to increase the wear resistance of a metalworking tool by 1.5-5 times. Creation of multilayer vacuum coatings, including those containing nanophases and nanoparticles in their structure, using multicomponent magnetically controlled flows of metal and carbon plasma, of the following composition: (Al-Ti-Cr-Si)-(C, N), CN, CF, CB , will significantly increase the physical and mechanical properties of the modified products. It has been established that the formation of vacuum coatings on a modified steel surface by the method of electrospark alloying also leads to a decrease in the surface roughness values of the modified steel substrate.

Thus, the formation of nanocomposite structures in multifunctional coatings depends on the type of sublayer material, as well as on the modes of coating formation

References:

1. Ti-Al-N hard coatings deposited from filtered vacuum-arc plasma / V.V. Belous [et al.] // Physical engineering of the surface. -2009. - v. 7, No. 3. -S. 216-220.

2. Ovchinnikov, E.V. Tribotechnical characteristics of AlTiN plasma-chemical coatings / E.V. Ovchinnikov, N.M. Chekan, I.P. Akula // Fundamental and applied problems of engineering and technology. - 2014. - No. 1 (303). - S. 55-63.

3.Adhesive activity AITiN layers based on forming polymer coatings / Y. Auchynnikau [et al.] // The proceedings of the Austrian-Slovenian Polymer Meeting 2013 [Elektronski vir] / Austrian-Slovenian Polymer Meeting-ASPM 2013, 3-5 April 2013, Bled, Slovenia; editors Majda Žigon, Teja Rajšp.- El. zbornik. - Ljubljana: Centre of Excellence PoliMaT, 2013. – P. 256- 257.

4. Obtaining and heat treatment of coatings of the Ti-Al-Si-N system / N.M. Coinage [et al.] // Bulletin of the State Duma, ser. 6. - 2013. - No. 2 (154). - S. 31-37. 4. N.M. Chekan [et al.] // Vesník GrDU, ser. 6. – 2013. – № 2 (154). – P. 31-37.

Nanodisperse modifiers produced by the shs method for composite materials of automotive equipment

Auchynnikau Y.[1], Vozniakovskii A.[2], Vozniakovskii A.[3], Semenov A.[1]
Faculty of Innovative Mechanic Engineering [1] – Yanka Kupala State University of Grodno, Belarus
Sector of Polymer Nanostructured Materials, Institute of Synthetic Rubber, Saint-Petersburg, Russian Federation[2]
Laboratory "Physics for Cluster Structures", Ioffe Institute, Saint-Petersburg, Russian Federation[3]

Abstract: *The object of the study was carbon particles obtained by the method of self-propagating high-temperature synthesis. The purpose of the work is the development of compositions and technologies for obtaining competitive composite materials modified with low-dimensional carbon modifiers based on vegetable raw materials.*
KEYWORDS: *CARBON, STRUCTURE, PROPERTIES, COMPOSITES, SELF-PROPAGATING HIGH-TEMPERATURE SYNTHESIS.*

1. Introduction

According to the literature data, the formation of nanodispersed particles by the method of self-propagating high-temperature synthesis makes it possible to obtain low-sized particles with properties that differ from those of bulk carbon materials. The resulting nanosized particles have a high adsorption activity, large specific surface area. The studies performed have shown that, depending on the technology for the formation of these particles in the reactor, it is possible to control the morphology and lateral sizes of the particles, which in the future will make it possible to purposefully change the activity of these particles.

The activity of nanosized particles obtained by self-propagating high-temperature synthesis is due to the imperfection of the formed nanocrystals.

So, for example, if we consider a zero-dimensional, point defect located in a crystal at a distance of no more than 5–7 atomic layers, then an area with mechanical stresses appears on the surface due to violations of atomic mutual configurations. In connection with this, a region with a changed potential appears on the crystal surface. The appearance of these surface defects leads to the appearance of surface active centers (SACs). The interaction of PACs with the molecules of the substance adjacent to them are electromagnetic in nature. The presence of an electric charge is not a prerequisite for the appearance of surface active centers..

At present, one of the promising classes of modifiers for polymeric materials is carbon nanomaterials (CNMs). This classification includes the following substances: detonation nanodiamond, graphene, graphene oxide, graphene nanoplates, single-walled carbon nanotubes, multi-walled carbon nanotubes, fullerenes [1] - [4] of unique properties. In particular, detonation nanodiamonds have thermal conductivity and hardness close to single-crystal diamond. Single-walled carbon nanotubes and multi-walled carbon nanotubes have high physical and mechanical characteristics. The values of the modulus of elasticity for these substances can reach 1.7 - 3.8 TPa, depending on the type of material, and the values of thermal conductivity along the axis of the tube are estimated

~ 3000 W/m K. Graphene has similar physical and mechanical characteristics: thermal conductivity - 5000 W/m K, Young's modulus - 1 TPa, specific surface area - 2630 m^2/g.

Detonation diamonds were first synthesized in the USA in 1961. In the USSR, this class of materials was obtained at UNIITF in 1962. Detonation diamond particles are geometric objects with a lateral size of about 10 nm. The production of this class of substances can be carried out both by blasting technology with a negative oxygen balance, and by mechanical grinding of natural and synthetic diamonds.

Fullerenes were discovered in 1985, but the theoretical justification for the existence of these particles was given back in the 70s of the last century. This class of materials represents molecules of composition C_n, where n>20, which consist of closed convex polyhedra with pentagonal and hexagonal faces. Fullerenes are synthesized by the electric arc method, which is characterized by a low yield of the product required for industrial use, which determines a rather high cost per gram of material.

In 1991, single-walled carbon nanotubes were synthesized. This allotropic form of carbon is hollow rods consisting of hexagons, at the tops of which there are carbon atoms and up to several tens of nanometers in diameter. The main methods for obtaining this class of materials are laser dispersion of a graphite target, the effect of electric spark discharges on a carbon material, and the formation of nanotubes in vacuum using plasma-chemical methods. However, the above methods are inefficient. Therefore, to obtain nanotubes on an industrial scale, the method of chemical deposition of carbon tubular particles from the gas phase is used [1] – [7]. Multi-walled carbon nanotubes are obtained by a similar method.

Graphene was obtained in 2004 by exfoliation and subsequent deposition on the surface of silicon oxide. Graphene is a flat layer of sp^2-hybrid carbon atoms one atom thick, forming a hexagonal lattice. Graphene nanostructures are understood as materials consisting of 2 – 100 graphene layers. For the synthesis of graphene nanostructures, the following technological approaches are used: "bottom-up", "top-down" [1-7].

2.1. Preconditions and means for resolving the problem

In the course of the studies, the morphology of carbon nanoparticles obtained using the technology of self-propagating high-temperature synthesis from various raw materials was evaluated. It has been established that the technology of obtaining and the prehistory of the sample has a significant impact on the morphology of the formed carbon nanoparticles.

In most cases, nanodispersed carbon particles obtained by the SHS method, due to their high activity, form agglomerates that are quite stable. These formations are in the micron range of dimensions, which is confirmed by the data of scanning electron microscopy. Thus, these objects can be studied by optical microscopy. Figures 1 - 3 show agglomerates of carbon particles produced by the SHS method from various materials with different content of combustible matter.

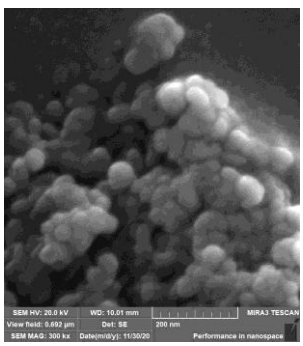

a)

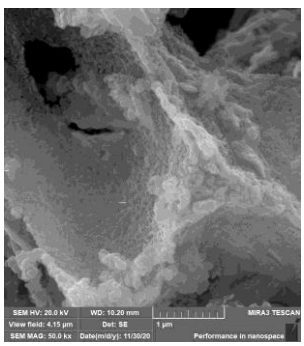

b)

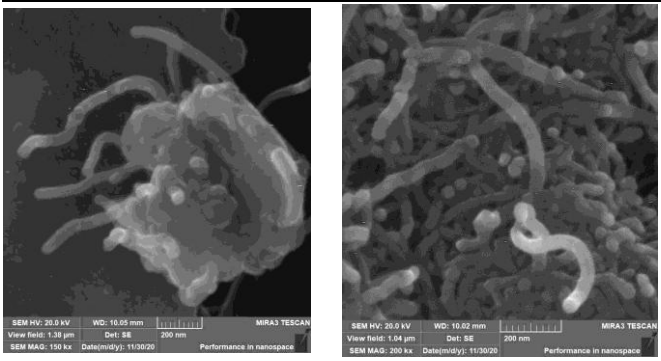

c) d)

a – ultrafine diamond-containing graphite, b – graphene nanoplates, c – nanodispersed carbon particles obtained from starch, d – multilayer carbon nanotubes

Figure 1 - Morphology of nanodispersed carbon particles obtained by the method of self-propagating high-temperature synthesis

Carbon nanodispersed particles were obtained by the method of self-propagating high-temperature synthesis (SHS) . This technology for obtaining nanocarbon particles is exothermic due to the occurrence of chemical processes such as combustion. The combustion process is autowave, flowing through a mixture of reagents with the formation of solid carbon end products of various dispersion. An exothermic reaction occurs in the process of supertemperature self-propagating synthesis, and this process is localized in a narrow range. The heating temperature of the initial material for the implementation of structural transformations in the initial mixture can reach 2000–3000 °C, depending on the initial raw material and combustible materials that make up the mixture for SHS synthesis. As a result, the high-temperature front of SHS synthesis passes from layer to layer of the initial charge. This is an advantage of the technology of self-propagating high-temperature synthesis, which consists in using the heat of chemical reactions released in the heating zone of a substance, instead of volumetric heating of the entire material from an external source. This technological feature of the SHS method makes it possible to successfully compete with the widespread energy-consuming technologies for obtaining nanosized carbon particles.

The studied nanodispersed carbon particles were obtained on the basis of the principle of nanoparticle formation known as "bottom-up". As a result of applying this approach, the structure of the organic material changes with the formation of various carbon structures: graphite, diamond, fullerene, graphene, graphane, nanotubes, etc. The existing alternative technology for creating carbon nanoparticles is the "top-down" technology, the advantage of which is the low cost of the process, relative technological simplicity, and the ability to obtain large volumes of synthesized material.

The application of the principles of formation of carbon nanodispersed structures "bottom-up" makes it possible to obtain carbon structures of various dispersity. Usually, dispersion is understood as the reciprocal of the average geometric dimensions of the object under study. According to one of the classifications of the geometric dimensions of objects, they can be divided into molecular, highly dispersed and coarsely dispersed. Based on this classification, it can be seen that these systems will differ significantly in their physical, mechanical, and chemical characteristics. Thus, the study of the dispersity distribution of formed nanodispersed carbon particles by the SHS synthesis method will make it possible to predict the properties of both the obtained nanocarbon particles themselves and composite materials using this type of substances as a modifier.

As objects of research, the dispersion composition of the following carbon particles was studied: carbon agglomerates obtained by the method of self-propagating high-temperature synthesis from cellulose with a percentage of the starting material to a combustible substance of 30:70% wt.; carbon agglomerates obtained by the method of self-propagating high-temperature synthesis from starch with a percentage of the starting material to a combustible substance of 30:70% wt. The research results are presented in figures 1 - 3.

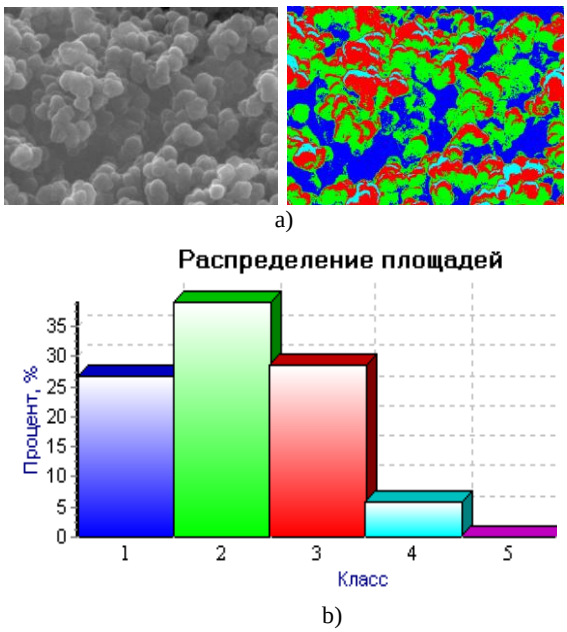

a)

b)

a – SEM image of the test substance, including after the analysis; b - percentage distribution of carbon particles by size in the test sample

Figure 2 - The results of the dispersion analysis of carbon particles obtained by the method of self-propagating high-temperature synthesis from cellulose with a percentage of the starting material to the combustible substance of 30:70% wt.

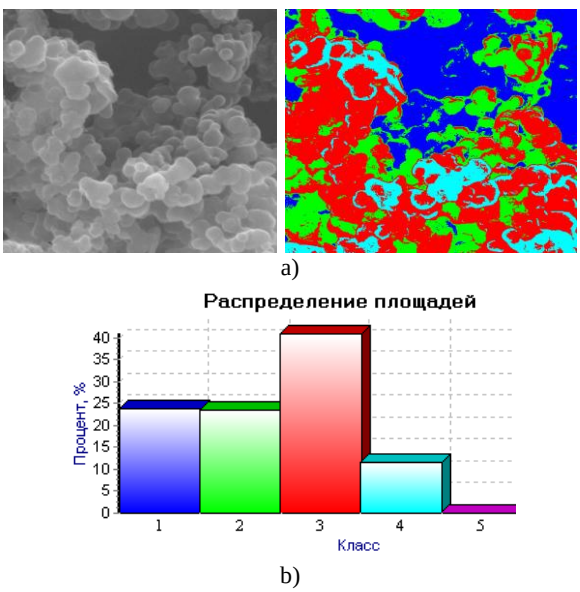

a)

b)

a – SEM image of the test substance, including after the analysis; b - percentage distribution of carbon particles by size in the test sample

Figure 3 - The results of the dispersion analysis of carbon particles obtained by the method of self-propagating high-temperature synthesis from starch with a percentage of the starting material to the combustible substance of 30:70% wt.

To carry out dispersion analysis of nanodispersed carbon particles obtained by SHS synthesis, we used the method of scanning electron microscopy, which makes it possible to obtain images of particles with a resolution in the nanometer region. For image processing, a specialized program "AutoScan" produced by CJSC "Spectroscopic Systems" was used. According to the size of carbon nanoparticles, they were divided into 5 classes: class 1 - from 300 nm to 400 nm, class 2 - from 200 nm to 300 nm, class 3 - from 100 nm to 200 nm, class 4 - from 50 nm to 100 nm, Class 5 - less than 50 nm.

In the course of the conducted studies, it was found that as a result of the use of self-propagating high-temperature synthesis for the processing of organic raw materials, particles of the nanometer range with different dispersion distributions are formed. The dispersity of the studied samples depends on the organic raw materials used.

It is shown that, depending on the methodology for the formation of carbon particles, various structures are formed with characteristic properties inherent only to them. Thus, the formation of diamond-like structures, fullerenes, fullerites, carbon nanotubes, rods, disks, graphenes, etc. is possible. These materials differ significantly in properties from each other. The disadvantage of the considered technologies is, in most cases, the high cost of the obtained particles, as well as the low yield of carbon nanocluster structures. In some cases, environmentally harmful technologies are used. In this connection, the use of the technology of self-propagating high-temperature synthesis will make it possible to obtain carbon nanoparticles of various nomenclature in large quantities. The use of the SHS method will make it possible to obtain nanosized cluster structures not only of carbon, but also of materials consisting of other chemical elements of the periodic system of D.I. Mendeleev. The main advantage of the SHS method is its sufficient simplicity and environmental safety. Using the method of self-propagating high-temperature synthesis, it is possible to obtain low-sized particles with properties different from those of bulk carbon materials. The resulting nanosized particles have a high adsorption activity, large specific surface area. The studies performed have shown that, depending on the technology for the formation of these particles in the reactor, it is possible to control the morphology and lateral sizes of the particles, which in the future will make it possible to purposefully change the activity of these particles. The activity of nanosized particles obtained by self-propagating high-temperature synthesis is due to the imperfection of the formed nanocrystals. So, for example, if we consider a zero-dimensional, point defect located in a crystal at a distance of no more than 5-7 atomic layers, then a section with mechanical stresses appears on the surface due to violations of atomic mutual configurations. In connection with this, a region with a changed potential appears on the surface of the crystal. The appearance of these surface defects leads to the appearance of surface active centers (SACs). The interaction of PACs with molecules and substances adjacent to them are electromagnetic in nature. It is shown that in the process of self-propagating high-temperature synthesis, the formation of combined particles of the DND-CNT, CNT-CND (carbon nanodiscs) type occurs; in some cases, the formation of structures such as graphene and graphene nanoplates, lonsdaleite is possible.

In the course of the conducted studies, it was found that as a result of the use of self-propagating high-temperature synthesis for the processing of organic raw materials, particles of the nanometer range with different dispersion distributions are formed. The dispersity of the studied samples depends on the organic raw materials used.

References:

1. Burchell Ed. T. D. Carbon materials for advanced technologie – Pergamon: USA Elsevier Science Ltd., 1999. – 540 p.
2. Kratschmer W., Huffman D. R. Fullerites: new form of crystalline carbon. // Carbon. – 1992. – Vol. 30, № 8. – P. 1143 – 1147.
3. Hirsch A. The Chemistry of the Fullerenes. – Stuttgart: G. Thieme Verlag, 1994. – 203 p.
4. Iijima S. Helical microtubules of graphitic carbon // Nature. – 1991. – Vol. 35. – P. 56 – 58.
5. Nanostructured Materials: Science and Techmology / Ed. G. M. Chow, N. I. Noskova. – Dordrecht: Kluwer Acad. Publ., 1998. – 457 p.
6. Zhu Y. [et al.] Graphene and graphene oxide: synthesis, properties, and applications // Advanced materials. – 2010. – V. 22, № 35. – P. 3906 – 3924.

Influence of mechanically activated particles on the activity of polymer engineering materials and compositions based on themt

Yauheni Auchynnikau [1], Tatiana Grigorieva[2], Yauhenia Eisimont[1], Valeri Sorokin[1], Ilya Mysika[1]
Faculty of Innovative Mechanic Engineering [1] – Yanka Kupala State University of Grodno, Belarus
Laboratory of Chemical Materials Science[2] – Solid State Chemistry and Mechanochemistry
of the Siberian Branch of the Russian Academy of Sciences, Russia

Abstract: *The article presents the results of studies on the study of the physical and mechanical characteristics of polymeric materials modified with mechanically activated particles. It is shown that the use of mechanically activated nanosized particles makes it possible to achieve a significant effect of increasing operational characteristics at relatively low degrees of modification of 0.05% wt. – 3% wt. The use of modifiers at such concentrations in polymer matrices makes it possible to preserve the basic technology for the processing of polymeric materials and equipment in the manufacture of composite materials on a polymer matrix.*
KEYWORDS: *POLYMER, VISCOSITY, STRENGTH, MECHANICAL ACTIVATION, STRUCTURE.*

1. Introduction

The formation of functional composite materials based on thermoplastic and thermoplastic polymers is in most cases achieved by extensive modification of matrices with powders, fibers, agglomerates, clusters, etc. varying degrees of dispersion. The use of nanocomposite materials based on polymers is a promising trend in the development of modern mechanical engineering. To modify regular and irregular high-molecular compounds, various types of low-sized particles are used: micas, metals, metal oxides, clays, graphenes, sialons, graphite, etc. The geometric parameters of individual crystals of low-sized particles are in the range of 1-5 nm. The conducted studies on the study of the activity of nanoscale objects showed high values of the specific surface area, residual charge, which indicates a high modifying ability of these objects.

The energy state of nanosized particles essentially depends on the habitus of the nanomaterial, its composition, and the formation technology. The influence of these parameters has a significant effect on the structure of the surface layers of the particles of the resulting composite material, which determines the force interaction within the volume of the composite.

The influence of the force field of nanoparticles leads to a change in the predominant orientation of the modified polymer molecules in space, which makes it possible to obtain nanophases in the bulk of the material with a higher degree of orientation compared to other phases of the composite material. The main disadvantage of these materials is the loss of activity over time. In this regard, various technological methods are proposed for the activation of low-dimensional systems or the creation of systems of nanomodifiers with a prolonged lifetime of the active state.

Thus, the establishment of the mechanism of influence and interaction of mechanically activated particles with an uncompensated charge on the structure and properties of structural thermoplastics is of both theoretical and practical interest. The creation of these modifiers will make it possible to obtain composite materials with enhanced functional characteristics. As modifiers of polymeric materials, organic and inorganic dispersed particles of various kinds and origins are widely used. One of the current trends in purposeful changes in the structure and properties of polymeric materials is the use of nanodispersed particles with a high specific surface area, which contributes to a higher activity when interacting with a polymer matrix [1-4]. Nanodispersed particles of diamond-containing compounds obtained by blasting technology with a negative oxygen balance have found the widest application in industry.

The technology for obtaining such compounds has been developed at a sufficiently high level, and the structure and properties of diamond-containing nanoparticles have been well studied [1]. The disadvantage of this class of nanomaterials is the high cost of the final product (diamond nanoparticles), which ranges from $0.5 per carat and more. An alternative for obtaining low-dimensional active modifiers using existing technologies is the use of the mechanical activation (MA) method. Mechanical activation of organic compounds or mixtures of organic compounds and inorganic substances makes it possible to obtain composite nanosized, nanophase particles that meet the criteria of environmental friendliness, ergonomics, resource saving, financial savings. This technology makes it possible to carry out the reactions of high-molecular compounds of an ordered structure with surface layers of inert materials.

In the course of mechanochemical activation, the destruction of polymer molecules occurs with the formation of active radical groups, which can interact with hydroxyl groups of silicates to form composite particles of various dispersed compositions, including those in the nanometer range. The structure of these particles is a layered composite, in which the radical groups of polymeric materials are chemically bonded at the molecular level to the carrier metal ions of silicate. A number of works have previously shown the interaction of polymeric materials with layered silicates, including during mechanical activation, in which it is assumed that there is a relationship between the shape (habitus) of a particle and the charge activity of the obtained nanocomposite particles. The purpose of this work was to study the physical and mechanical characteristics of polyamide modified with composite mechanically activated particles.

A widely used polymeric material in mechanical engineering, in particular in the production of automotive and tractor equipment, is polyamide.

2. Preconditions and means for resolving the problem

At present, polyamide 11 is widely used in the automotive industry. This material is used as a block product and coatings in automotive units manufactured by leading companies in the world, including. Mersedes Benz, Wabko, Comatsu, Ford, etc. Target additives are introduced into polyamide 11 (Rilsan) - antioxidants, dyes, dry lubricants, which are graphite, molybdenum disulfide, aliphatic amines. Polyamide 11, used for coating, is produced in the form of a powder with a particle size of 80-10 microns. To ensure a stable level of adhesive strength of the coating with a substrate of carbon steels, an undercoat ("primer") of Rilprim based on an epoxy resin oligomer is used. The sublayer is applied in the form of a solution by spraying or dipping on a thoroughly cleaned surface of a metal part, after which it is dried and heat treated in the temperature range of 290-340 ºC for 5-20 minutes. A Rilsan coating is applied to the metal part prepared in this way from a fluidized bed, which is melted to form a layer with a thickness of 100-500 microns. After cooling, the coatings are processed to size using special tools, such as broaches.

The disadvantages of this material for domestic manufacturers are due to the fact that: the lack of large-tonnage domestic production of polyamide 11 in the Union State, which does not allow mastering the industrial production of the powder component, which is the basis for the coating; insufficient adhesion of the coating to metal products and substrates without special preparation; the need to apply a special sublayer (“primer”) to the metal surface, which provides the necessary adhesive strength of the coating and substrate; complex coating technology, involving high energy costs; the need to use special methods for cleaning the environment due to the fact that during the application, heat

treatment of the sublayer (Rilprim), a large amount of environmentally harmful components in the gaseous state are released. A replacement for an imported analogue can be found by using different dispersions of polyamide 6, modified with a mechanically activated mixture of polyamide 6 - kaolinite, with a content of nanometer-sized particles of 20-50 nm. Figure 1 shows the rheological characteristics of polyamide 6 modified with mechanically activated particles.

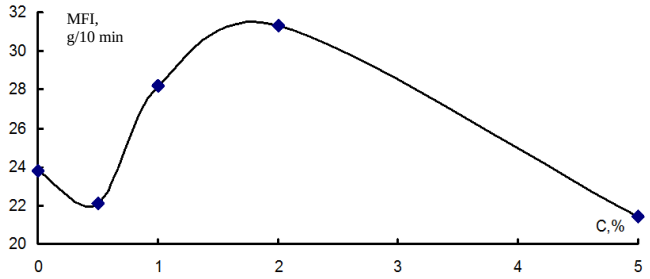

***Figure 1** - Rheological characteristics of polyamide 6 modified with mechanically activated particles polyamide 6-kaolinite*

The introduction of mechanically activated particles at low concentrations leads to an increase in the viscosity characteristics of the composite material. A further increase in the content of the modifier in the composition leads to a decrease in the values of the viscosity characteristics. The maximum increase in the fluidity of the modified polymer is observed at 2% wt. modifier content. Increasing the content of the modifier to 5% wt. increases the values of viscosity characteristics.

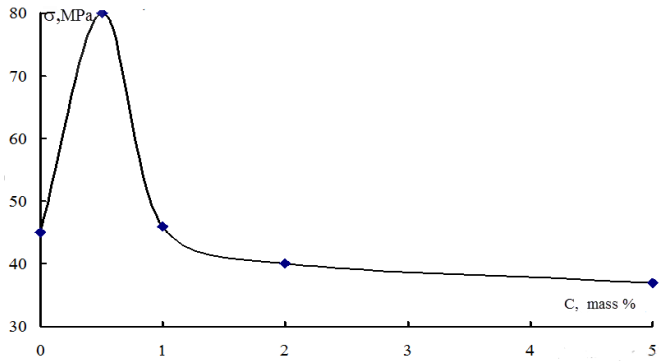

***Figure 2** - Dependence of the tensile strength of polyamide 6 modified with a mixture of mechanically activated particles of polyamide 6-kaolinite on the concentration of the modifier.*

The increase in viscosity with the content of the modifier at 0.5% wt. is explained by the formation of a labile network of physical bonds formed as a result of the interaction of electric charges of mechanically activated particles and dipole charges of polar polyamide 6 molecules. and plastic deformation of the surface layers of the polymer matrix both in the process of friction and in the process of mechanical destruction Increase in the fluidity of the composite material at 2% wt. is explained by an increase in the concentration of particles in the bulk of the polymer, as a result of which these particles begin to interact with each other with the formation of agglomerates capable of breaking down at low tangential shear stresses. A further increase in the concentration of the modifier, leading to an increase in the viscosity characteristics, is explained by classical concepts associated with the modification of polyamide materials with various types of modifiers. The introduction of mechanically activated particles into the polyamide matrix leads to a change in the strength characteristics of the composite material.

In the area of modifier concentration of 0.5 wt.%, an increase in strength characteristics up to 80 MPa is observed. A further increase in the concentration of the modifier in the polymer matrix leads to a decrease in the values of the ultimate tensile strength. This is due to the interaction between charge clusters, the formation of large agglomerates of mechanically activated particles with low cohesive strength in the bulk of the polyamide matrix, which leads to a decrease in strength characteristics.

Table 1 shows the physical and mechanical characteristics of polyamide 6 modified with a mechanically activated mixture of PA6-kaolinite.

***Table 1** - Physical and mechanical characteristics of polyamide 6 modified with mechanically activated particles "PA6-kaolinite"*

Options	raw material	0,5 %	2 %	5 %
Physical yield strength, MPa	30,6	49,5	28,3	16,2
Deformation at physical yield strength, %	19,85	6,9	4,2	4,9
Strength at maximum force, MPa	48,6	77,6	30,2	37,6
Deformation at maximum force, %	133,4	81,6	5,6	9,2
Breaking strength, MPa	48,6	77,6	30,2	37,6
Deformation at failure, %	133,4	81,6	5,6	9,16

The use of mechanically activated nanosized particles makes it possible to achieve a significant effect of increasing performance at relatively low degrees of modification of 0.05 wt. – 3% wt. The use of modifiers at such concentrations in polymer matrices makes it possible to preserve the basic technology for the processing of polymeric materials and equipment in the manufacture of composite materials on a polymer matrix.

The main effect explaining the increase in the physico-mechanical characteristics of polymer nanocomposites upon modification with nanosized mechanically activated particles is the formation of a spatial network of labile physical bonds of the adsorption type in the polymer layer, as well as the influence of the modifier on the kinetics of the formation of the polymer layer from the liquid phase with the formation of supramolecular and pseudocrystalline ordered structures.

The conducted studies on the study of the structure of particles obtained using mechanical activation showed that the formed particles of both organic and inorganic structures differ significantly from each other depending on the technological processing modes and on the initial semi-finished products used.

Studies on the study of the structure of mechanically activated silicate particles with polymeric materials showed that with an increase in the time and modes of mechanical activation, amorphization of the structure of the resulting composite silicate-polymeric materials occurs, and the habitus of microparticles changes. In the course of mechanoactivation, the values of parameters corresponding to an increase in the activity of the resulting composite particles increase.

The developed compositions of composite materials based on polyamide 6 belong to the field of polymer materials science and can be used in mechanical engineering for the manufacture of coated friction parts used in automotive units such as a shock absorber, driveline, brake chamber, etc.

3. References:

1.Khaibullin I.B. [et al.] Ion synthesis in viscous organic // Nuclear Instruments and Methods in Physics Research B. – 1997. –Vol. 127/128. – P. 665 – 690.

2.Grigorieva T.F. [et al.]. Solid-state interaction of kaolinite and acids during joint mechanical activation. // J. Mater. Synth. and Proc. − 1996. – Vol. 4, 5. − P. 299 – 305.

3.Yiu-Wing Mai, Zhong-Zhen Yu Polymer nanocomposites – Cambrige, Woodhead Publishing Limited, 2006 – 594 p.

4. Physicomechanical characteristics of composite materials modified with mechanically activated particles/ Y. Auchynnikau [et. al.] // Fundamental bases of mechanochemical technologies : The book of abstracts of the V International Conference \"Fundamental bases of mechanochemical technologies\". 25-28 June 2018, Novosibirsk, Russia.- Novosibirsk : IPC NSU, 2018 .- P.167

Corrosion protection of aluminum AA1050 alloy by growth of porous anodic Al_2O_3 layers

Christian Girginov, Stephan Kozhukharov
University of Chemical Technology and Metallurgy
1756 Sofia, Bulgaria

Aluminum and its low doped alloys find various applications in both mass production and hi-tech industrial sectors. Almost all aluminum products are subjected to anodizing, which is a relatively simple process that under certain conditions allows the formation of highly ordered porous Al_2O_3 layers. Of particular importance for their successful application is their barrier ability when working in corrosive environments.

The samples of technically pure aluminum (AA1050) were submitted to anodization and subsequent electrochemical measurements. The anodization was performed for 50 min in 15%wt. H_2SO_4 in galvanostatic (15 mA cm^{-2}) and isothermal (20 °C) regime. Under these conditions, the formed Al_2O_3 matrices are 20 microns thick and have a porosity of 20%. The samples were subjected to prolonged exposure (up to 336 hours) in a 3.5% NaCl model corrosive medium. The measurements were performed by Electrochemical Impedance Spectroscopy (EIS) and Linear Sweep Voltammetry (LSV) in three electrode cells with Ag/AgCl/3M KCl reference electrode and a cylindrical platinum mesh, serving as a counter-electrode. The EIS data acquisition was performed from 10^4 to 10^{-2} Hz, distributed in 50 frequency steps (at 120 mV), according to the Open Circuit Potential (OCP). After each EIS spectrum recording, individual LSV curves were recorded from +30 to -500 mV, (in cathodic direction), and from -30 to +600 mV (in anodic direction), respectively.

The recorded EIS spectra, were plotted both in Bode and Nyquist coordinates. In order to obtain quantitative data, the acquired EIS spectra were fitted to a suitable equivalent circuit, composed by two time-constants (parallel-RC units), with additional CPE. The formed anodic oxide layers demonstrate well-defined barrier properties even after 336 hours of exposure. The specimens did not show any remarkable indications for corrosion even after such a long time of exposure.

The method of recording individual LSV curves enables the determination of localized corrosion activity, by the occurrence of sharp inflexions in the anodic LSV branches. The data obtained are in good agreement with those from the EIS measurements.

Summarizing the data from both electrochemical methods, it can be concluded that the corrosion process of anodized AA1050 alloy in stationary hydrodynamic conditions is a self-inhibiting process, due to the insoluble corrosion products accumulation and the consequent pore obstruction. These processes suppress further corrosion, by hindering the access to the Al_2O_3 pores and defects.

Acknowledgments:
The authors are grateful for the financial support from the BNSF (contract No. КП06-Н37/16 / 2019)

Determination of the temperature dependence of the thermal conductivity coefficient of hvaf al-cu-fe quasicrystalline coatings

G. Frolov[1], M. Iefimov[1], V.Kysil[1], Yu. Yevdokimenko[1], Wang Changliang[2], Tian Haoliang[2], Li Zhang[2], Guo Mengqiu[2]

[1]Frantsevich Institute for Problems of Materials Science of the NAS of Ukraine, 3 Krzhizhanovsky st., UA-03142 Kyiv, Ukraine

[2]Aviation Key Laboratory of Science and Technology on advanced Corrosion and Protection for Aviation Material,AECC Beijing Institution of Aeronautical Materials, Beijing 100095, China

Abstract: The results of determining the thermal conductivity coefficient from quasicrystalline coatings of the Al-Cu-Fe system in the temperature range up to 900 °C are presented in the manuscript. A coating with a thickness of more than 0.8 mm was fabricated on substrate of steel 45 by high-speed air-fuel spraying. Determination of the temperature dependence of the thermal conductivity of the coating was carried out by solving the inverse problem of thermal conductivity by one-dimensional temperature fields in samples obtained by single-sided jet heating with an industrial hot air torch (at surface temperatures up to 450 °C) and an oxygen-propane welding torch (at temperatures above 450 °C). It is shown that the values of the thermal conductivity coefficient of Al-Cu-Fe quasicrystalline coatings in the range of 20 °C… 900 °C vary within $\lambda = 1.9 – 2.31$ W m^{-1} K^{-1}.

***KEYWORDS**: Al-Cu-Fe QUASICRYSTALLINE ALLOY, GAS-THERMAL COATINGS, THERMAL CONDUCTIVITY COEFFICIENT, INVERSE HEAT CONDUCTION PROBLEM*

1. Introduction

Quasicrystals (Q.C.) are solids with atomic stacking that is characterized by a perfect long-range order in the absence of translational symmetry and in presence of rotational symmetry with 5-, 8-, 10- or 12-fold axes forbidden in crystalline materials [1]. At present, Q.C. phases are found in more than 100 systems, most of them - alloys on aluminum base.

Unusual packing of atoms in some cases provides a unique combination of physical and chemical properties of these materials. Most of Q.C. were manufactured by rapid crystallization and appeared to be metastable, but there exist a number of stable Q.C. phases, for example in system Al-Cu-Fe.

The Al-Cu-Fe Q.C. acquired a great interest also for practical use for the combination of their properties (low density, high hardness, high elasticity modulus, high corrosion and wear resistance, low friction coefficient, reduced adhesion, low thermal conductivity combined with thermal expansion coefficient close by its value to one of metals [2, 3].

Q.C. has electronic properties most closely related to crystalline materials and thermal properties most closely associated with amorphous materials [4]. As distinct from metals, with the increase of temperature the electric receptivity of Q.C. drops: for Q.C. phase Al-Cu-Fe the values $\rho_{4K}/\rho_{300K} \sim 2 - 3$ are typical [5]. The thermal conductivity of the Q.C. phase Al-Cu-Fe at room temperature is on the level of the thermal conductivity of oxide ceramics ZrO_2. Thermal conductivity of Al-Cu-Fe Q.C. phase was studied at both low [6] and high temperatures [7]. As has been shown, the thermal conductivity of Q.C. phase increases with increasing temperature.

Thus, the features of electronic structure determine low electrical and thermal conductivity of Q.C. that in combined with high hardness allows their use as thermal barriers.

Thermophysical properties of the Q.C. phase of the Al-Cu-Fe system: density $\rho = 4.5$ g/cm^3; limiting temperature for the existence of the Q.C. phase $T_{max} \approx 880$ °C; values of the thermal conductivity coefficient in the range of 20 °C…800 °C $\lambda = 1.6 – 8.6$ W·m^{-1} K^{-1}; high hardness and low ductility (HV = 10 GPa and $\varepsilon <$ 2.5%, respectively, at 20 °C) maintained up to 500 °C; coefficient of thermal expansion in the range of 20 ° C…800 °C varies in the range from $\alpha = (14…41) \times 10^{-6}$, which causes intense cracking during cooling after casting or spraying [7].

In complicated Q.C. lattice the activation energy of dislocation movement is very high (of the order of some eV [8]), and the temperature dependence of the yield stress in them is very sharp. Therefore Q.C. at low temperatures (Al-Cu-Fe lower than 600 °C) do not reveal the macroplasticity. Due to above-mentioned properties Q.C. are very promising for the application as coatings.

Promising areas of application: heat-shielding coatings for internal combustion engines, non-stick coatings on equipment for chemical synthesis and the food industry, anti-icing coatings in aviation). The prospects of application of Q.C. coatings in such technical problems concerned with heat transfer in them are determined by the thermal conductivity coefficient of such coatings. In contrast to other thermophysical properties, the thermal conductivity of coatings are always many times or even an order of magnitude lower than that of monolithic material due to the presence of many internal boundaries (between individual applied particles and between sputtered layers).

In contrast to other thermal physical properties, the thermal conductivity of coatings is always in many times lower than in monolithic material due to the presence of many internal boundaries in coatings (between separate particles and between sprayed layers).

2. Materials, samples and coating technology

The water atomized $Al_{63}Cu_{25}Fe_{12}$ powder with a dispersion of +40/-63 μm and Q.C. phase content of about 75 wt. % was used for spraying. The coating was spraying to the end of a cylindrical substrate from steel 45 (diameter – 25 mm, height – 10 mm), which before spraying was subjected to jet-abrasive treatment by corundum powder with a determining particle size of 1 mm.

Spraying was performed by the high-velocity air-fuel (HVAF) spraying using the GVO-RV12 burner developed at the IPMS of the National Academy of Sciences of Ukraine.

The air-cooled burner with flow control of two-phase flow parameters has a gas-dynamic path with a total length of 310 mm (the supersonic part is 140 mm), the diameter of the supersonic nozzle is 12 mm and uses kerosene as fuel [9].

Spraying mode: the pressure in the combustion chamber of the burner is 1.0 MPa; the oxidant excess coefficient $\alpha \approx 1.2$, the spraying distance is 270 mm. The samples were placed on the side surface of a drum (120 mm diameter) rotating with a speed of 2.0 r/sec (the movement speed of the spray spot was 0.8 m/sec). Sputtering was performed in three runs of 10 seconds each with an interval of 30 seconds for cooling between each run.

For determination of temperature dependence of the thermal conductivity coefficient (λ) of the coatings, five samples were preparedю The average coating thickness was 820 μm, the average porosity was 4%.

The coatings have a tight adhesion to the substrate, a microstructure characteristic of HVAF coatings with a small number of defects in the form of differently oriented cracks up to 80 μm long. The Q.C. phase content in the coating measured by X-ray phase analysis is 75 wt. %. The adhesion strength of the coatings determined by the adhesive method is (18 ± 3) MPa.

3. The method of determining the temperature dependence of the thermal conductivity coefficient

The method of determining the temperature dependence of λ of gas-thermal coating materials is based on the use of a mathematical model of the heat transfer process in a flat plate during its one-sided heating, which is a homogeneous one-dimensional thermal conductivity equation. The model is implemented by «WarmingUp» computer program of solving the equation by means of finite elements method allowing one to determine time dependence of temperature of heated surface $T_{hot}(\tau)$ and specific heat flux from the rear ("cold") surface $q'_{out}(\tau)$, as well as the plate thickness and its thermophysical properties (density and temperature dependences of specific heat capacity and heat conductivity coefficient) determine the time dependence of its back surface temperature $T_{cold}(\tau)$.

In the solved Cauchy task, for the heat conduction equation the initial temperature of the sample T_0 is the initial condition, the temperature $T_{hot}(\tau)$ and the heat flux $q'_{out}(\tau)$ are the boundary conditions of the 1st and 2nd kind, respectively.

Any unknown parameter in the calculation can be determined by iterative calculation with the "WarmingUp" program with a known (experimentally or otherwise calculated) back surface temperature of the plate $T_{cold\,ex}(\tau)$, any unknown parameter. Before starting the calculations, this parameter is set to an arbitrary value, for example, a constant, then the temperature $T_{cold}(\tau)$ calculated from it is compared with the known temperature $T_{cold\,ex}(\tau)$ and a correction of the determined parameter is made to achieve their coincidence. The process of successive iterations with the values of the unknown parameter specified at each step continues until the temperatures $T_{cold}(\tau)$ and $T_{cold\,ex}(\tau)$ coincide with the specified accuracy throughout the heating time. The mean deviation of these temperatures at the level of 3 - 5 ℃ is quite sufficient, as it corresponds to the accuracy of the temperatures themselves determination.

The iterative process of determining any of the unknown parameters in the "WarmingUp" program is carried out automatically by a special control program, and takes no more than 10 minutes.

This determination of the desired temperature dependence λ of the plate material - the function λ(T) - is a variant of the widely used method of its determination by solving the inverse thermal conductivity problem (ITP).

In samples of coatings on substrates it is technically difficult to experimentally determine the temperature at the boundary between them. Therefore, the calculation is carried out in two stages: at the first stage the thermal conditions at the coating-substrate boundary are determined; at the second stage, the required temperature dependence $\lambda_{coat}(T)$ is found by the ITP solution method.

The task of the first calculation step is to determine the temperature of the "coating-substrate" boundary $T_{cold2}(\tau) = T_{hot1}(\tau)$ during heating (index 1 refers to the substrate, index 2 refers to the coating) end the specific heat flux through it $q'_{out2}(\tau)$.

The initial data for it are the experimentally determined specific heat flux from the back end of the substrate $q'_{out1}(\tau)$ (the boundary condition on it) and the temperature on it $T_{cold1\,ex}(\tau)$, with which the calculated temperature $T_{cold1}(\tau)$ is compared.

Thermal and physical properties of the substrate material (steel 45) – density, temperature dependences of specific heat capacity and thermal conductivity coefficient were taken from the electronic "Handbook of steels and alloys" [10].

Before the calculation, the desired temperature $T_{hot1}(\tau)$ is set by an arbitrary curve increasing from the initial value T_0. The temperature of the back surface of the substrate $T_{cold1}(\tau)$ is calculated from it, which is compared with the experimentally measured temperature $T_{cold1\,ex}(\tau)$. In a further iterative process, the dependence $T_{hot1}(\tau)$ is corrected until the compared temperatures coincide with a given accuracy. In the last iteration, the specific heat flux into the substrate $q'_{out2}(\tau)$ is determined.

The task of the second stage of calculation is to determine the temperature dependence $\lambda_{coat}(T)$, of the Q.C. coating material, which is a parameter corrected in the iteration process. The boundary condition on the heated surface of the coating is the experimentally determined temperature $T_{hot\,ex2}(\tau)$, on the back side of the coating - the specific heat flux from it $q'_{out2}(\tau)$.determined at the first stage.

In this study, the experimental temperature fields in the sample were obtained by unilateral heating with a jet of an industrial hair dryer (Bosch, Germany) with an air flow temperature of 660 °C and a nozzle diameter of 22 mm (at surface temperatures up to 450 °C) and the torch of a welding propane-oxygen burner (at higher temperatures). The need to use two heating sources is caused by the illumination of the pyrometers by the burner flame at temperatures below 450 °C, which makes it impossible to accurately determine the surface temperature at the initial stage of heating.

The structural diagram of the experimental model with a sample and the appearance of its heated surface are shown in Fig. 1a and b, respectively.

a

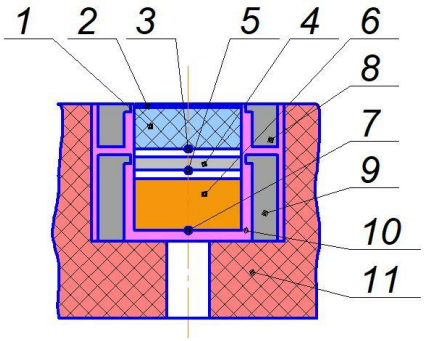

1 - sample substrate; 2 - coating on the sample; 3 - TEP of the sample; 4 - heat acceptor #1; 5 - TEP of heat acceptor #1; 6 - heat collector # 2; 7 - TEP of heat collector #2; 8 - sample holder; 9 - sensor holder; 10 - thermal insulation; 11 - fireclay body

b

***Fig. 1** - Experimental model: a - structural diagram; b - appearance of the heated surface (without surface blackening)*

Specific heat flow from the rear surface of the sample is measured by a two-layer heat flow sensor, consisting of two heat receivers installed in series with an air gap between them. The diameter of heat receivers is 25 mm, heat-receiver #1 is made of steel 12Kh18N9T (height is 3 mm), heat-receiver #2 - of M1copper (height is 12 mm). In the center of back surface of each sensor couples thermoelectric transducer (TET) - type K thermocouple (wire diameter 0.2 mm). The same TET was installed in the center of the back face of the sample substrate.

The one-dimensional model used in the calculation, assumes uniform heating of the sample surface and no heat transfer through its lateral surfaces. To limit of heat transfer in the radial direction, the sample and the heat flux sensor were placed in stainless steel shells, insulated with asbestos thread, and the entire experimental model was placed in a high-porosity chamotte case.

The experimental model with the sample was installed coaxially under the hair dryer or burner at a distance that provided the required level of surface temperature stabilization, 35 mm and 180 mm, respectively.

During the experiments, the temperature in the center of the heated face of the sample was measured by two pyrometers

mounted at a distance of 1.4 m from the surface at an angle of 20º to the normal and having the following technical specifications:

pyrometer # 1 - INFRATHERM Converter IGA 100 (IMPAC Electronic Gmb, Germany): measuring temperature range 350...1800 °C. Wavelength λ= 1.45...1.8 μm. Possible radiation coefficient ε = 0.2...1.0. Error of measurements at temperatures up to 1500 °C does not exceed 0.3 %;

pyrometer # 2 - recorder pyrometer USB FLUS IR-863U (PRC): working range: 50 ~ 1650 ° C; D: S (ratio of distance to the object to the beam width) - 50:1; maximum measurement frequency - 4 Hz; the accuracy of measurements in the range to 500 ° C – 1.0% ± 1 °C, in the range of 500 ~1650 ° C – 1.5% ±2 ° C.

The heated surface of the coating samples was blackened with soot and its radiation coefficient was taken to be ε = 0.93.

Before the start of the experiment, the heated surface of the experimental model was reliably thermally insulated with a thermal screen; after the heating source entered the operating mode, the screen was quickly removed, fixing the time the sample began to heat up.

Recording the data of pyrometers and TET was performed on a personal computer with a measurement frequency of 1 Hz, in the second case - by a special data processing program through the analog converter AKON-T.

From the records of the pyrometer data, the function of the dependence of the surface temperature on time $T_{\text{hot ex2}}(\tau)$ was obtained, which was smoothed by polynomial approximation to the 9th degree using the software package for numerical data analysis and scientific graphics "Origin".

Sensor temperature curves were also approximated by polynomials to smooth their derivatives, determining the values and dynamics of heat fluxes in them and, accordingly, the heat flux from the sample. Based on the smoothed temperature curves of sensors $T_{\text{dat1}}(\tau)$ and $T_{\text{dat2}}(\tau)$, the specific heat fluxes in them were calculated:

$$q'_{\text{dat } i} = T'_{\text{dat } i}(\tau)\, m_i\, C_{pi}(T) / S_i,$$

where index i is the number of the heat sink; m_i, $C_{pi}(T)$, S_i are the mass, specific heat capacity, and area of the heated surface of the sensor, respectively;

The total heat flux from the back side of the substrate:

$$q'_{\text{out1ex}} = q'_{\text{dat 1}} + q'_{\text{dat 2}}$$

The temperature dependence of specific heat capacity $C_{\text{p cc}}(T)$ of Al-Cu-Fe Q.C. alloy required for calculation of λ in the temperature range of 20 - 500 °C was determined by the device IT-s-400 [x+3], the obtained function was approximated by a polynomial of the 2nd order and extrapolated to 850 °C. This dependence is shown in Table 1.

Table 1 *– The temperature dependence of the specific heat capacity of a Q.C. alloy used in the calculation*

Temperature, °C	20	100	300	500	700	850
Specific heat capacity, kJ kg^{-1} K^{-1}	676	702	762	811	851	874

Taking into account the porosity of the coating of 4%, its density was assumed to be ρ_{cc} = 4.28 g/cm^3.

Two cycles of jet heating were performed on each sample: in the first one, the coating surface was heated to 400 °C by a 650 °C air jet from an industrial hair dryer, and in the second one to 850 °C by the torch of the welding oxygen-propane burner. From the temperature field recorded in the first cycle, the λ of the coating from room temperature to 400 °C was determined according to the described methodology. In the second cycle, because the pyrometers were illuminated by the welding torch flare, they began to show the temperature of the heated coating surface from about 450 °C, so in the range up to 400 °C, this temperature was determined using the already known values of the heat transfer coefficient, the coating-substrate border temperature and the heat flow through this border. In subsequent iterations, the λ values were varied so as to ensure the smoothest possible fit between the calculated temperature and the temperature recorded in the experiment ($T_{\text{hot ex2}}(\tau)$ > 500 °C). The values of $\lambda_{\text{coat}}(T)$ at temperatures above 500 °C were then determined using the technique described above.

4. Results of experimental determination of the temperature dependence of $\lambda_{coat}(T)$ of Al-Cu-Fe Q.C. coating

On three samples of coatings (samples # 1, # 2, # 3) were carried out on two measurements (heating cycles) - at low-temperature heating with a hair dryer and at high-temperature heating with an oxygen-propane burner.

Fig. 2 shows the temperature fields prepared for the calculation, obtained on the sample #1 at low-temperature (a) and high-temperature (b) heating.

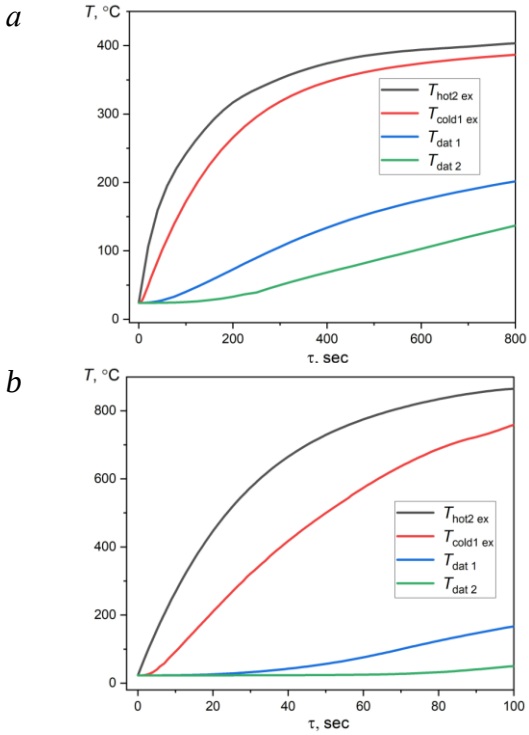

Fig. 2 *- Temperature fields in the experimental model (sample #. 1): a - heating with a hair dryer; b - heating with a burner*

The graphs show the time dependences of the heated surface temperature $T_{\text{hot ex2}}(\tau)$, the back surface of the substrate $T_{\text{cold ex1}}(\tau)$, and the heat flow sensor temperatures $T_{\text{dat 1}}(\tau)$ and $T_{\text{dat 1}}(\tau)$. The calculated values of specific heat fluxes from the sample are shown in Fig. 3.

The temperature dependences of the coating thermal conductivity coefficient $\lambda_{\text{coat } mn}(T)$, where m is the sample number and n is the sample heating cycle number, determined for all the six obtained temperature fields (two for each sample) are shown in Fig. 4. The dependence $\lambda_{\text{coat}}(T)$, averaged over all of them, which is taken as the required temperature dependence of λ of HVAF coating from Q.C. alloy Al-Cu-Fe is also shown there. The values of this dependence are given in Table 2.

As can be seen from Fig. 4, the coatings show a monotonic growth of λ and have close values - deviations of λ values obtained on samples # 1 - 3, from the average values do not exceed 10%, 8% and 2%, respectively, and are approximately the same over the entire temperature range. At temperatures above 700 °C the dependences have a different appearance: the λ values of the coating of sample # 3 begin to decrease; the coating of samples # 1 and # 2 grow with different intensity. Taking into account the partial delamination of coating # 3 from the substrate in the process of further cooling, we can assume that the decrease in its λ is caused by the weakening of the contact between the coating and the substrate as a

result of cracking under the effect of thermomechanical stresses due to the difference in their thermal expansion coefficients. The difference in λ values obtained on different samples is probably caused by the different number of defects in the coating and at the "coating-substrate" boundary: the more there are, the lower the determined value of λ. Thus, the values of the thermal conductivity coefficient of the coating itself are most characterized by the maximum values obtained on individual samples.

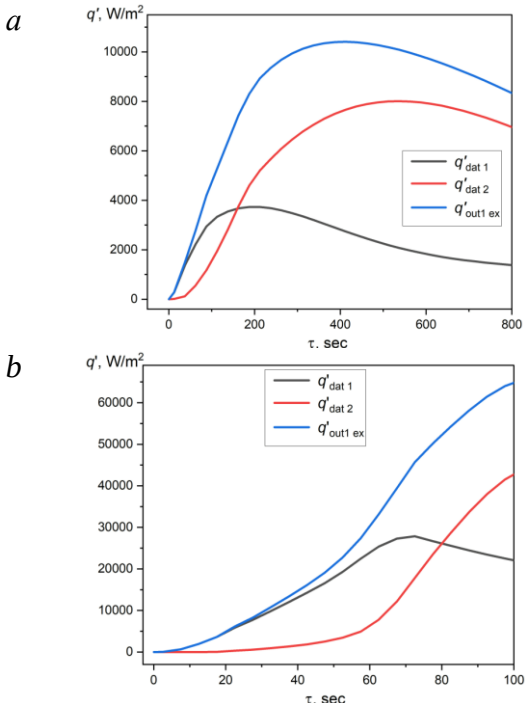

Fig. 3 *- Heat fluxes of sensors # 1 and # 2 (q'_{dat1} and q'_{dat2}, respectively) and the heat flux from the back of the substrate $q'_{out1\ ex}$: a - heating by hair dryer; b - heating by burner*

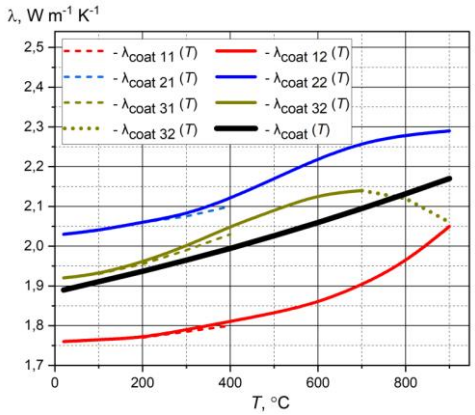

Fig. 4 *- Temperature dependences of the coefficient of thermal conductivity of coating samples # 1 - 3 under different types of heating and their averaging dependence $\lambda_{coat}(T)$*

Table 2 *- Temperature dependence of thermal conductivity coefficient of HVAF-coating from Al-Cu-Fe Q.C. alloy*

Temperature, ℃		20	100	300	500	700	850
Thermal conductivity coefficient, λ W m^{-1} K^{-1}	Average	1.89	1.91	1.96	2.03	2.09	2.15
	Max	2.03	2.04	2.08	2.17	2.26	2.29

5. Conclusions

1. A method for determining the temperature dependence of the thermal conductivity coefficient of gas-thermal coatings based on solving the inverse problem of thermal conductivity under one-sided heating has been developed.

2. Using this method we determine the temperature dependence of the coefficient of heat conductivity of HVAF $Al_{63}Cu_{25}Fe_{12}$ coating with a quasicrystalline ψ phase (75± 2) wt. %. In the temperature range 20...850 ℃, the average λ values of Q.C. coating determined for three samples increase monotonically from λ_{coat} = 1,9 9 W m^{-1} K^{-1} to λ_{coat} = 2.15 W m^{-1} K^{-1}.

3. The values of the thermal conductivity coefficient obtained for different samples differ significantly from each other (up to 25 %), which can be explained by the heterogeneity of the coating structure and the different quality of contact between the coating and the substrate.

6. References

1. Dubois J.-M. Introduction to Quasicrystals. – Berlin: Springer Verlag, 1998. – 392 p.

2. Sordelet D.J., Kramer M.J., Unal O. Effect of starting powders on the control of microstructural development of Al-Cu-Fe quasicrystalline plasma-sprayed coatings // J. Thermal Spray Techn. – 1995. – **4**, No. 3. – P. 235-244.

3. Dubois J.-M., Proner A., Bucaille B. et al. Quasicrystalline coatings with reduced adhesion for cookware // Ann. Chim. Fr. – 1994. – 19. – P. 3-25.

4. Pope, A.L., Tritt, T.M. (2004). Thermal Conductivity of Quasicrystalline Materials. In: Tritt, T.M. (eds) Thermal Conductivity. Physics of Solids and Liquids. Springer, Boston, MA. https://doi.org/10.1007/0-387-26017-X_11

5. Berger C., Mayou D., Cyrot-Lackmann F. "Anti" metallic properties of quasicrystals // C. Janot, R. Mosseri (Eds.), Proc. of the 5th Internat. Conf. on Quasicrystals, Singapore: World Scientific. – 1996. – P. 423-430.

6. A. Biluši´c, A. Smontara, J.C. Lasjaunias, J. Ivkov, Y. Calvayrac. Thermal and thermoelectric properties of icosahedral $Al_{62}Cu_{25,5}Fe_{12,5}$ quasicrystal. Materials Science and Engineering 294–296 (2000) 711–714.

7. Dubois J.-M. Useful Quasicrystals. World Scientific, – 2005. – 482 p.

8. Feuerbacher M., Metzmacher C., Wollgarten M. et al. The plasticity of icosahedral quasicrystals // Mater. Sci and Eng. – 1997. – A233, P. 103-110.

9. Evdokimenko Yu. Burner for High-Velocity Air-Fuel Spraying of ZrB_2 Based Coatings for Aerospace Technics / Evdokimenko Yu., Kysel V.,G. Frolov , G. et al. // "Space Research In Ukraine 2014-2016" Report to COSPAR. Scientific Editor O. Fedorov. – Kyiv. – Akadempereodyka. – 2016. – P.114-117.

10. Steel and alloys. Electronic reference book /. www.splav-kharkov.com/